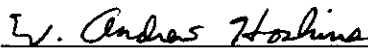# ASYMMETRIC DISCHARGE PATTERNS IN THE MPD THRUSTER

by

W. Andrew Hoskins

Princeton University
School of Engineering and Applied Science
Department of Mechanical and Aerospace Engineering

Submitted in partial fulfillment of the requirements for the degree
of Master of Science in Engineering from Princeton University, 1990.

Prepared by:

W. Andrew Hoskins
W. Andrew Hoskins

Approved by:

R. G. Jahn
Professor Robert Jahn
Thesis Advisor

A. J. Kelly
Arnold Kelly, Sr. Research Engineer
Thesis Reader

January, 1990

ABSTRACT

Azimuthally asymmetric behavior that is observed during operation of a quasi-steady Magnetoplasmadynamic (MPD) thruster operated at low $J^2/\dot{m}$ with argon has been investigated. Asymmetric behavior can produce such adverse effects as off-axis thrust and uneven anode heat loading during operation. In addition, asymmetric behavior can limit the utility of diagnostic measurements that require an assumption of axisymmetry.

In addition to high speed photographic sequences which yield time-resolved information on the luminosity patterns, a set of four symmetrically placed magnetic field probes enable an evaluation of the three dimensional nature of the developing current conduction pattern. A centroid of current parameter is defined to elucidate the temporal behavior of the conduction pattern as measured by the four probe rig. Excellent correlation between the luminosity patterns and the centroid of current is demonstrated.

Both photographic sequences and probe data reveal asymmetric behavior at all conditions, except the highest $J^2/\dot{m}$ (30 kA, 6 g/s), as a non-recurring transient that is always associated with the initiation of the discharge pulse. Although most of the asymmetric behavior subsides after the transient, some localized and unsteady non-uniformities do persist for the duration of the discharge at values of $J^2/\dot{m}$ below about 10 kA^{2}s/g. Throughout the transient, the angular position of the maximum luminosity and magnetic field remains stationary while the discharge spreads uniformly around the thruster until a symmetric pattern is achieved. There is no evidence of a rotating or oscillating spoke. The "asymmetry parameter," defined as the instantaneous distance of the current centroid from the center of the thruster, and the transient time are both shown to scale with $J^2/\dot{m}$. Typical transient times reach as high as 700 μs at 4 kA current and 15.5 g/s mass. Conditions that yield 1000 s specific impulse (e. g. 16 kA at 6 g/s) have typical times of 250 μs.

Two possible mechanisms for the establishment of a symmetric discharge are discussed. The first involves the diffusion of plasma, driven by azimuthal pressure gradients, from regions of high

conductivity into regions of lower conductivity. Calculations of diffusion velocities based on gradients inferred from filtered photography demonstrate that diffusion can occur on a time scale consistent with the observed transient times. In the second mechanism, back emf generated by the movement of the flow through the magnetic field promotes decreased Ohmic power deposition in regions with higher conductivity and flow velocity. Since the relative importance of back emf scales with the magnetic Reynolds number, the scaling of the asymmetric behavior with $J^2/\dot{m}$ is correlated with the scaling of the magnetic Reynolds number with the same parameter.

TABLE OF CONTENTS

LIST OF FIGURES

Chapter 1

INTRODUCTION

Future long duration or long range spacecraft missions will require a higher specific impulse than is possible with chemical propulsion systems. Since the power used to develop thrust in a chemical rocket comes from the propellant itself, the energy per unit propellant mass available from a reaction effectively limits the specific impulse to a few hundred seconds for any chemical rocket. Electric propulsion overcomes this limitation by using a power supply external to the flow, providing values of specific impulse ranging from several hundred to several thousand seconds.[1]

Electric propulsion can be divided into three classifications: electrostatic, electrothermal, and electromagnetic. In an electrostatic thruster, ions are accelerated through an applied electric field, achieving very high levels of specific impulse, but at very low thrust densities. Electrothermal thrusters heat the flow with a resistor or columnated arc and recover useful thrust by expanding the flow through a nozzle. Electromagnetic thrusters pass large currents through the propellant in a diffuse arc, creating high magnetic fields, which in turn accelerate the current carrying plasma via the Lorentz force.[1] In actuality, arc thrusters fall along a spectrum of devices combining electrothermal and electromagnetic acceleration mechanisms. At one extreme lies the low power arcjet, whose acceleration mechanism is primarily electrothermal, providing relatively low values of specific impulse. Operated at 1 - 30 kW input power, the arcjet has good prospects for deployment in the near future. At the other end of the spectrum is the magnetoplasmadynamic (MPD) thruster, whose acceleration mechanism is primarily electromagnetic. The MPD thruster is attractive because of its high thrust density, simplicity of design, and specific impulse values of 1000-5000 s, which are optimal for many orbit transfer and interplanetary missions.

In the typically axisymmetric design of electric thrusters, the thrust should be oriented in the axial direction for efficient propulsion. This thrust orientation in turn requires axisymmetric patterns of electrical current flow in the discharge. Therefore, it is imperative to know under which

1

conditions the MPD thruster discharge is cylindrically symmetric. Since deployment of multimegawatt MPD systems must await the development of power supply modules over 100 kW, there has been considerable interest in operating MPD thrusters at lower powers, at least until such time as large power supplies become available.[2,3] The focus of this thesis is the study of azimuthally asymmetric discharge patterns that may develop at these low powers in the MPD thruster.

1.1 The MPD Accelerator

A basic co-axial MPD thruster is diagrammed in Figure 1-1. Gaseous propellant is injected through openings in the insulating backplate into the space between the anode and cathode. When a voltage of several hundred to several thousand volts is applied between the central, cylindrical cathode and the annular anode, electrical breakdown occurs. The propellant is ionized and begins conducting currents of several thousand amperes in a diffuse plasma arc. If the current distribution is cylindrically symmetric, the high currents produce large magnetic fields in the thruster that are oriented entirely in the azimuthal direction. By interacting with the current flow through the plasma, this magnetic field exerts a Lorentz force on the plasma in a direction perpendicular to the local magnetic field and current vectors. Radial current components produce axial thrust, and axial current components directed upstream "pump" the plasma toward the cathode where it exerts pressure on the cathode tip for an added increment of thrust.

An MPD thruster is usually operated in either a continuous or a "quasi-steady" mode. In the latter, a pulse-forming network supplies current to the thruster in a square wave pulse on the order of 1 ms long, which allows acceleration processes to attain a steady state condition.[4] The main advantages of operating in the quasi-steady mode for ground-based testing are that this mode allows probing in the discharge and circumvents limitations in the power supply, vacuum pumping speed, and facility cooling.
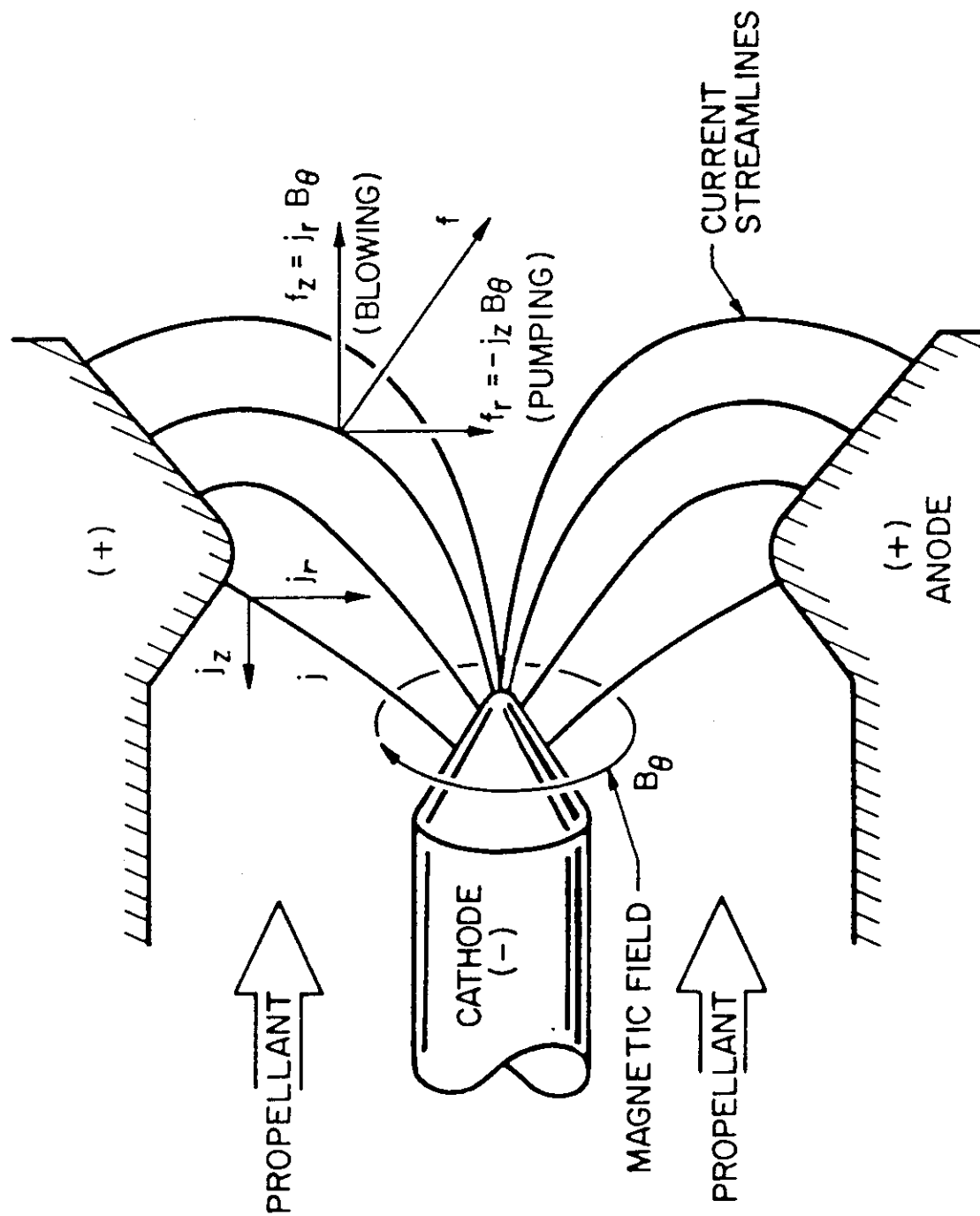
SELF - FIELD MPD ACCELERATOR

FIGURE I-I

1.2 Azimuthally Asymmetric Discharge Patterns

During a photographic investigation of plasma symmetry for spectroscopic purposes, unusual behavior of a low-power, argon MPD discharge was noted. The top of Figure 1-2 shows an end view, time-integrated photograph of a pulsed MPD discharge with a total thruster current of about 4 kA, a mass flow of 5.9 g/s, and a pulse length of 1 ms. A 488 nm line pass filter was used to visualize radiation from an excited state of singly ionized argon, the most abundant ionic species in the discharge. The luminosity pattern is grossly asymmetric, bulging out greatly in one direction. While the behavior is qualitatively repeatable for given operating conditions, the angular position of maximum radial extent is not consistent from shot to shot, indicating that the phenomenon is not merely a result of misalignment or an optical effect. As the thruster current is increased, this striking non-uniformity diminishes gradually until a completely symmetric discharge is observed at about 16 kA (Fig. 1-2, bottom).

Such asymmetric discharges have been noted by other researchers working with pulsed thrusters when the current is decreased sufficiently. Gilland[5] observed lopsided patterns on time-integrated photographs of the discharge in a half scale version of the thruster operating in Figure 1-2. The asymmetric discharges appeared below about 10 kA at 3 g/s argon and 7 kA at 1.5 g/s, with the asymmetric behavior worse at lower currents. Using a thruster with the same electrode configuration and scale as Gilland, but in a different vacuum facility, Polk[6,7] observed lopsided discharges at similar conditions. In addition to noting the increasing severity of the asymmetry at lower currents, Polk also noted a slight increase in severity at higher mass flow rates. The values of current squared over mass flow ($J^2/\dot{m}$) for which photographs of the discharge in the half scale thruster appears asymmetric are similar to the values for the full scale thruster. Thus, $J^2/\dot{m}$, which is proportional to the specific impulse, is an important scaling parameter.

While investigating the range of useful operating conditions for helium in the same full scale device, Simpson[8] described asymmetric behavior appearing at currents below 20 kA at 2 g/s. He hypothesized that the phenomena may be more dependent upon applied breakdown voltage than

4
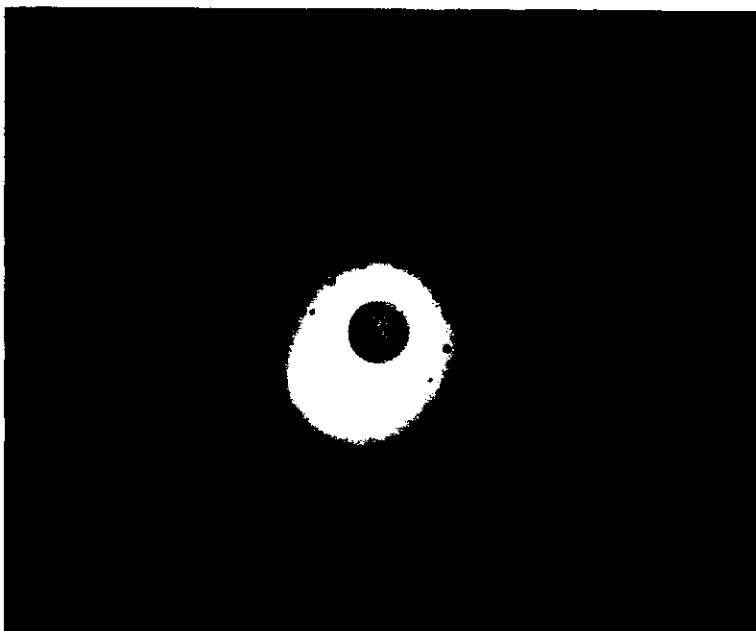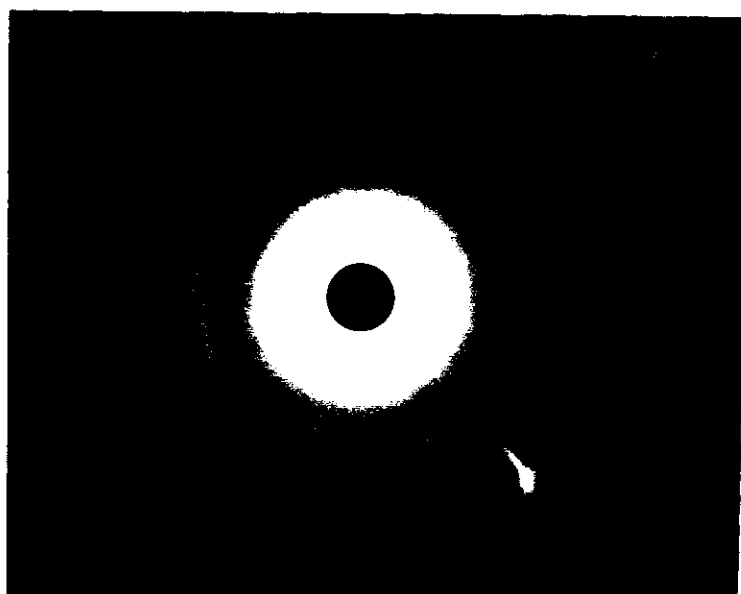
4 kA, 5.9 g/s

16 kA, 5.9 g/s
End View, 488 nm Light
Figure 1-2

current since, by varying the capacitor bank configuration to vary the current at a given charging voltage, he saw similarly asymmetric patterns. However, this assessment is not conclusive because he judged the asymmetric nature of the discharges from time-integrated photographs. Since changing the bank configuration also changes the pulse length, the effect of a different pulse length on the degree of asymmetry apparent in an integrated photograph is unclear.

Working with a radically different geometry (Figure 1-3), Heimerdinger[9] established minimum current conditions below which asymmetric discharges would result. Below 40 kA at 4 g/s argon, he was plagued with asymmetric discharges that remained stationary throughout the 400 μs pulses. He also noted that the asymmetry disappears at currents near the threshold after several shots, indicating that the phenomena is linked to electrode condition. Heimerdinger attributed the relatively high currents needed to achieve axisymmetry to his large cathode radius (5.5 cm) which lowered the current density at the cathode surface. However, the average current density at his threshold condition (150 A/cm^2) is about 60 % of that for the condition for which symmetric discharges are achieved in the thruster studied in this thesis, and 30 % of the density seen in the half scale model. This hypothesis also does not account for any dependence on mass flow rate.

Using still another very different geometry (Figure 1-4) with hydrogen and ammonia propellant, Nishida et al.[10] have seen a highly non-uniform distribution of anode spots around the anode. By dividing the anode on their K-XI model thruster into 16 azimuthal segments, each with its own pulse-forming network, they were able to force the discharge to distribute more uniformly and improve efficiency and thrust. The improvements were greatest at lower currents, indicating again stronger asymmetry at lower currents.

Clearly, there is much evidence for the pervasive existence of an asymmetric discharge phenomena during low current operation of MPD thrusters.

1.3 Impetus for Studying Asymmetric Discharge Patterns

Azimuthally asymmetric discharge patterns have several adverse ramifications for thruster
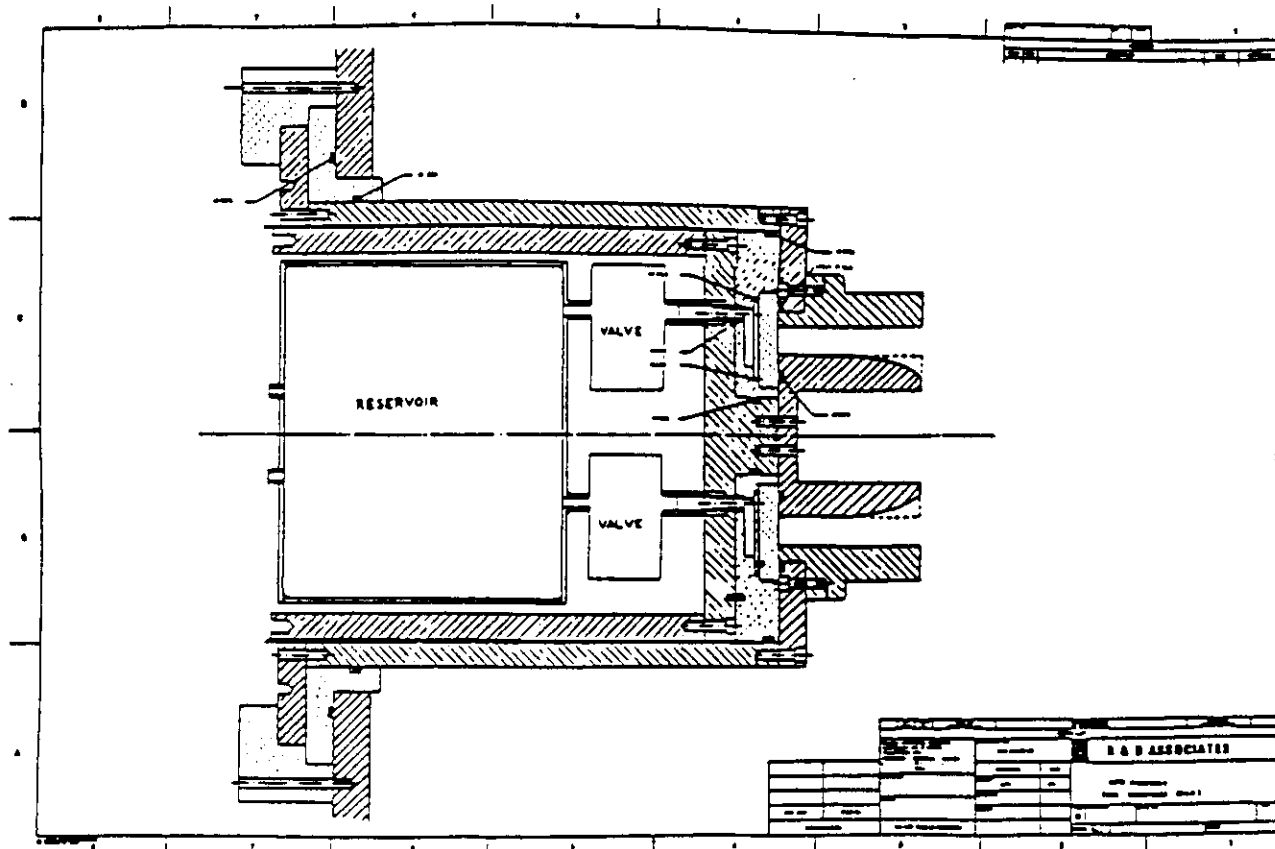
Geometry of Heimerdinger's Thruster

Figure 1-3

K-VI/DA/ESC

CATHODE
ANODE

K-XI

0 1 2 3 4 5 cm
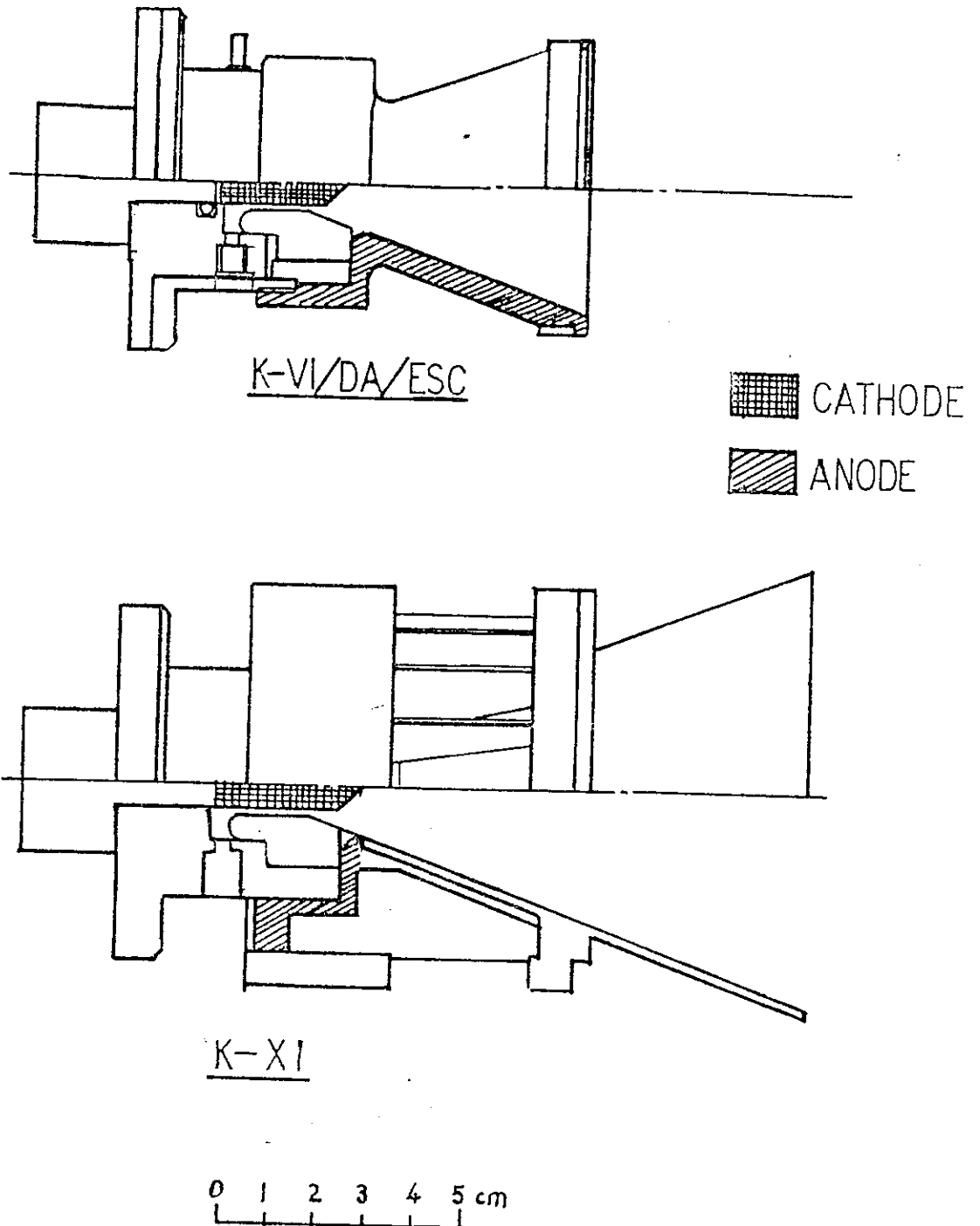
Geometry of Nishida's Thruster

Figure 1-4

operation. Asymmetric magnetic field and current patterns can result in off-axis thrust, which would produce unwanted torque on the spacecraft if consistently directed or attenuate the directed thrust if randomly directed. Non-uniform current distributions at the anode could locally deposit more power in the anode than can be accomodated by the design. Moreover, non-uniform cathode current densities would produce uneven erosion, possibly leading to premature failure. Since a significant portion of the thrust in a partially ionized flow is produced by momentum coupling between charged and neutral species,[11] a non-uniform distribution of charged species will tend to reduce the total thrust. If most of the charged species were concentrated on one side of the thruster, propellant outside the ionized region would be unaccelerated by the discharge. Recurring or time-dependent asymmetric behavior may drive low frequency noise, which could interfere with spacecraft communications or data collection. Finally, since most diagnostic techniques and theoretical analyses assume axisymmetry, including probing, spectroscopic analysis involving an Abel inversion, and surface layer activation for cathode erosion measurements, asymmetric behavior could compromise results from such measurements.

Although much research has been directed toward operating MPD thrusters at the highest currents possible to achieve better thrust, specific impulse and efficiency, there are several reasons to characterize the limits for low current operation. The primary reason, as stated previously, is that space-based power supplies available in the near future are limited to 100 kW or less. The asymmetric discharge at the top of Figure 1-2 required approximately 100 kW instantaneous power. By comparison, 1.5 MW was required to produce the symmetric discharge at the bottom of Figure 1-2. Since voltage is a monotonically increasing function of current and a slightly decreasing function of mass flow[12], operation at lower powers will necessitate lower currents or higher mass flows for a given thruster design.

A second reason for interest in operation at lower currents is that the ratio of thrust to power increases as current decreases. A semi-empirical model by Choueiri[11] of performance characteristics of the thruster studied in this thesis shows thrust to vary linearly with current for the

conditions for which asymmetric behavior is noted:

$$T = \dot{m}u_{ac}J/J_{fi}.$$

u_{ac} and J_{fi} are the Alvén critical velocity and full ionization current, respectively, and are constant for a given mass flow and propellant. The thrust to power ratio is then

$$T/P = \dot{m}u_{ac}/J_{fi}V(J).$$

Since voltage decreases with decreasing current, thrust to power increases with decreasing current. In a power limited situation, higher thrust to power ratios mean higher thrust, which allows shorter trip times. From the efficiency equation:

$$\eta = 1/2\, \dot{m}u_e^2/P = 1/2\, u_e\,(T/P) = 1/2\, gI_{sp}(T/P),$$

it is clear that for a given efficiency, there is a trade off between specific impulse and the thrust to power ratio. However, for orbit transfer missions in which short transfer times are required, it may be beneficial to sacrifice some of the specific impulse achieved at higher currents for a better thrust to power ratio. Some near earth missions presently under consideration have specific impulse requirements of about 1000s.[10] This level of specific impulse is produced at the threshold conditions below which asymmetric behavior becomes noticable in photographs.

Other reasons for interest in operating MPD thrusters at low currents include the possibility of ganging several smaller thrusters together for flexibility in throttling and maneuvering and to reduce the high cost of ground-based testing.[3] In addition, in the event that high currents are used at steady state, the thruster will be started up at low currents. Persistent asymmetric behavior during this start-up period could produce the same adverse effects listed previously. Finally, recent data on cathode erosion rates indicate that there are threshold currents and pulse lengths above which bulk melting of the cathode surface occurs, resulting in very high erosion rates. Polk measured this threshold to be about 10 kA for a 2 ms pulse in a half scale thruster.[13] Such high erosion rates may necessitate using lower currents.

Many experimenters are presently operating in the range of current and mass flow for which asymmetric discharges have been observed.[14,15] For example, in order to examine the effect of

thruster current on cathode erosion, it is necessary to examine as broad a range of currents as possible. Due to upper limits on the current imposed by the facility, Polk[6] must obtain measurements at current levels as low as 8 kA, well within the regime in which asymmetric discharges are observed. Choueiri's plasma wave experiment[11] is limited to relatively low currents in order to obtain an acceptable signal to noise ratio. For all these reasons, it is important to know the conditions for which asymmetric behavior appears in MPD thrusters.

Although azimuthally asymmetric discharges have been observed at low currents by several experimenters, no one has undertaken a time-resolved study specifically of this phenomenon. To determine the potential impact of asymmetric behavior on both steady and quasi-steady operation, it is essential to characterize it. It was the purpose of this study to determine whether or not the asymmetric patterns are time dependent or steady in nature, and if time dependent, to measure the time scales over which the phenomenon persists. In addition, the dependence of the occurrence and degree of asymmetry upon current, mass flow, capacitor bank charging voltage were investigated. Also, the correlation between asymmetric luminosity patterns and possibly asymmetric current patterns were studied to determine whether one occurs without the other. Since current pattern data are more easily quantifiable than luminosity patterns, study of the current patterns enables quantification of the asymmetric behavior. Finally, characterization of this phenomenon has yielded physical insight into the mechanisms behind it as well as the thruster operation in general.

To facilitate these goals, time-resolved photographic sequences from a high speed movie camera have been used to record the development of the luminosity pattern throughout the pulse. A set of four symmetrically placed magnetic field probes has enabled a three dimensional study of the current distribution in time. Chapter 2 will provide details of the experimental facility and diagnostics. Chapter 3 will describe the results of luminosity studies using time-integrated photographs and time-resolved photographic sequences. Chapter 4 will discuss the results of experiments using the magnetic field probes and examine the dependence of asymmetric behavior on operating conditions. The Chapter 5 provides a discussion of the possible mechanisms for the

11

observed asymmetric behavior. The final chapter gives a summary of the results and their implications for thruster operation.

Chapter 2

EXPERIMENTAL FACILITIES AND DIAGNOSTICS

2.1 Experimental Facilities

The Electric Propulsion Laboratory has been a center of plasma propulsion research for over twenty-five years. Much of the experimental facility used in this study has been developed over this period and is described briefly here. More detailed descriptions can be found in reports and theses published by this laboratory.[4,12,16,17]

2.1.1 The MPD Thruster and Vacuum Facility

The thruster used in this study is an open-throated, coaxial device, usually designated the "Full Scale Benchmark Thruster" (FSBT). A cross-section of the thruster and a schematic of the related facilities is shown in Figure 2-1. The thruster has a cylindrical chamber 5 cm deep and 6.35 cm in internal radius with a Pyrex wall and a boron nitride backplate. The cathode is a 1 cm radius rod of 2% thoriated tungsten with a hemispherical tip. The annular aluminum anode is 1 cm thick, with a 5.1 cm radius orifice and a 9.3 cm outer radius. The anode is mounted on an aluminum cylinder that can have a view port extension, enabling direct side observation of the entire chamber through the Pyrex chamber wall. Figure 2-2 is an exploded view photograph of the thruster, showing the anode column parts with view port extension in the top row, and the cathode and mass injection assembly below. Figure 2-3 shows two views of the assembled thruster.

Mass injection into the chamber through the backplate is split equally between an annulus at the base of the cathode and 12 equally spaced holes at a radius of 3.75 cm from the thruster axis. At a radius of 2 cm, there is also a second set of holes from a previous experiment that are unused. These holes are blocked by the Plexiglas distribution plate that lies underneath the backplate. The mass flow rate is controlled by two sets of six choked orifices located beneath the distribution plate. One set feeds the annulus and the other feeds a plenum that distributes the flow to the 12 outer
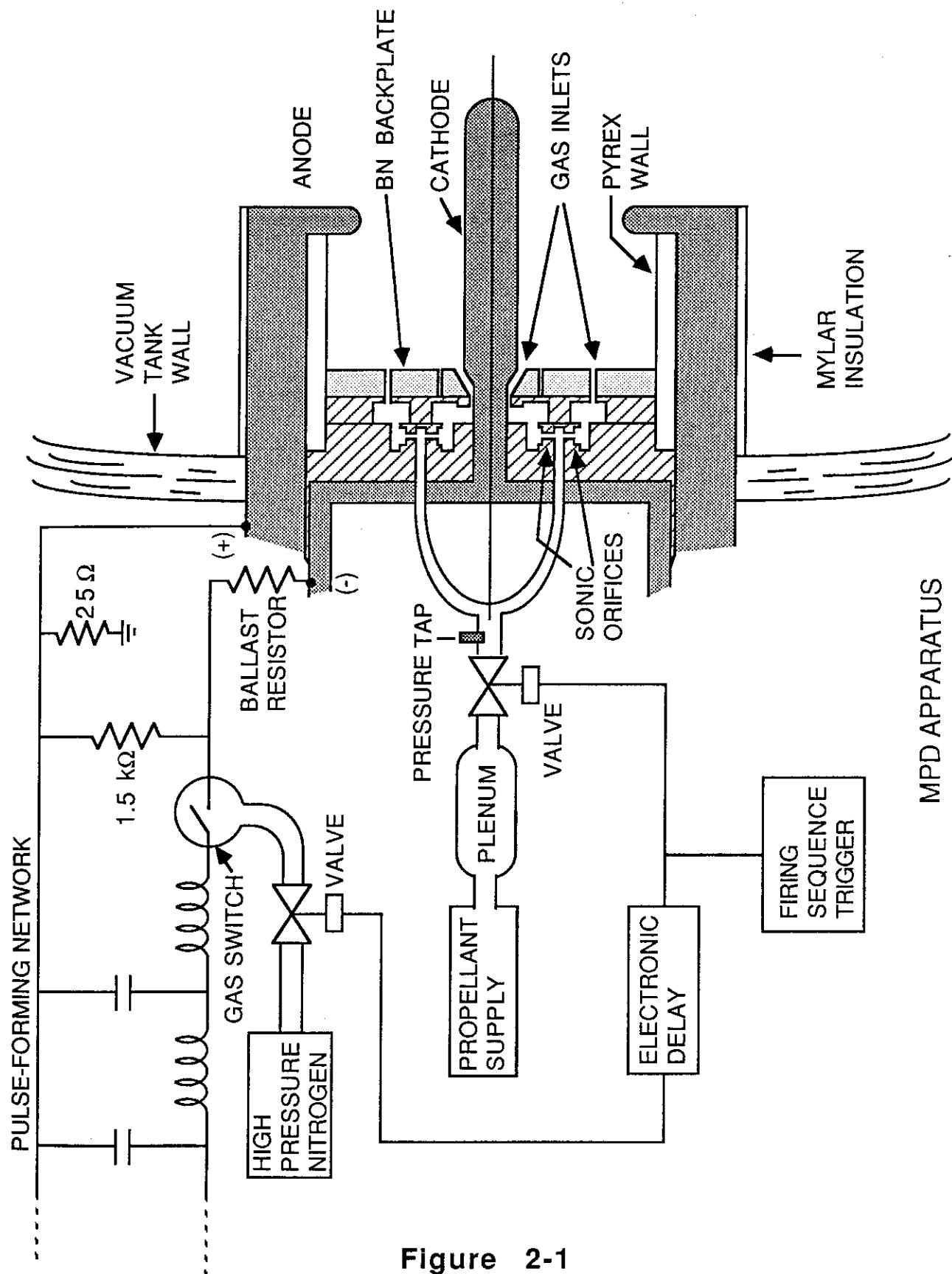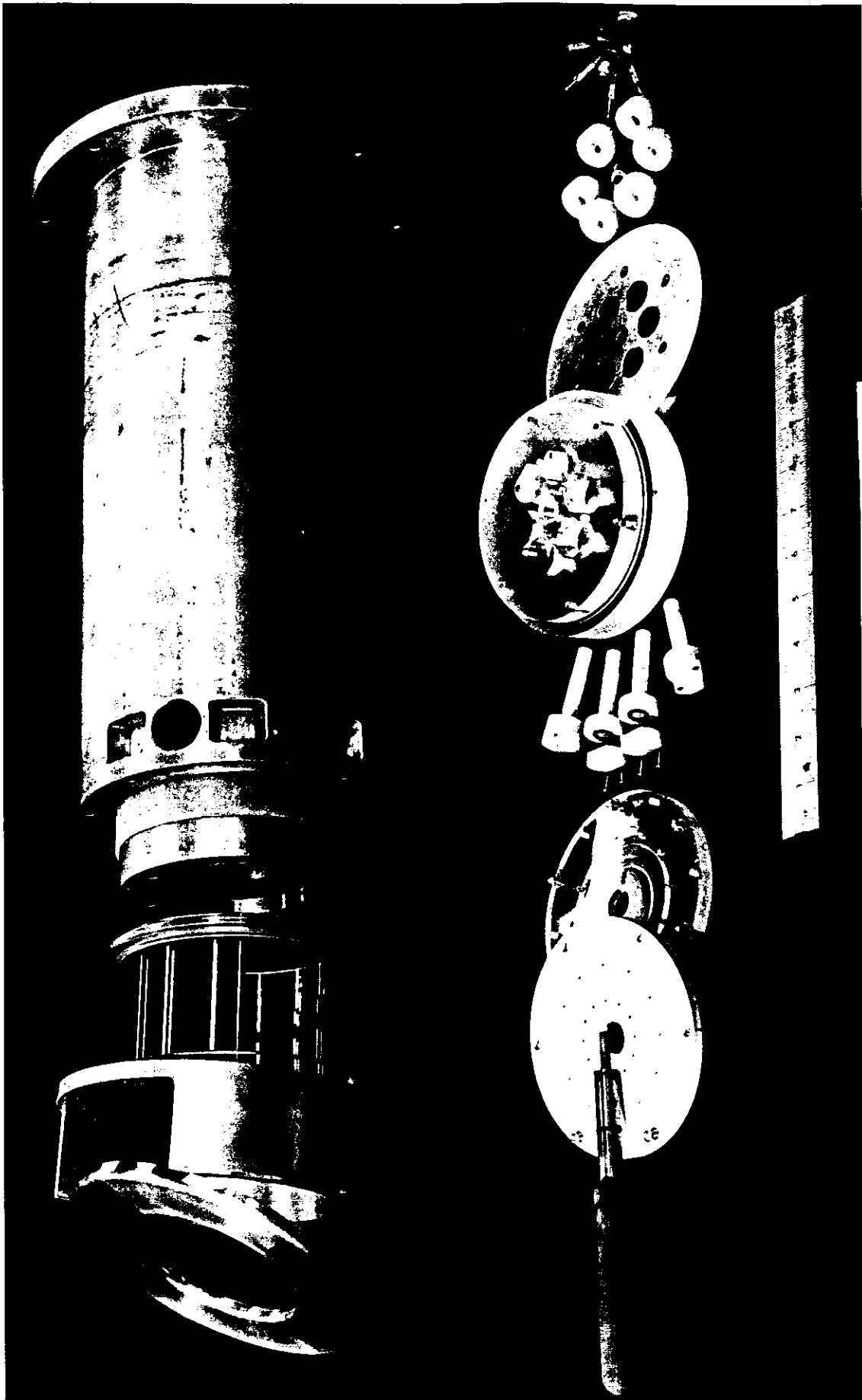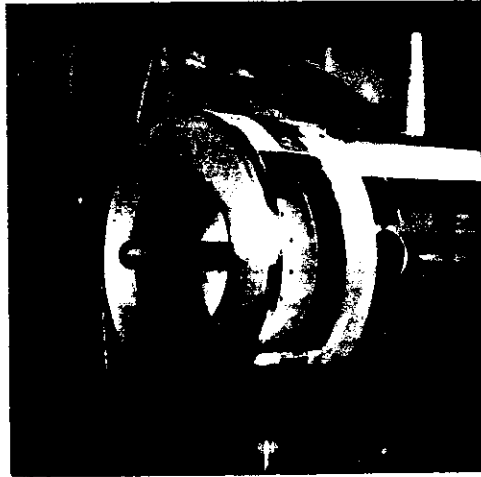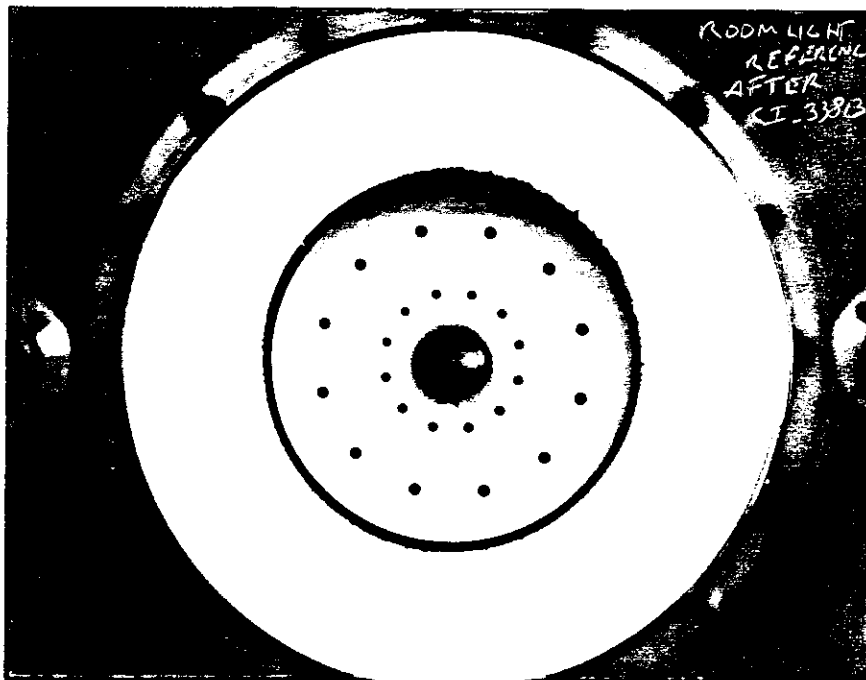
Figure 2-1

Exploded View of Thruster

Figure 2-2

Perspective View

End View

Room Light Photographs of

Full Scale "Benchmark" Thruster

in Plexiglas Tank

Figure   2-3

holes. Since the flow through the orifices is sonic, the mass flow rate is proportional to the pressure in the propellant plenum upstream of the orifices. The range of mass flows used was from 1.0 to 15.5 g/s. Argon was used as propellant for all test series. The mass flow rate calibration procedure is discussed in appendix A.

To insure that the asymmetric behavior was not induced by the apparatus, every effort was made to insure that the thruster geometry and mass injection were symmetric. The mass injection annulus at the cathode base was measured to have a uniform opening to within 2%. The plena in the Plexiglas distribution plate behind the backplate were enlarged to provide more uniform propellant distribution to the annulus and the outer holes. It is difficult to assess the uniformity of the flow through the annulus, but the standard deviation between the flow through the 12 outer holes was measured with a variable area flow meter to be about 2%. The cathode was centered in the anode orifice to within .5% during thruster assembly with a template designed for the purpose. Finally, the view port in the anode column was used only for side view photographs and movies. End view photographs did not show an effect of the view port on luminosity. However, magnetic field probes showed a 20% increase in the magnetic field on the side of the chamber near the view port, presumably due to the absence of current in the missing portion of anode column. Therefore, except when the viewport was necessary, the cylindrically symmetric anode column was used.

All experiments were conducted in a Plexiglas vacuum chamber 1.83 m long with .92 m inner diameter. The tank was evacuated to pressures less than 5×10^{-5} torr by a six-inch diffusion pump and two mechanical roughing pumps. An electrically controlled probe rack with three degrees of translational freedom, as well as rotational motion in the horizontal plane, was used to precisely position the magnetic field probes.

2.1.2 Power Supply

The MPD thruster is operated in a pulsed mode with pulses of duration sufficient to achieve quasi-steady operation. The current pulse is supplied by an L-C ladder network configured to

produce rectangular pulses. This pulse-forming network (PFN) consists of 80 stations, each with four 26.1 μF capacitors in parallel. The stations are all linked sequentially in one ladder, with a 1.5 μH inductor between each station. When the output to the thruster is connected to the middle of the ladder, in essence creating two parallel arms of 40 stations, the PFN produces a 1 ms pulse with 8 amperes of current for every volt the capacitors are charged. When the output is attached to the end of the ladder, it produces a 2 ms pulse with 4 amperes of current for every volt charged. The PFN is connected to the thruster though an electrolytic ballast resistor that matches the impedance of the bank to that of the thruster.[16]

To fire the thruster, a DEL High Voltage DC Power Supply is used to charge the PFN to the desired voltage. When the firing sequence is triggered, a high voltage pulse from an electronic circuit opens a high speed solenoid valve that begins injecting propellant. Propellant is injected for about 20 ms to allow the propellant flow to stabilize. Then the firing sequence circuit sends a high voltage pulse to open another high speed valve that begins flooding the gas switch with nitrogen. When the pressure in the switch reaches the Paschen limit, the gas in the switch breaks down, completing the circuit between the PFN and the thruster. The minimum charging voltage for which breakdown occurs in the thruster is about 500V, corresponding to a minimum current of 2 or 4 kA, depending on the PFN configuration. The maximum current used in this study was 30 kA.

2.2 Diagnostics

The principle types of data collected in this study were terminal voltage and total current measurements, time-integrated photographs, high speed photographic sequences, and magnetic field probe measurements. The voltage, current and magnetic field data were collected on Nicolet 2090-IIIA digital oscilloscopes, located in a grounded Faraday cage. The oscilloscope data were transferred to a Hewlett Packard 9816 computer, where it was stored on 3.5" floppy disks using a data acquisition program, FASTTRANS, written by Jay Polk. The digital traces were later analyzed by a program called UBERCRANK, also written by Jay Polk[18] and extensively modified

18

for this work. The data were ultimately archived on computer tape cassettes.

2.2.1 Terminal Voltage and Current

Thruster terminal voltage and total current were measured simultaneously over the duration of the discharge. The voltage was measured differentially across the anode and cathode using two Tektronix 6013A 1000:1 high voltage probes. The probes were calibrated and compensated regularly and were found to retain their calibration quite well.

The current was measured using a low inductance copper sheet shunt in series between the pulse-forming network and the anode of the thruster. The differential voltage across the shunt had been previously calibrated at one volt per 4.2 kA current. Previous experience has shown the terminal voltage and current to achieve steady-state behavior well within a few hundred microseconds. The value of steady state voltage and current for a given shot was measured by finding the average value from 700 μs - 800 μs after the beginning of the current trace.

2.2.2 Time-Integrated Photographs

Photographs of the discharge, exposed throughout the entire pulse, were made with a Burleigh Brooks Super Cambo bellows camera on black-and-white Polaroid Type 57 film. The camera has an f/5.5 lens with a 50 cm focal length. Various Wratten neutral density filters were used in conjunction with the aperture setting to achieve the proper exposure. In addition, a 488 nm filter with a 1 nm band pass was often used to image radiation from the 487.99 nm transition singly-ionized argon. Studies with 600 nm and 330 nm filters to view neutral and doubly ionized argon, respectively were also attempted, but the 10 nm bandpass of these filters transmits so much light from sources other than the transition of interest that it is impossible to unambiguously interpret the results.

To determine whether asymmetric distributions in the 488 nm line were accompanied by similar distributions in other lines, spectrographs were taken with a Steinheil GH 3 prism

19

spectroscope. Spectra from both end view and side view, looking into the chamber through the anode column view port, were recorded on black-and-white type 47 Polaroid film. The spectral range was limited to greater than about 400 nm by the glass optics and less than about 660 nm by the film sensitivity. Wavelengths of the observed lines were identified with reference spectra from an argon Geissler tube and by comparison with previously identified spectra.

2.2.3 High Speed Photographic Sequences

High speed photographic sequences of the discharge were obtained with a Hycam model 41-0004 high speed movie camera on Kodak type 7277 4-X reversal black-and-white 16 mm film. The film gives a positive image when developed. To retain as much detail as possible for the large print size presented in this thesis, the prints were made directly from the developed film, yielding reverse color prints. Therefore, luminous regions appear dark in all photographic sequences presented.

With the aid of a special camera head that puts four split frames on the space of every normal frame, framing rates of up to 24,000 frames/s were obtained. Since the camera shutter is opening for the first half of each framing period and closing for the second half, a plot of exposure versus time would look like a triangular wave. The effective exposure time for each frame is 40% of the framing period. The camera lens has a 50 mm focal length, and the camera optics allow a maximum effective aperture of f/3.3. Movies were taken from both an end and a side view, both unfiltered and with the 488 nm filter. Thruster mass flow was varied from 3.5 to 15.5 g/s with currents of 4 kA to 30 kA. Below a value of the parameter J^2/m equal to 10 kA^2s/g, the intensity of 488 nm light is too dim for reliable exposures with the filter.
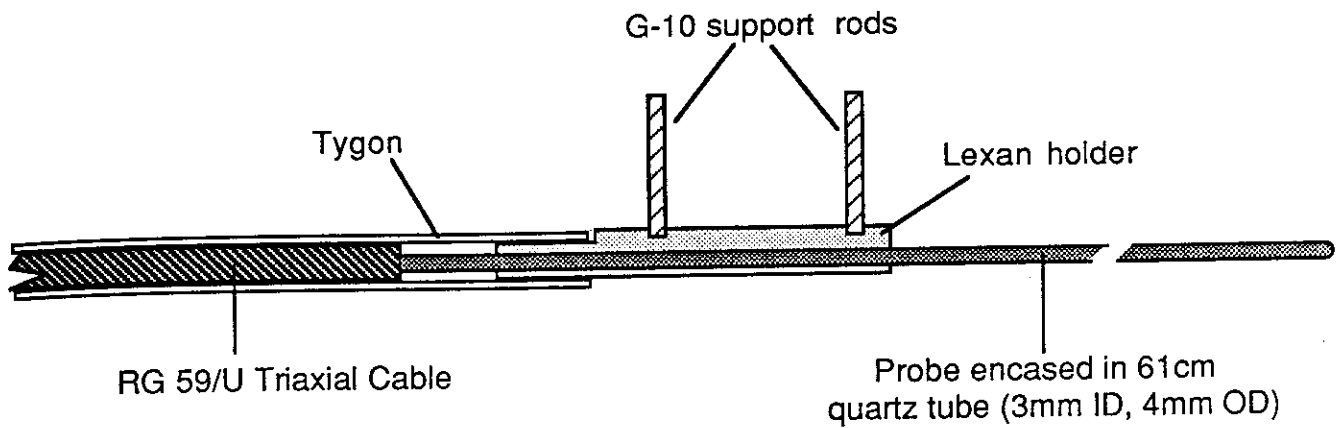
Since the camera does not reach top speed until near the end of a roll of film, an electronic system was devised with the aid of George Miller to delay the firing of the thruster a set amount of time after the camera starts moving the film. The system uses a Wavetek signal generator to generate a triggered square-wave pulse with a period equal to the desired delay. On the up stroke of

20

the pulse, the camera is set in action, and on the down stroke, the thruster firing sequence is initiated. The circuit diagram of this system is presented in appendix B. Since only a few centimeters out of 100 feet of film are actually exposed, the same roll was reused to record four discharges. Using the film more than four times risks damaging the film.
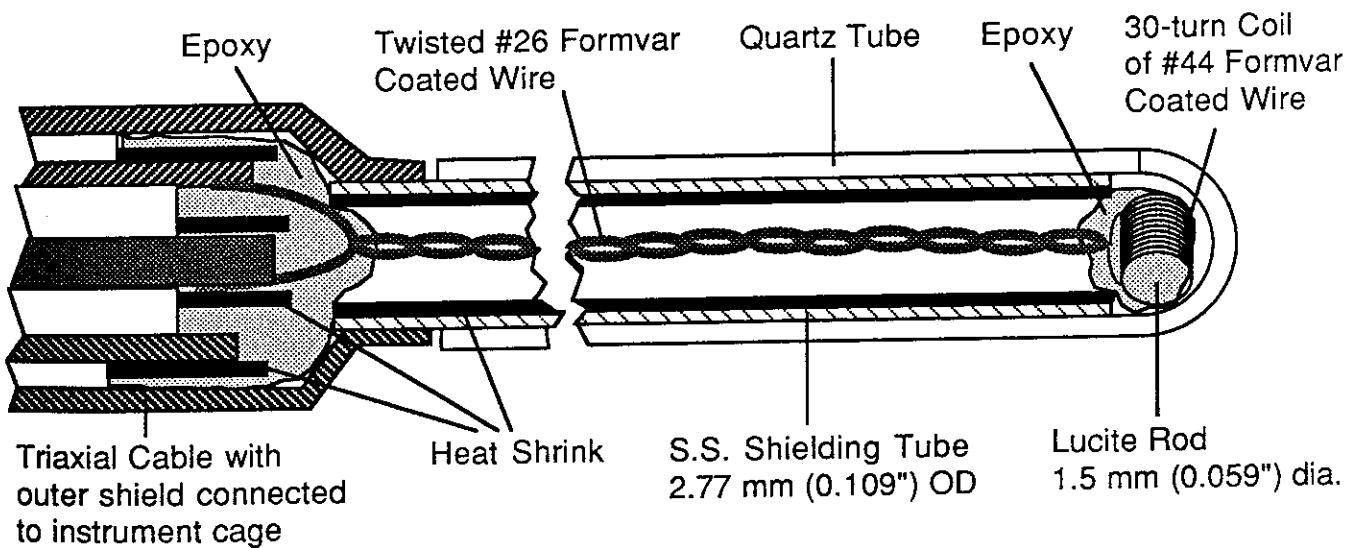
Two methods were used to determine the film speed. In the first method, the distance was measured between timing marks made on the edge of the film by an LED that produces 20 μs pulses at a rate of 1 kHz during camera operation. The chief drawback to this system was that, although the framing rate could be determined to within 0.5%, there was no way to tell when, relative to the start of the thruster current pulse, the first frame was exposed, so the location of any frame during the current pulse could not be known to better than one framing period. In the second method, a photomultiplier tube was mounted over the camera viewfinder to collect light that bleeds through the film as it is being exposed. The output of the photomultiplier tube, recorded on a digital oscilloscope simultaneously with the thruster current, shows to within 1 μs when each frame is being exposed during the current pulse. In addition, the same arrangement was used with the camera turned off and the shutter open to record the relative total intensity of 488 nm light over the course of the discharge for several different conditions.

2.2.4 Magnetic Field Probes

To investigate the correspondence between asymmetric luminosity and current patterns, a set of four magnetic field probes was constructed. Since all magnetic fields in a self-field thruster are created by the current pattern, asymmetric magnetic fields are an indication of asymmetric current patterns. A magnetic field probe is essentially a small coil of wire encapsulated in a closed quartz tube (Figure 2-4). The coil produces an emf that is proportional to the change in magnetic flux along its axis with respect to time. By using an active electronic integrator to integrate the probe signal, a voltage that is proportional to the magnetic field strength at the location of the probe can be obtained. The calibrations for the magnetic field probe and integrator pairs are on the order of

G-10 support rods

Tygon

Lexan holder

RG 59/U Triaxial Cable

Probe encased in 61cm
quartz tube (3mm ID, 4mm OD)

Magnetic Field Probe

Epoxy

Twisted #26 Formvar
Coated Wire

Quartz Tube

Epoxy

30-turn Coil
of #44 Formvar
Coated Wire

Triaxial Cable with
outer shield connected
to instrument cage

Heat Shrink

S.S. Shielding Tube
2.77 mm (0.109") OD

Lucite Rod
1.5 mm (0.059") dia.

Close-up Of Probe

Figure 2-4

.3 Tesla per Volt and are accurate to within 2%. The characteristics of the probes and integrators as well as details about the calibration procedure are discussed in Appendix C.

The four probes were positioned at an equal axial distance from the backplate and at an equal radial distance from the thruster axis, but were at four different azimuthal positions, all 45° from horizontal. The axes of the probe coils were oriented in the azimuthal direction. The probes were mounted in an acrylic ring by means of sliding support rods, allowing an unobstructed end view of the thruster chamber and freedom in radial positioning. The support ring was mounted on the tank's probe rack, which was used for axial positioning. The radial positions of the probes were checked visually and are accurate to within 1% which, combined with the 2% uncertainty in calibrations and a 1% uncertainty induced by coil orientation, produced a worst-case total of 4% uncertainty in the magnetic field measured by one probe relative to that measured by the other probes. Each probe was connected to its own integrator, and the output signals from the integrators were recorded on digital oscilloscopes, which in turn transfer the data to the Hewlett Packard computer for analysis. The overall experimental arrangement is shown in Figure 2-5.
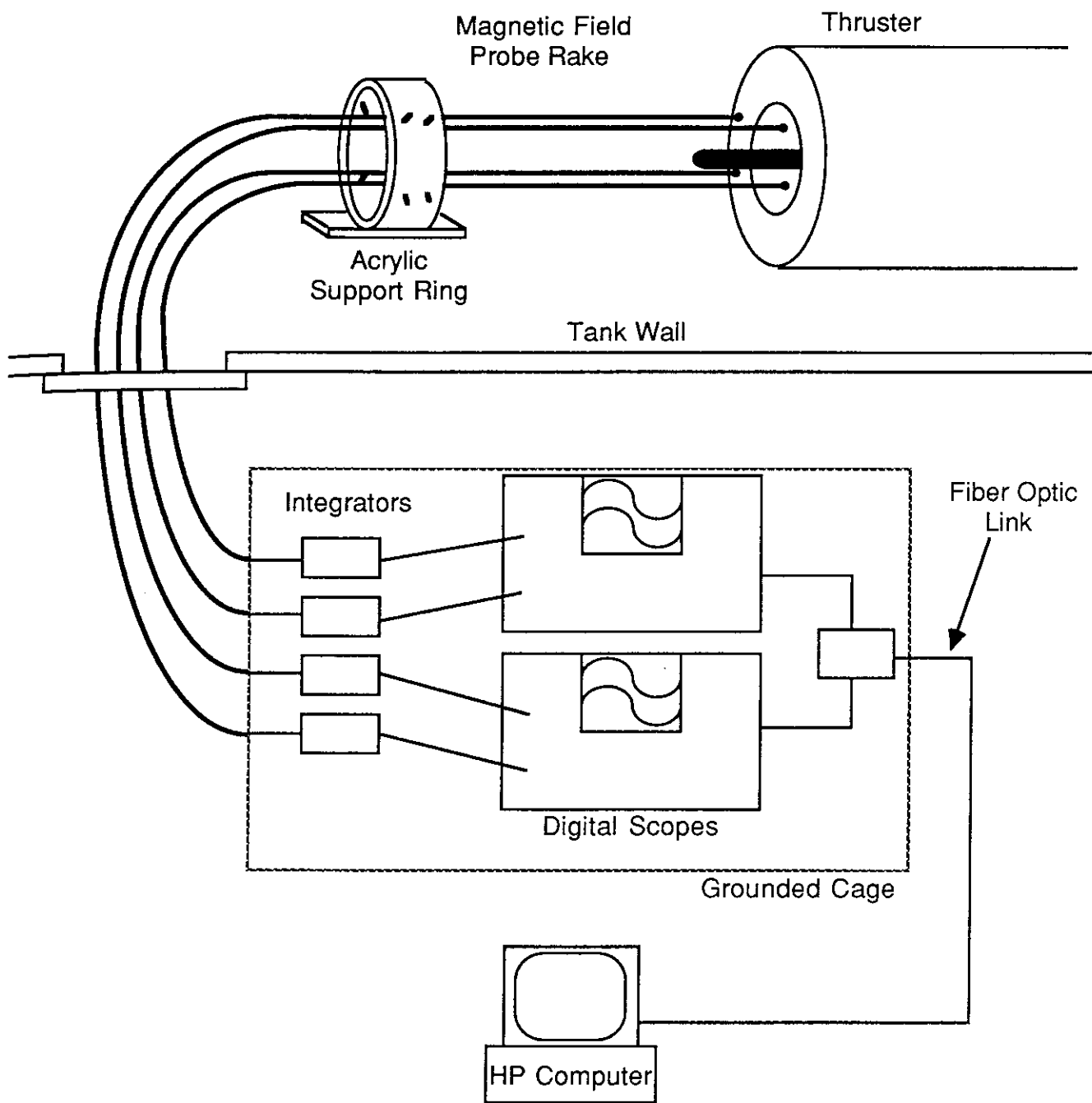
Magnetic Field Probe Rake Arrangement

Figure 2-5

Chapter 3

LUMINOSITY STUDIES

3.1 Introduction

Because measurement of luminosity for an entire plume is possible in a single photograph, luminosity studies provide an excellent way to assess the overall symmetry of each discharge, as well as to characterize the structure of an asymmetric pattern. Therefore, extensive studies of the luminosity were conducted over the following matrix of parameters: time-integrated or time-resolved, end view or side view, and filtered or unfiltered.

Time-resolved photographic sequences generally prove more informative than time-integrated photographs. Time-integrated photographs give no indication whether the asymmetric behavior is time dependent or not, a crucial question to be answered. If the asymmetric behavior is time dependent, three factors will affect how asymmetric a discharge looks in a photograph: how severe the asymmetry is, how long it lasts, and how bright the asymmetric phase of the discharge appears, compared with more symmetric portions. Therefore, it is imperative to perform time-resolved studies to investigate the development of the discharge, and these will be presented in the third section of this chapter. However, time-integrated photographs, which will be presented in the next section, are much simpler to obtain and do provide useful information.

Most of the photographic studies were conducted through a Pyrex window in the end of the vacuum tank for several reasons. First, the azimuthal distribution is most easily viewed from an axial perspective. Also, it is not possible to observe asymmetric discharge patterns from the side if the discharge is skewed toward or away from the viewer; nor is it possible to view the azimuthal structure of the pattern from the side. In addition, end view photographs do not require the view port to be mounted in the anode column. However, the side view does allow interpretation of the axial extent of the asymmetric behavior and was occasionally used to complement the end view studies.

As was stated in Chapter 2, the filtered studies all used the 488 nm argon ion line filter. The main advantage of filtered over unfiltered photography is that the distribution of 488 nm light is related to the distribution of singly ionized argon. The "intensity" of a particular line is proportional to the integral of the number density of the excited state of the ion, n_j, along the line of sight:

$$I_{ji} = h\nu_{ji}A_{ji} \int n_j \, dx \qquad [W/m^2],$$

where Planck's constant, h, the frequency of the light, ν, and the transition probability, A, are constants for a given transition. For a plasma in equilibrium, n_j would be given by a Boltzmann distribution:[19]

$$n_j = n_+ \, (g_j/Z(T)) \, e^{-\varepsilon/kT},$$

where T is the electron temperature and ε is the energy of the excited state above ground state. Thus, the 488 nm line intensity is linked to the number density of argon ions.
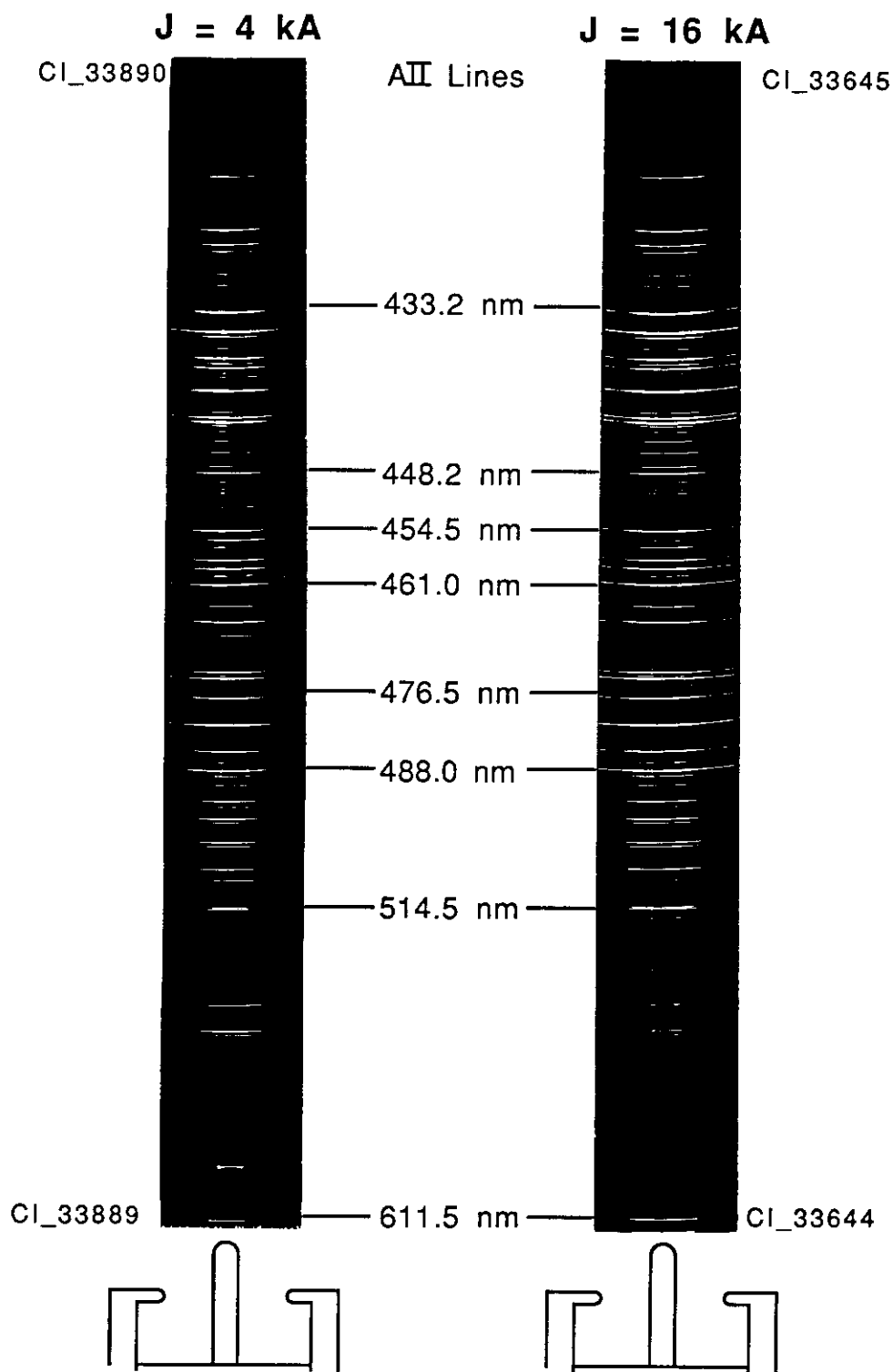
However, several caveats must be made before interpreting the observed 488 nm intensity distribution as the argon ion distribution. First, the plasma is not in equilibrium, so the number densities of the excited states may be different than that predicted by the Boltzmann distribution,[20] although they will probably still be proportional to the total ion number density. Second, the observed intensity is integrated along the line of sight, so care must be taken to assign the source of the radiation to its proper location. Third, the number density of the excited state is a strong function of electron temperature. Therefore, azimuthal gradients of intensity could indicate azimuthal gradients of electron temperature as well as of ion number density. Finally, the 1 nm bandwidth of the filter admits bremsstrahlung continuum radiation, as well as the desired light from the 488 nm transition. Since the intensity of bremsstrahlung is proportional to the square of the electron number density, it becomes an important contribution in regions where the electron number density is high, such as near the cathode surface and in the jet off the cathode tip.[17] In any case, since axisymmetric distributions of temperature and number density are expected in a symmetric discharge, asymmetric intensity distributions do indicate asymmetric temperature and/or number density distributions.

Figure 3-1 shows a comparison between the spectrum of a discharge taken at 4 and 16 kA at 5.9 g/s, conditions under which filtered photographs look asymmetric and symmetric, respectively. The spectra were taken from the side at an axial position 2.4 cm from the backplate and are time-integrated. Although only a few lines are identified for clarity, virtually all the lines visible at these currents are from transitions of singly-ionized argon. Careful inspection of the 4 kA spectra shows that all the argon ion lines are skewed to the left of the cathode shadow, similar to the 488 nm line; whereas all lines are symmetric about the cathode in the 16 kA spectra. These spectra demonstrate that the distribution of 488 nm radiation is indicative of the distribution of all argon ion radiation under these conditions.

The principle reason for looking at unfiltered luminosity patterns is that the 488 nm light alone becomes too dim to adequately expose the film in high speed sequences of low $J^2/\dot{m}$ conditions. Since the spectra show that virtually all the light emitted at these conditions is from argon ion transitions, the unfiltered intensity distribution should be similarly indicative of the argon ion distribution. In fact, at thruster conditions for which exposure is not an issue, the filtered and unfiltered luminosity patterns look virtually identical.
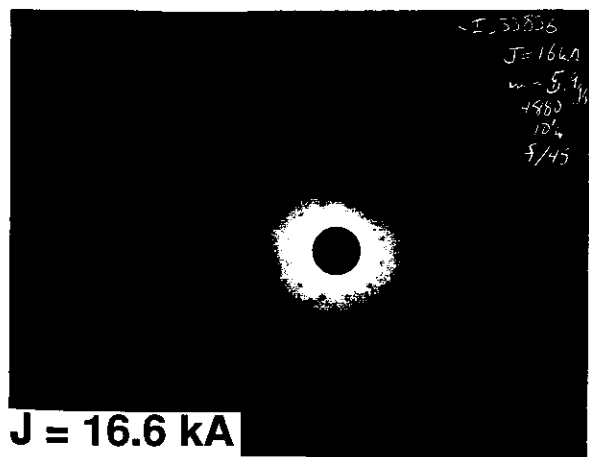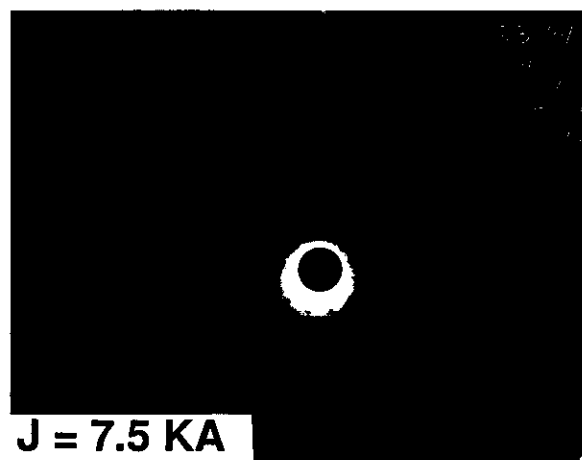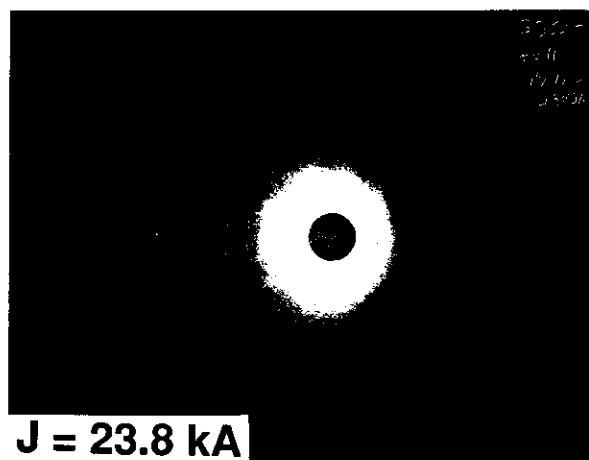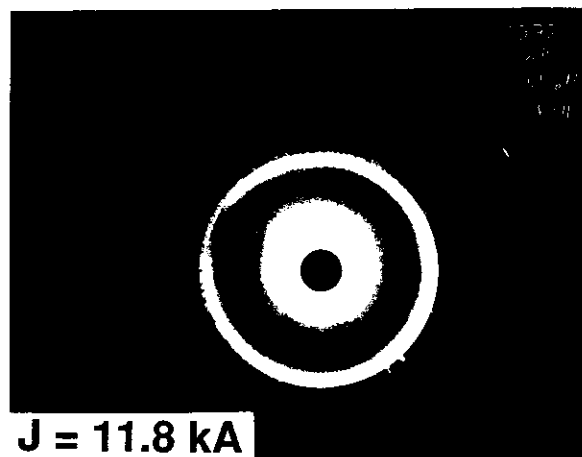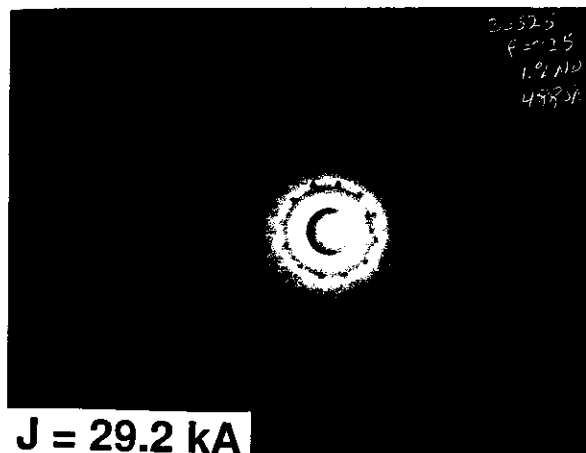
3.2 Time-integrated Photographs

A series of time-integrated photographs over a range of currents at the same mass flow demonstrates the existence of asymmetric behavior at low currents (Figure 3-2). It should be noted that, because the overall intensity of 488 nm light changes considerably for different operating conditions, exposure levels were adjusted to give the best contrast and are not the same in different photographs. The dark circle at the center of these end view photographs is the tip of the cathode. Two rings of mass injection holes appear around the cathode, of which the inner set is unused. The ring outside the outer injection holes is the inner edge of the anode, the face of which can be seen in the brighter photographs. The asymmetry is most pronounced at the lowest current and becomes gradually less severe as the current is raised. There is an apparent threshold at about 16 kA, above

J = 4 kA

CI_33890

AII Lines

J = 16 kA

CI_33645

— 433.2 nm —

— 448.2 nm —

— 454.5 nm —

— 461.0 nm —

— 476.5 nm —

— 488.0 nm —

— 514.5 nm —

CI_33889

— 611.5 nm —

CI_33644

Steinheil Spectrographs

Side View 2.4 cm from backplate, $\dot{m}$ = 5.9 g/s

Figure 3-1

J = 29.2 kA

J = 11.8 kA

J = 23.8 kA

J = 7.5 KA

J = 16.6 kA

J = 3.9 kA

End View,   488 nm Light,   5.9 g/s

Figure   3-2

which the discharge appears quite symmetric. Similar degrees of asymmetry at different mass flow rates, but at the same value of $J^2/\dot{m}$, indicate that the asymmetric behavior scales with this parameter. This scaling will be discussed further in the next section.
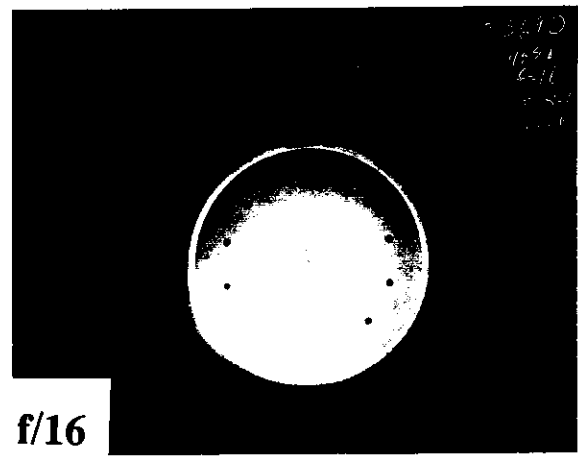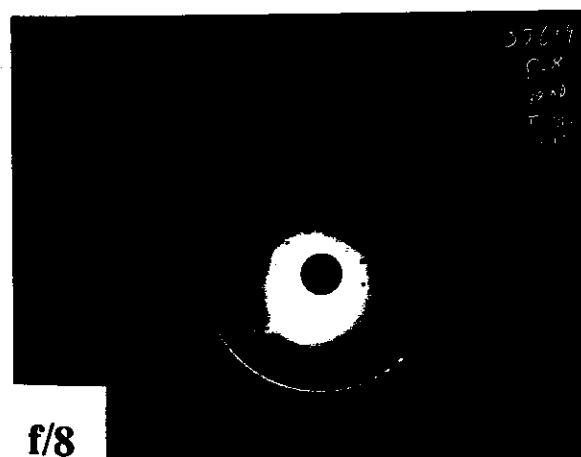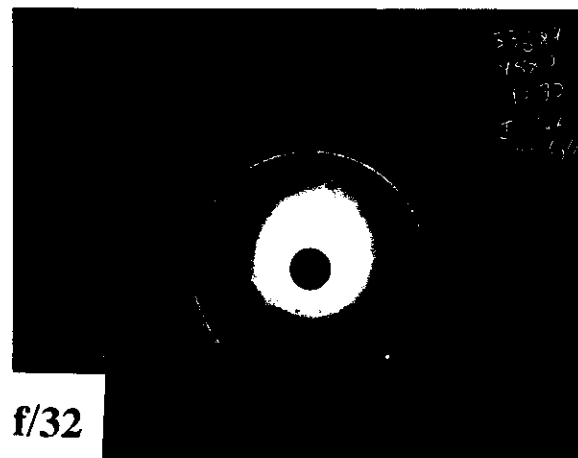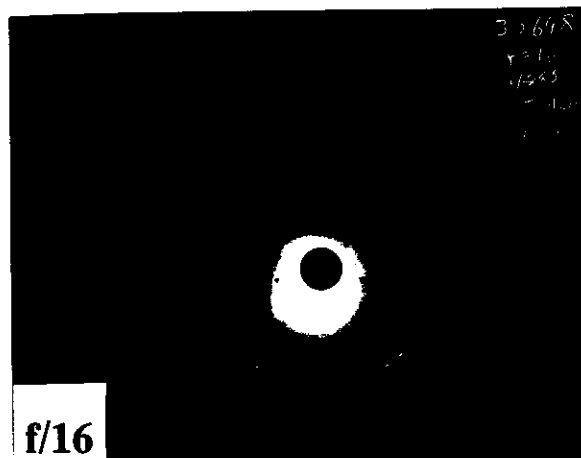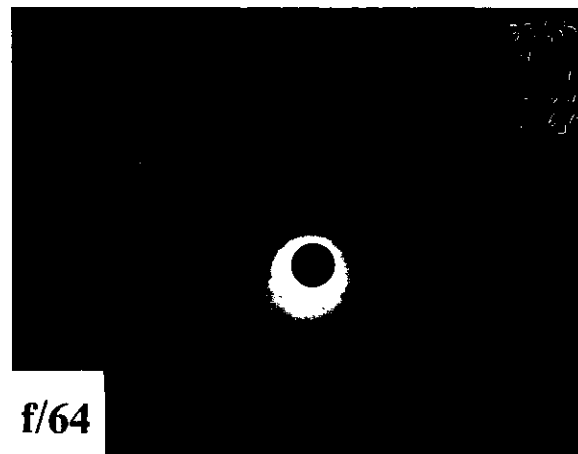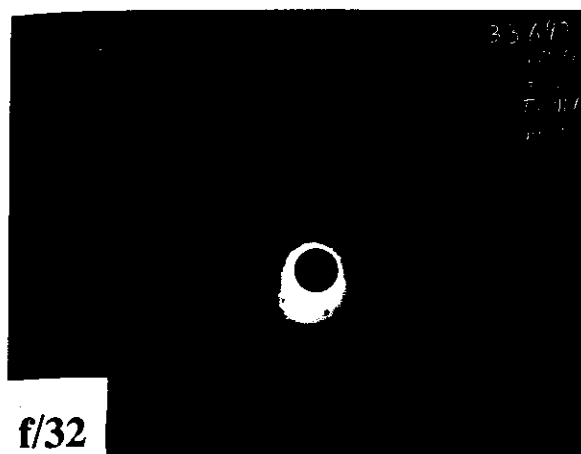
Side view photographs in Figure 3-3 show that the luminosity distribution is asymmetric at all axial positions, but is most pronounced inside the thruster chamber. In this view, the backplate is to the right, so the flow moves to the left. The anode is the dark vertical bar at the center of the image. The curved boundary at the left is the edge of the vacuum tank window.

In both views, a symmetric discharge corresponds with a sharply defined outer edge of the luminosity, and a definite structure appears within the discharge. At the highest current in the end view, this structure resolves into a band around the cathode that has been commonly referred to as "the barrel". In a study of thruster limitations at high currents, Rudolph[21] linked the appearance of the barrel to the appearance of terminal voltage oscillations, referred to as the "onset" condition. Measurements showed the bright band to be an area of high Hall parameter, high electric field strengths and mostly axial current conduction. The slightly darker region just inside that is an area of lower Hall parameter with more radial current conduction, since the rising charged particle number densities cause more collisions. The bright region immediately adjacent to the cathode is a region of high number density, emitting a relatively large amount of continuum radiation. This barrel phenomenon does not occur at lower currents, presumably because of the relatively low magnetic fields produced.

Photographs taken with different apertures at the same conditions (Figure 3-4) demonstrate the sharp azimuthal gradients in luminosity that accompany the asymmetric behavior. Since the largest aperture admits 16 times as much light as the smallest one used, the photographs show that the brightest portion of the plasma emits at least 16 times as much 488 nm radiation as the plasma a few degrees away in the azimuthal direction. Assuming, for simplicity, a Boltzmann distribution, this difference corresponds to more than an order of magnitude difference in ion number density at constant electron temperature, or a 35% difference in electron temperature if the ion number density

J = 30.5 kA

J = 12.8 kA

J = 25.1 kA

J = 8.0 kA

J = 16.9 kA

J = 4.0 kA
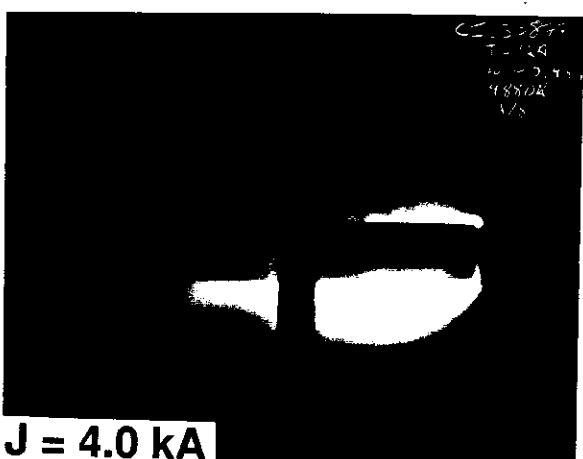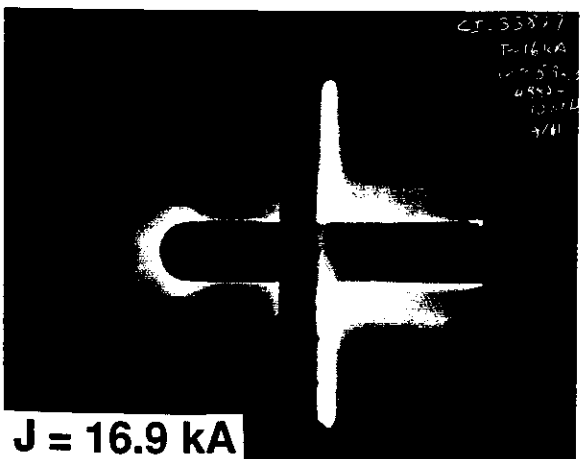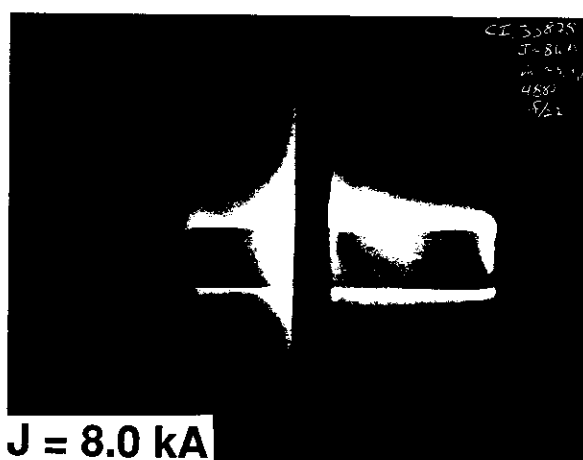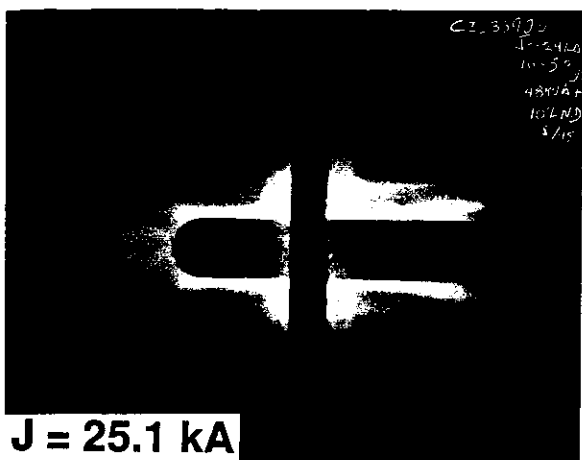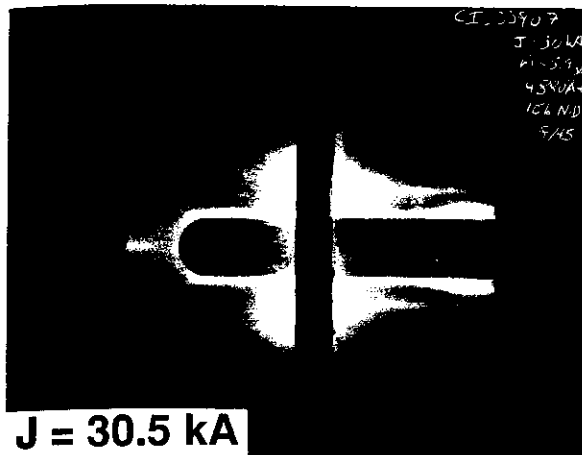
Side View, 488 nm Light, 5.9 g/s
Figure 3-3

f/32   f/64

f/16   f/32

f/8   f/16

J ≈ 4 kA, ṁ = 10.3 g/s   J ≈ 8 kA, ṁ = 5.9 g/s
488 nm Light
Figure 3-4

were constant.

Finally, the direction of the bulge in the asymmetric discharges changes over consecutive discharges. Figure 3-5 shows a plot of the angle of the center of the luminosity bulge at 4 kA for sets of shots taken on two different days. The second set of discharges was made with the magnetic field probes inserted in the thruster. The presence of the probes had no affect on the asymmetric behavior, neither attracting nor repelling the bulge. The azimuthal position of the asymmetry may change from shot to shot, but it is not randomly oriented. Individual series exhibit preferred bulge positions. However, these preferred positions may change, especially if the thruster is disturbed by cleaning or merely handling. Such behavior indicates that the position of the asymmetry is controlled by asymmetric aspects of the thruster that may vary with time. Since efforts were made to ensure macroscopic thruster symmetry, and since such macroscopic factors would most likely be constant with time, the direction of the asymmetry must be determined by a minor, changeable factor. Two candidates for this factor are the condition of electrode surfaces and fluctuations in the mass injection distribution. Both will be investigated in the next chapter.

3.3 Time-resolved Photographic Sequences

With the time resolution afforded by the photographic sequences, it is possible to investigate the first question proposed in the introduction - whether or not the asymmetric behavior is steady or time dependent in nature. In addition to this primary question, the sequences provide information about the character of the discharge as it develops throughout the pulse.

Figures 3-6, 3-7, and 3-8 illustrate the range of behavior typically seen in the photographic sequences. The thruster currents for the discharges shown are approximately 8, 16, and 24 kA, respectively. The mass flow was 5.9 g/s, and the 488 nm filter was used with the camera in an end view position for all three discharges. Since these are negative prints, the unilluminated cathode tip appears as the light disk in the center of each frame. The outer mass injection holes can be seen in many frames of the 16 kA sequence as small, light disks about four cathode radii from the center.
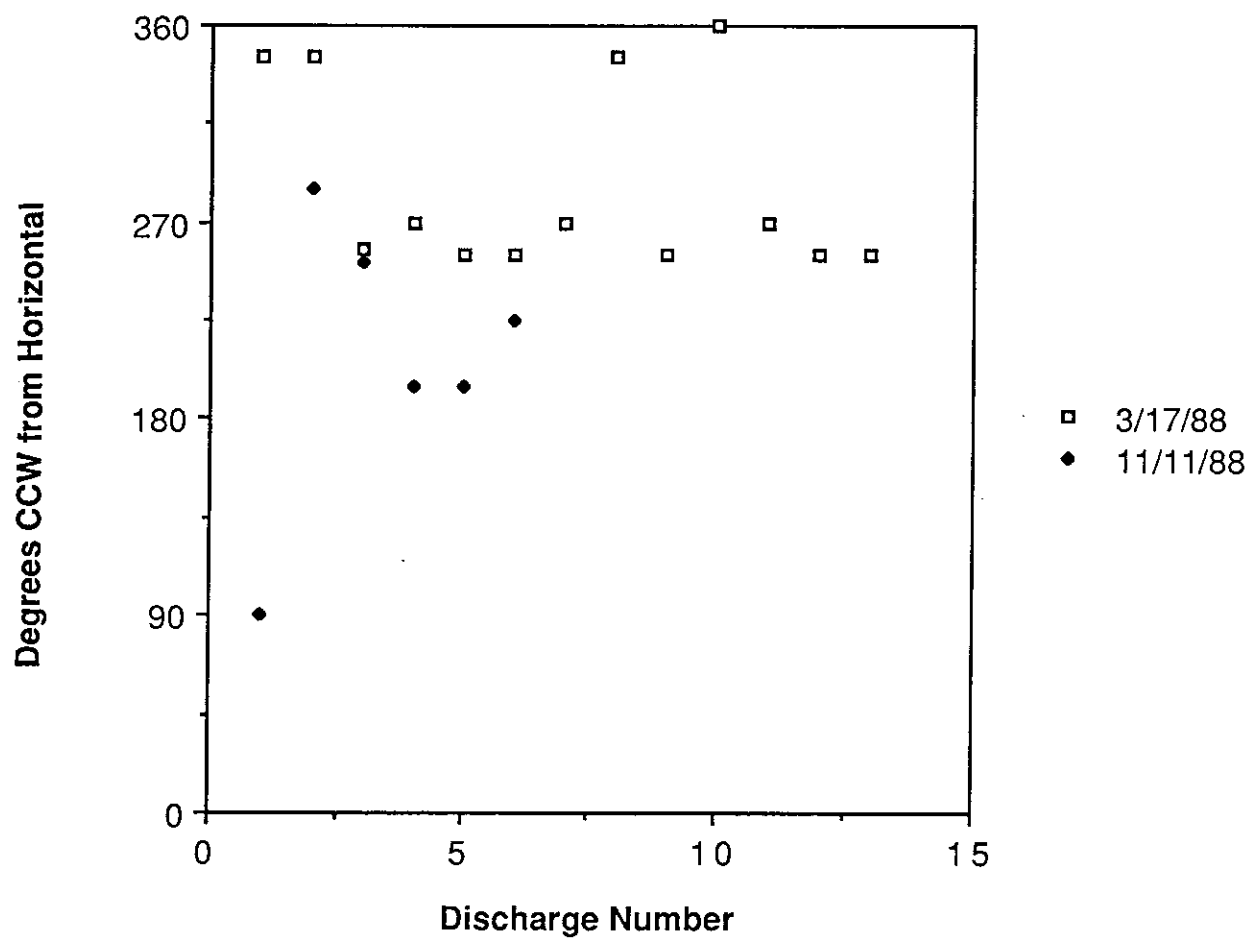
Angular Position of Asymmetry for 4 kA Discharges

Figure 3-5

Fr.	Time (μs)		Fr.	Time (μs)		Fr.	Time (μs)	
1	30		11	530		21	1030	
2	80		12	580		22	1080	
3	130		13	630		23	1130	
4	180		14	680		24	1180	
5	230		15	730		25	1230	
6	280		16	780				
7	330		17	830				
8	380		18	880				
9	430		19	930				
10	480		20	980				

CI_33732

Uncertainty in Absolute Times = ± 25 μs
Period Between Frames = 49.8 μs ± .2 μs

J = 7.52 kA, $\dot{m}$ = 5.9 g/s,   488 nm Light

Figure 3-6

Fr.	Time (μs)		Fr.	Time (μs)		Fr.	Time (μs)	
1	30		11	510		21	990	
2	80		12	560		22	1040	
3	130		13	610		23	1090	
4	170		14	660		24	1140	
5	220		15	700		25	1180	
6	270		16	750		26	1230	
7	320		17	800		27	1280	
8	370		18	850		28	1330	
9	410		19	900				
10	460		20	940				
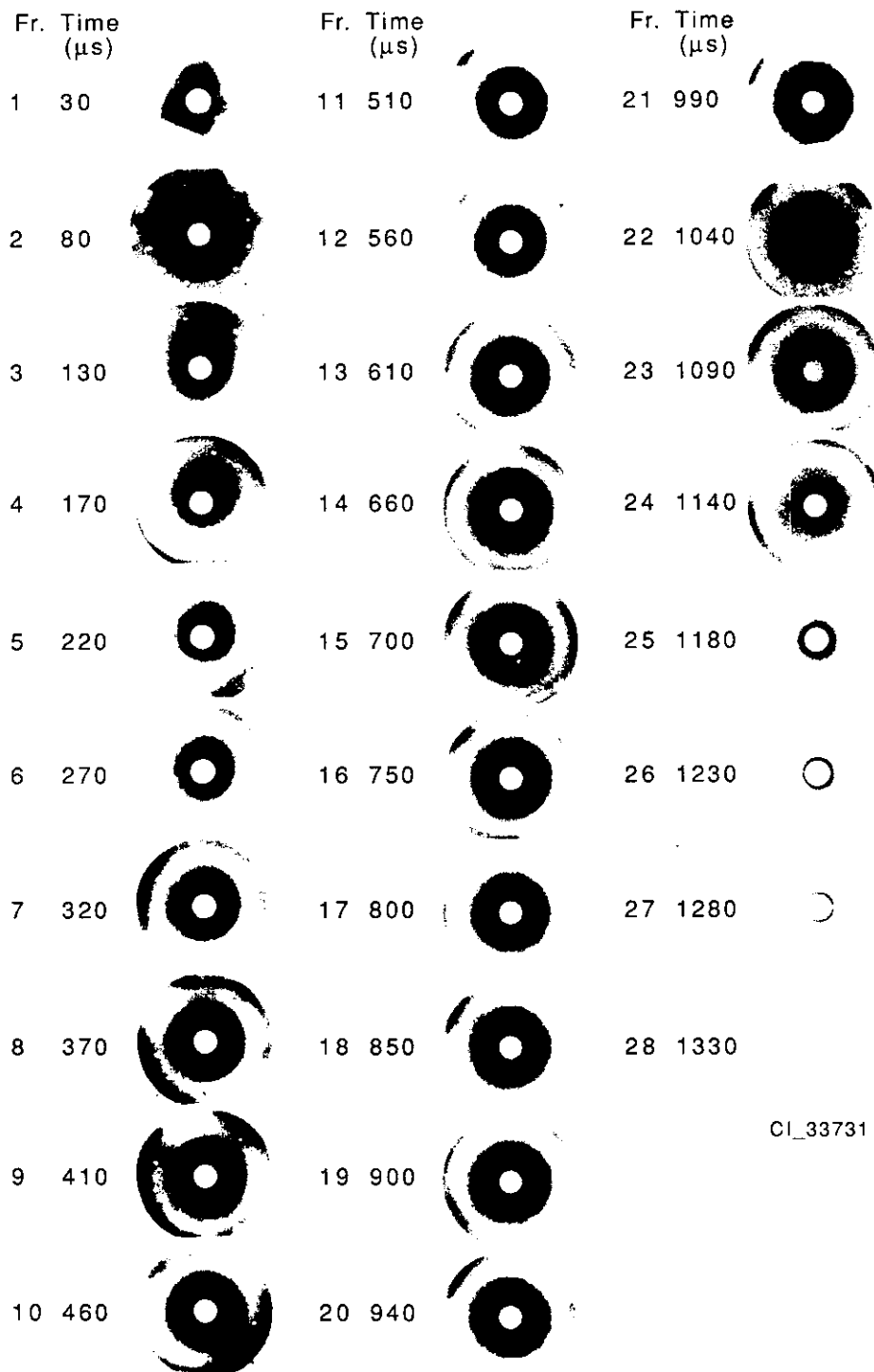
CI_33731

Uncertainty in Absolute Times = ± 25 μs
Period Between Frames = 48.1 μs ± .2 μs

J = 15.7 kA,   ṁ = 5.9 g/s,   488 nm Light
Figure 3-7

Fr.	Time (μs)		Fr.	Time (μs)		Fr.	Time (μs)	
1	20		11	470		21	910	
2	60		12	510		22	950	
3	110		13	550		23	1000	
4	150		14	600		24	1040	
5	200		15	640		25	1080	
6	240		16	690				
7	290		17	730				
8	330		18	780				
9	380		19	820				
10	420		20	870				

CI_33822

Uncertainty in Absolute Times = ± 20 μs
Period Between Frames = 44.5 μs ± .2 μs

J = 24.5 kA, $\dot{m}$ = 5.9 g/s, 488 nm Light
Figure 3-8

The maximum radial extent of the luminosity in that sequence demarcates the inner edge of the anode. In the time-integrated photographs, an 8 kA discharge appears asymmetric, a 24 kA discharge appears symmetric, and a 16 kA discharge is at the transition.

Although the time-integrated photographs display symmetric discharges at higher currents, it is apparent from the three sequences shown here that the discharge is initially asymmetric at all currents. At 24 kA, this asymmetric behavior is a mild and short-lived transient, lasting for only the first two frames. In fact, at 30 kA it is difficult to discern asymmetric behavior, even in the first frame, so any transient behavior lasts less than one framing period at such a high current. In the 16 kA sequence, the asymmetric behavior of the luminous region around the cathode is also transient, although this transient persists longer and is somewhat more severe. At 8 kA, the discharge pattern gradually collapses down to the cathode in a thin luminous ring. The ring luminosity originates from continuum radiation as well as the 488 nm transition since, as was stated before, the layer immediately adjacent to the cathode has been shown to have relatively high electron number densities. Although gross asymmetry disappears after the first few frames in this sequence, a slight bulge does remain on the lower right hand edge of the cathode ring throughout the discharge. Unfortunately, the overall amount of 488 nm light emitted at currents below 8 kA at 5.9 g/s mass flow is at the lower limit of the film sensitivity, and efforts to "push" the development of the film do not reveal any more detail.

Unfiltered sequences at 4 kA reveal a surprising amount of activity in the luminous region surrounding the cathode. Figures 3-9a and 3-9b show the complete photographic sequence for a 2 ms discharge. Although the bulk asymmetry disappears within the first few microseconds, the discharge shows a strikingly non-uniform and unsteady azimuthal distribution throughout the pulse. Spikes and bulges, reaching as far as 4 cm in radius, appear out of the body of the luminous plasma, which has a radius of approximately 2.5 cm. These structures last between 50 and 250 μs and may appear in any direction. In unfiltered sequences at 8 kA, the spikes are less pronounced and less frequent, and they do not appear at all at higher currents. An unfiltered side view sequence

38

Fr.	Time (μs)		Fr.	Time (μs)		Fr.	Time (μs)	
1	20		11	500		21	970	
2	70		12	540		22	1020	
3	120		13	590		23	1070	
4	160		14	640		24	1120	
5	210		15	690		25	1160	
6	260		16	740		26	1210	
7	310		17	780		27	1260	
8	350		18	830		28	1310	
9	400		19	880		29	1360	
10	450		20	930		30	1400	

CI_33793

Uncertainty in Absolute Times = ± 20 μs
Period Between Frames = 47.7 μs ± .2 μs

J = 3.76 kA, ṁ = 5.9 g/s, All Light
Figure 3-9a

Fr.	Time (μs)		Fr.	Time (μs)		Fr.	Time (μs)	
31	1450		41	1930		51	2410	
32	1500		42	1980		52	2450	
33	1550		43	2020		53	2500	
34	1590		44	2070		54	2550	
35	1640		45	2120		55	2600	
36	1690		46	2170				
37	1740		47	2210				
38	1780		48	2260				
39	1830		49	2310				
40	1880		50	2360				

CI_33793

Uncertainty in Absolute Times = ± 20 μs
Period Between Frames = 47.7 μs ± .2 μs

J = 3.76 kA,   ṁ = 5.9 g/s,   All Light
Figure 3-9b

at similar conditions (Figure 3-10) does not reveal similar radial excursions of the luminous plasma, indicating that these features may be axially located in the anode plane. In the side view sequence shown, the backplate is to the right, the flow is toward the left, and the anode is the light vertical bar in the center. The outline of the cathode can be seen in most frames as a horizontal rod with its tip to the left.

A distinction should be made between these relatively local non-uniformities that are viewed only at the lowest currents and the gross asymmetric behavior seen during the initial transient. The magnetic field probe studies discussed in the next chapter will address the question of whether these local non-uniformities significantly affect the overall symmetry of the current distribution and whether gross asymmetric behavior persists throughout the pulse at low currents. It is clear, however, that asymmetric luminosity patterns occur initially at all, except possibly the highest thruster currents. It is also clear that the grossly asymmetric patterns are transient for all conditions, except possibly the lowest current. In addition, the initial overall asymmetries tend to be more severe and longer lived at lower currents for a given mass flow.

Since the framing cycle of the camera is not directly linked to the thruster firing circuit, the first frame of a sequence may be exposed anywhere within the first 50 μs of the discharge. Therefore, it is impossible to reliably capture the first few microseconds of the discharge when the luminosity pattern develops from a few breakdown locations. However, after taking into account the possible variation in the degree of breakdown development imaged by the first frame, examination of the first frame of each sequence shows that, at high currents, there are several initial lobes of radiating plasma distributed around the cathode. For example, in Figure 3-7, the images of four distinct jets are clearly visible in the first frame.

At low currents, the breakdown usually occurs only in one location, with no plasma visible on the opposite side. The first frame of the 8 kA discharge in Figure 3-6 shows a relatively late stage in the breakdown development, but nonetheless still exhibits a lack of radiation on the side of the cathode opposite the breakdown location. At the lowest charging voltages, terminal voltage

Fr.	Time (µs)		Fr.	Time (µs)		Fr.	Time (µs)	
1	30		11	500		21	960	
2	80		12	540		22	1010	
3	120		13	590		23	1060	
4	170		14	640		24	1100	
5	220		15	680		25	1150	
6	260		16	730		26	1200	
7	310		17	780		27	1240	
8	360		18	820		28	1290	
9	400		19	870		29	1340	
10	450		20	920		30	1380	
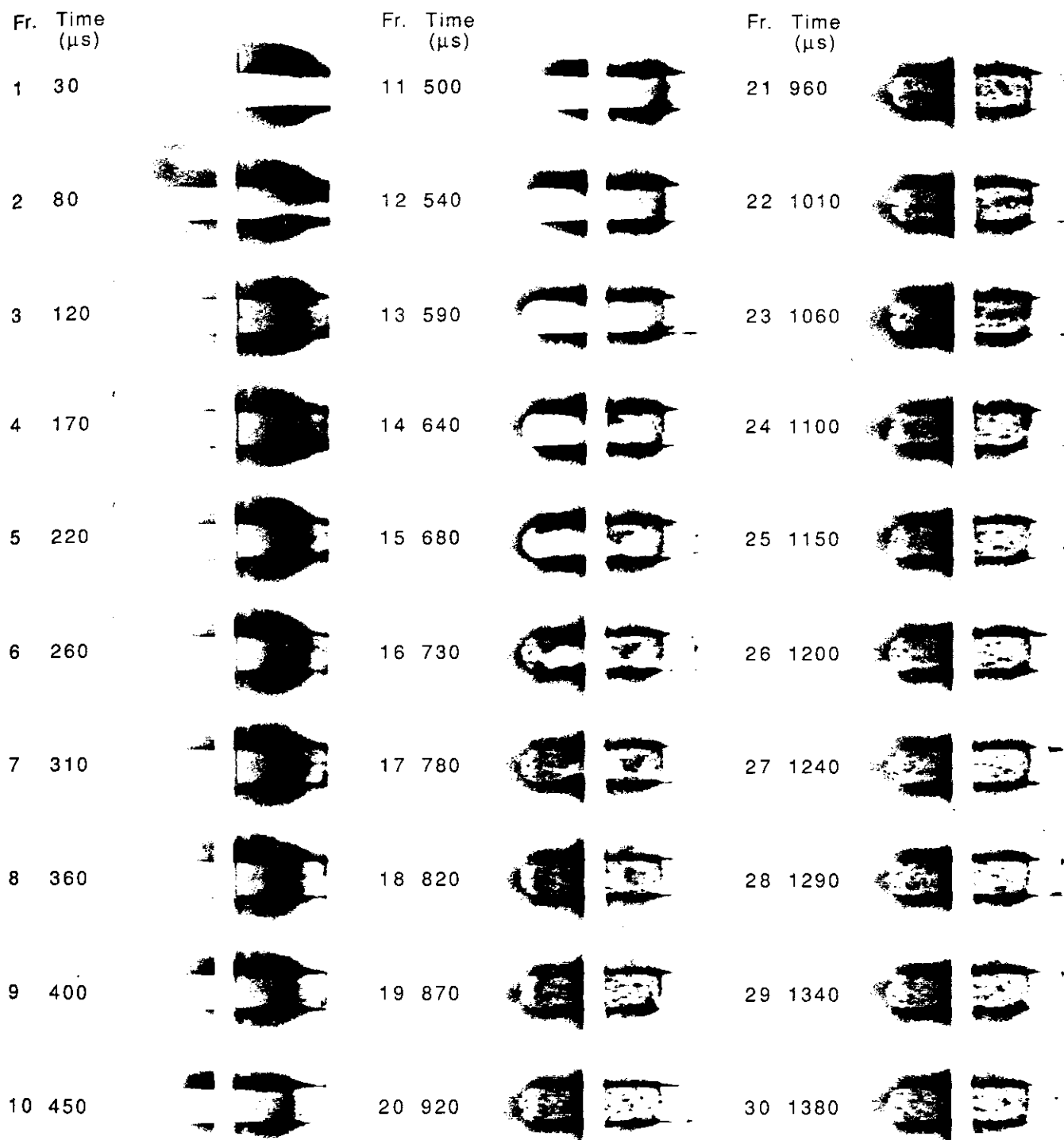
CI_33814

Uncertainty in Absolute Times = ± 25 µs
Period Between Frames = 46.6 µs ± .1 µs

J ≈ 4 kA, ṁ = 5.9 g/s, All Light, Side
Figure 3-10

measurements show that the propellant in the thruster often breaks down hundreds of microseconds after the gas switch experiences breakdown and applies the charging voltage across the thruster gap. Since the breakdown event occurs in only a fraction of a microsecond once initiated, the thruster is obviously having difficulty initiating the breakdown. Breakdown will occur at the first emission location that is able to ionize significant amounts of propellant, rather than simultaneously at several locations.

Since breakdown is initiated through field emission of electrons from cathode surface points, the luminosity initially appears near the cathode in all cases. Side view sequences show that the discharge initiates at the base of the cathode and rapidly spreads diagonally toward the inside edge of the anode (Figure 3-11). Because the breakdown transient involves large time derivatives of the magnetic field, the current patterns initially seek this lowest inductance configuration.[1]

The asymmetric transient is always associated with the beginning of the current pulse and is not intermittent or recurring. After breakdown, the discharge goes through a brief bright phase that will be discussed in a later section. The azimuthal location of maximum luminosity remains relatively motionless while the discharge spreads equally in both directions around the cathode. There is no evidence of rotating or oscillating spokes. At higher currents, there is often some luminous plasma all around the cathode with a bulge that persists for some time in one region (Figure 3-7). At the lower currents, there is often no visible plasma on one side of the cathode. Instead, a front of luminous plasma diffuses azimuthally around the cathode in both directions away from the region of maximum intensity (Figure 3-6).

3.4 Dependence of Luminosity Behavior on $J^2/\dot{m}$

Several of the luminosity phenomena that are manifest in the photographic sequences scale with $J^2/\dot{m}$, including the time taken to achieve symmetry, the overall intensity of 488 nm light, the appearance of the barrel, and the relative intensity of the bright phase. The significance of the $J^2/\dot{m}$ parameter can be understood by briefly examining the theoretical electromagnetic thrust.

Fr.	Time (μs)		Fr.	Time (μs)		Fr.	Time (μs)
1	20		11	460		21	900
2	60		12	510		22	950
3	110		13	550		23	990
4	150		14	590		24	1030
5	200		15	640		25	1080
6	240		16	680		26	1120
7	280		17	730		27	1170
8	330		18	770			
9	370		19	810			
10	420		20	860			
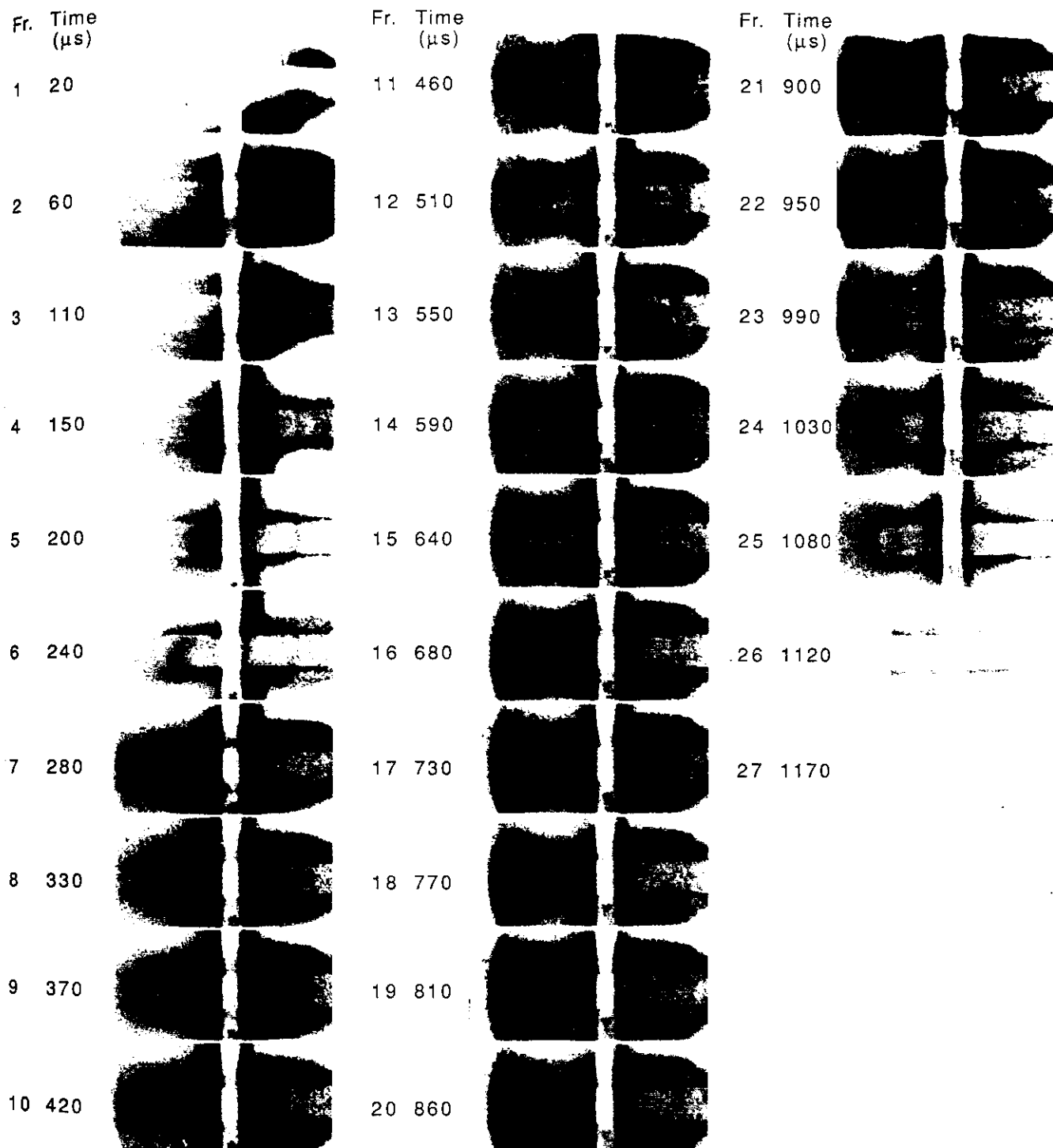
CI_33817

Uncertainty in Absolute Times = ± 20 μs
Period Between Frames = 44.1 μs ± .1 μs

J = 16.4 kA,   ṁ = 5.9 g/s,   488 nm Light,   Side
Figure   3-11

Since the magnetic field is generated solely by the currents in the thruster, it is proportional to the total thruster current, J, and electromagnetic thrust is generated by the $\mathbf{j} \times \mathbf{B}$ Lorentz force. The integral of this cross product over the volume of the thruster gives the total thrust, which can be written:

$$T = bJ^2,$$

where one factor of J comes from the current field itself, and the other comes from the magnetic field. b is a geometric constant. From the definition of specific impulse, the ratio of thrust to propellant mass flow, it is apparent that $J^2/\dot{m}$ is proportional to the specific impulse. A more profound relationship between $J^2/\dot{m}$ and the asymmetric behavior will be discussed in Chapter 5.

To investigate the dependence of the discharge behavior on $J^2/\dot{m}$, photographic sequences were obtained at several currents at mass flows of 3.3, 5.9 and 15.5 g/s. Figures 3-12 and 3-13 illustrate the similarity of the discharge at similar values of $J^2/\dot{m}$. In Figure 3-12, the first ten frames of sequences at roughly 8, 12, and 16 kA, all at 5.9 g/s, are shown. Figure 3-13 shows the first ten frames of sequences at approximately 12 kA and the three different mass flow rates. The low current discharge in Figure 3-12 and the high mass flow discharge in Figure 3-13 both have a $J^2/\dot{m}$ value of about 10 kA^{2}s/g. The high current and low mass flow discharges both have $J^2/\dot{m}$ values of about 43 kA^{2}s/g. The 12 kA, 5.9 g/s discharge falls in between with a $J^2/\dot{m}$ value of about 24 kA^{2}s/g.

The time until a discharge luminosity pattern becomes essentially symmetric is an important parameter since it determines, in part, how significant the effect of asymmetric behavior is on pulsed discharges. For the adverse effects of asymmetric behavior to be negligible, the asymmetric transient time must be short compared to the pulse time. The transient time can be estimated visually from the photographic sequences to within one framing period, which is typically 40-50 µs. For the three sequences on Figure 3-12, the transient times are 400, 300, and 260 µs, respectively. For the sequences in Figure 3-13, the times are 270, 300, and 430 µs. There is an unmistakable trend toward longer times for lower currents and higher mass flows. In addition, the

Fr.	Time (µs)		Fr.	Time (µs)		Fr.	Time (µs)	
1	43		1	30		1	30	
2	93		2	80		2	80	
3	143		3	130		3	130	
4	194		4	180		4	170	
5	244		5	230		5	220	
6	294		6	280		6	270	
7	344		7	320		7	320	
8	394		8	370		8	370	
9	445		9	420		9	410	
10	494		10	470		10	460	

CI_34467-9	CI_33769	CI_33731
Abs. Uncert. = ± 2 µs	Abs. Uncert. = ± 25 µs	Abs. Uncert. = ± 25 µs
Fr. Period = 50.2 ± .1 µs	Fr. Period = 49.0 µs ± .2 µs	Fr. Period = 48.1 µs ± .2 µs
J = 7.74 kA	**J = 11.8 kA**	**J = 15.7 kA**

$\dot{m}$ = 5.9 g/s,   488 nm Light

Figure 3-12

Fr.	Time (μs)		Fr.	Time (μs)		Fr.	Time (μs)	
1	10		1	30		1	30	
2	60		2	80		2	70	
3	100		3	130		3	120	
4	150		4	180		4	160	
5	190		5	230		5	200	
6	240		6	280		6	240	
7	280		7	320		7	290	
8	330		8	370		8	330	
9	370		9	420		9	370	
10	420		10	470		10	410	
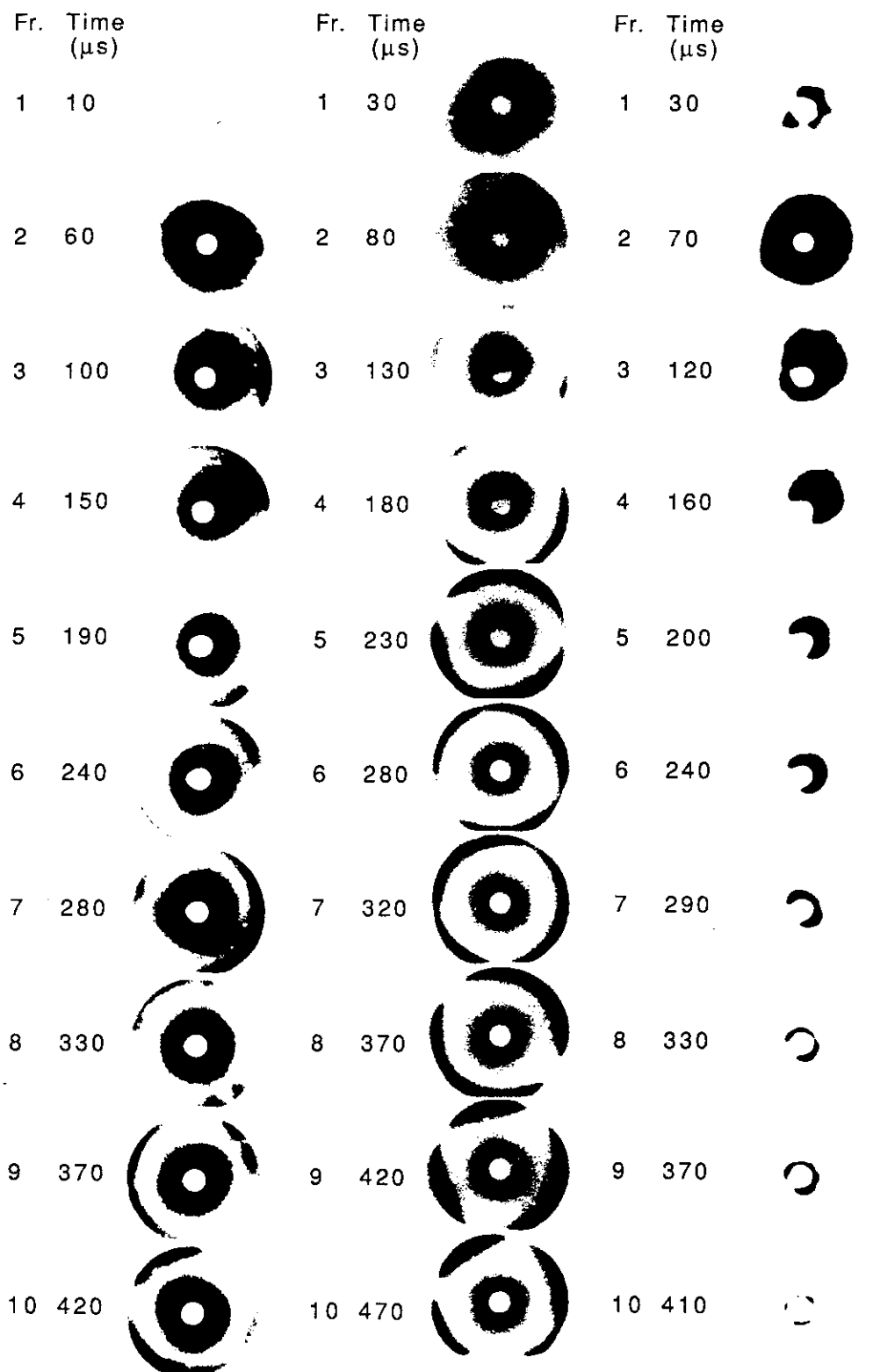
CI_344801	CI_33769	CI_33802
Abs. Uncert. = ± 25 μs	Abs. Uncert. = ± 25 μs	Abs. Uncert. = ± 20 μs
Fr. Period = 45.6 ± .2 μs	Fr. Period = 49.0 μs ± .2 μs	Fr. Period = 42.6 μs ± .2 μs
$\dot{m}$ = 3.3 g/s	$\dot{m}$ = 5.9 g/s	$\dot{m}$ = 15.5 g/s

$J \approx 12$ kA, 488 nm Light

Figure 3-13

sequences with similar values of $J^2/\dot{m}$ have nearly identical transient times.

The transient times for all end view sequences are plotted versus $J^2/\dot{m}$ on Figure 3-14. Data from all three mass flow rates are well mixed, indicating that $J^2/\dot{m}$ is a reasonable scaling parameter. To verify that the transient time is not merely a function of current, the data are plotted against current in Figure 3-15, which shows a distinct separation of data from different mass flow rates. Specific impulse requirements will probably dictate operation at values of $J^2/\dot{m}$ above 40 kA^{2}s/g. The transient time for this value of $J^2/\dot{m}$ is about 250 μs, a quarter of the total pulse time. This value of $J^2/\dot{m}$ is also at the transition in time-integrated photographs, above which they appear very symmetric. Since there is no discontinuity or asymptotic behavior in the transient times at this value of $J^2/\dot{m}$, the appearance of the time-integrated photographs must be affected by factors other than the duration of asymmetric behavior, as will be demonstrated later. At the lowest values of $J^2/\dot{m}$, the transient times can reach a half a millisecond or more, 50% of the total pulse time.

The overall intensity of 488 nm light also scales with $J^2/\dot{m}$. The discharge tends to be brighter with higher currents and lower mass flows, and discharges with similar values of $J^2/\dot{m}$ get the same exposure with the same aperture settings. This observation agrees qualitatively with the predictions of critical ionization velocity (CIV) theory that the level of ionization is an increasing function of $J^2/\dot{m}$ until a full ionization condition is reached.[22] Simpson[23] measured the radiance of four argon ion lines at a point on the axis 3 cm downstream from the cathode tip and found that the number densities of the ion excited states increased with current and leveled off above 23 kA current at 6 g/s. Figure 3-16 shows the steady state output of the photomultiplier (PM) tube mounted on the movie camera for several values of current at a mass flow of 5.9 g/s. The PM tube was mounted as described in chapter 2 for determining the film speed, except that the camera was off and the shutter held open and stationary. The fact that the intensity does not level off until currents above those predicted by CIV theory and Simpson's data is not surprising since these measurements integrate the intensity from the entire plume as viewed from the end of the tank.

A phenomenon that appears only for $J^2/\dot{m}$ values between 15 and 50 kA^{2}s/g is the irregular

Transient Time vs. J^2/Mass Flow

Times estimated from photgraphic sequences
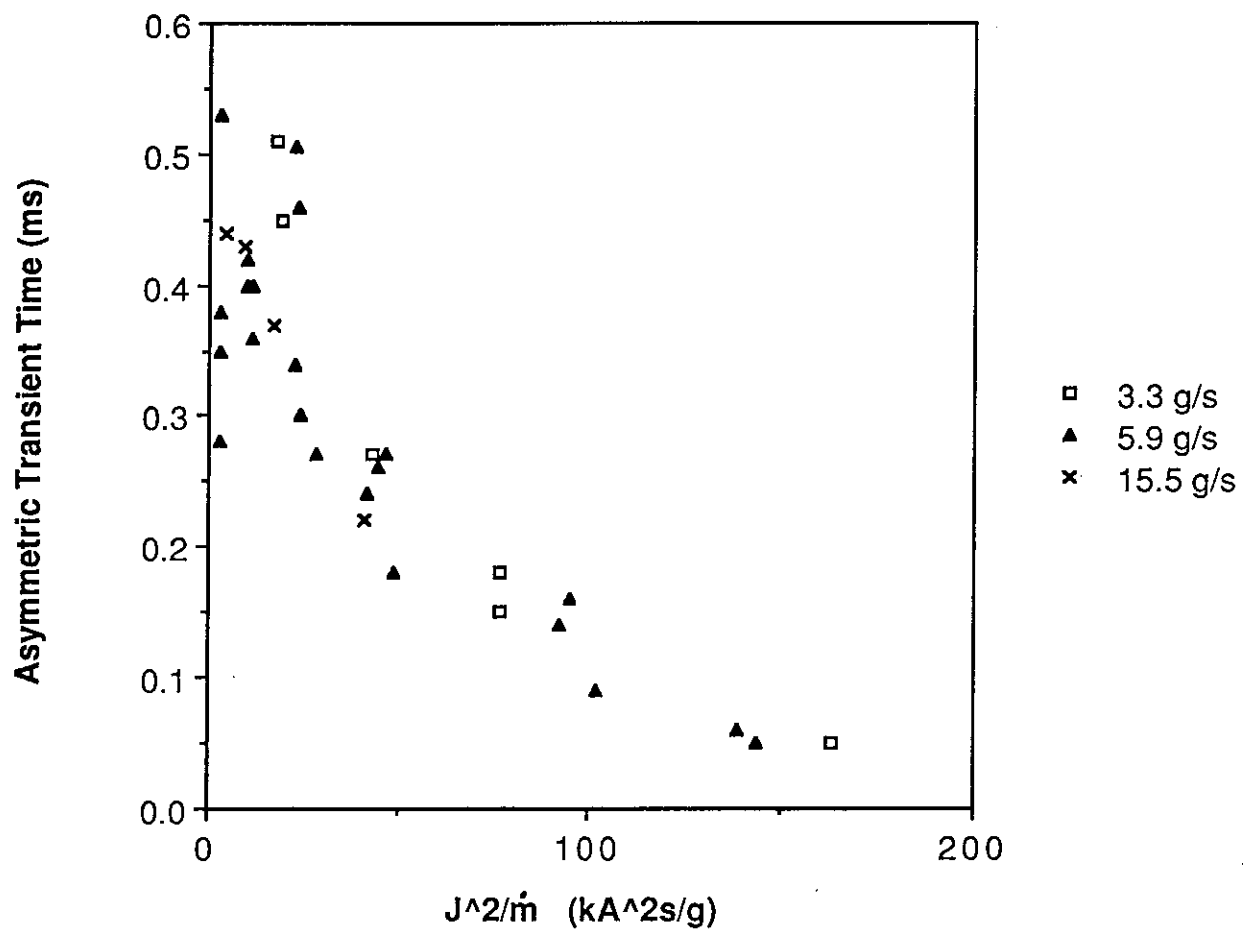
Figure 3-14

Transient Time vs. Current

Times estimated from photgraphic sequences
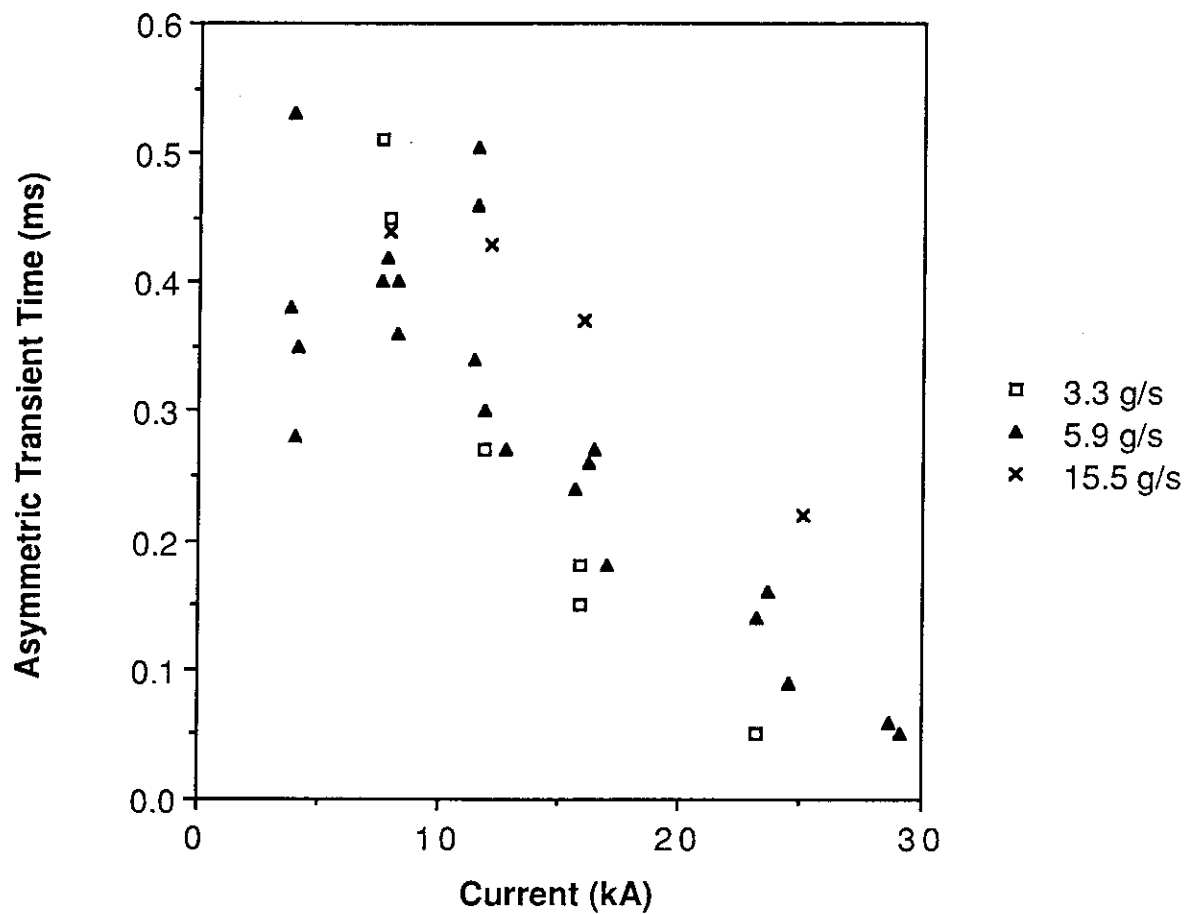
Figure 3-15

Steady State 488 nm Intensity vs. Current
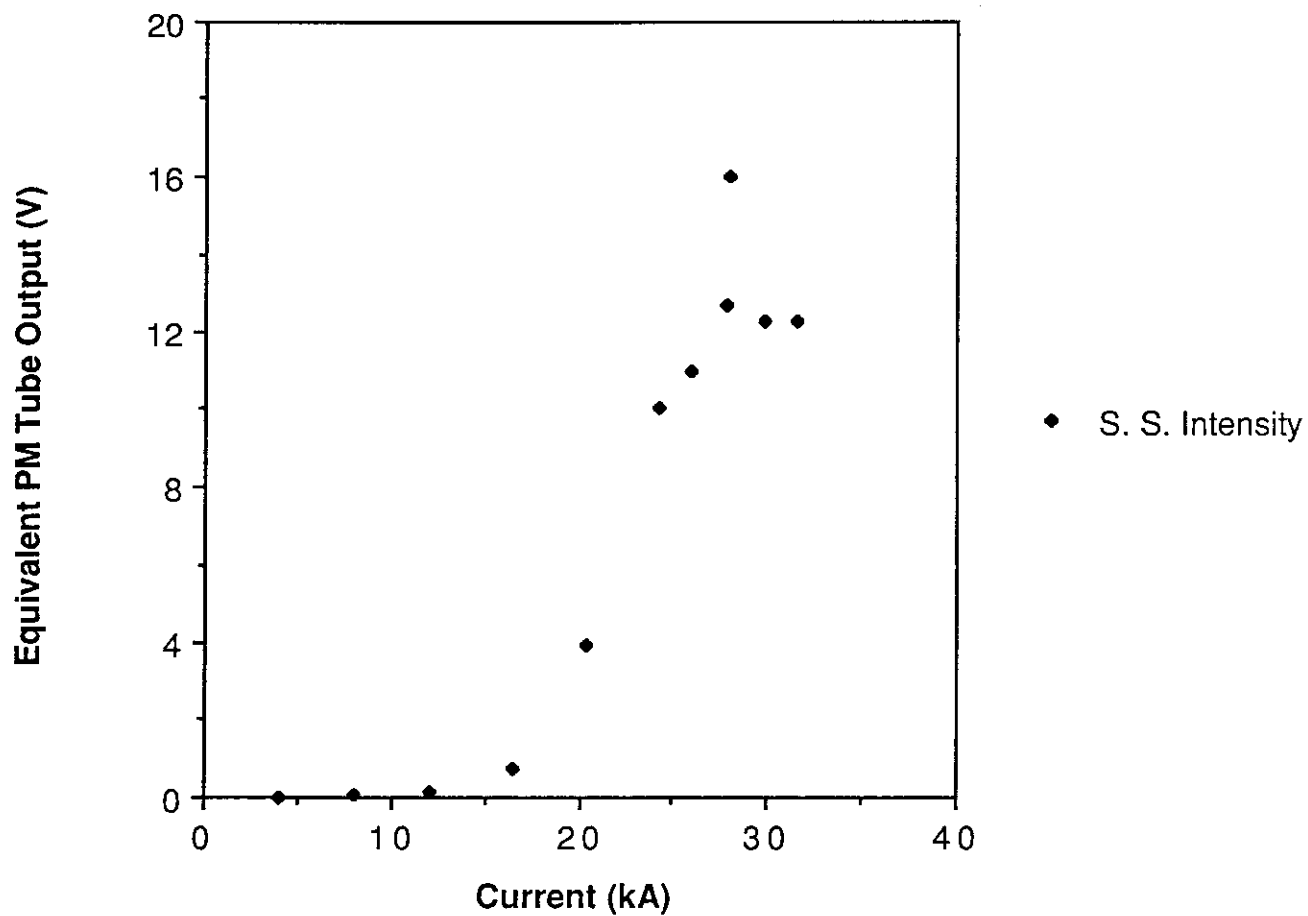
Figure 3-16

luminosity adjacent to the inner edge of the anode, visible in the last two sequences of Figure 3-12 and the first two sequences of Figure 3-13, as well as Figure 3-7. The luminosity appears within 200μs of the beginning of the discharge and remains unsteady throughout the pulse. The side view photographs of Figure 3-3 indicate that the luminosity is located on the upstream inner edge of the anode, and that it may disappear at higher values of $J^2/\dot{m}$ because it fades against the intensity of the main discharge. Measurements with magnetic field probes have not shown any discernible correlation between the position of the luminous regions and fluctuations in the magnetic field nearby.

At high values of $J^2/\dot{m}$, a bright ring around the cathode, known as "the barrel", appears (Figure 3-8). Although Rudolph[21] associated this phenomenon with "onset" conditions beginning at about 90 kA^{2}s/g, it appears to be just an advanced stage of the well-defined disk of luminosity around the cathode that develops at about 40 kA^{2}s/g. In fact, when the camera aperture is small enough, this well-defined disk will resolve into a barrel. Since 40 kA^{2}s/g is the condition at which CIV theory predicts full ionization[22], the barrel phenomenon and the development of a well-defined outer edge of the cathode luminosity may be linked to a full ionization condition.

3.5 The Initial Bright Phase and the Effect of Cathode Spots

One striking feature of all sequences, except those at the highest values of $J^2/\dot{m}$, is the brief period of high intensity early in the discharge. At low $J^2/\dot{m}$, the discharge rapidly increases in intensity and radial extent to a peak, usually during the first two frames, after which the intensity and radial extent diminish to an asymptotic level for the rest of the pulse (Figure 3-6). At moderate values of $J^2/\dot{m}$ ($\approx$40 kA^{2}s/g), the discharge diminishes for a few frames after the bright phase and then expands again to its steady state level (Figure 3-7). At the highest values of $J^2/\dot{m}$, the bright phase is lost in the rapidly intensifying steady state portion of the discharge. Side view sequences (figures 3-10 and 3-11) show that at all currents, the discharge grows to a maximum axial extent beyond the cathode tip during the first two frames, then retracts temporarily, and gradually grows

out again to its steady state configuration.

To investigate this phenomenon further, the PM tube was mounted on the movie camera in the end view position as described in the previous section, and traces of the overall 488 nm intensity as a function of time were collected for several currents at 5.9 g/s. Figures 3-17 shows the PM tube output for 4 kA, 16 kA, and 24 kA discharges. The bright peak near the beginning of the 4 kA discharge dominates the steady state intensity. Since the bright phase occurs during the asymmetric transient, the asymmetric behavior is disproportionately represented in time-integrated photographs. At 16 kA, the initial peak is still in evidence, but it has been surpassed by the steady state intensity, during which the discharge is symmetric. In fact, a plot of the ratio of steady state to initial peak intensity versus current (Figure 3-18) shows that the steady state intensity surpasses the peak intensity at about 16 kA for this mass flow. This observation explains why time-integrated photographs undergo a transition to a symmetric appearance at 16 kA. At higher currents, the initial peak appears only as a small plateau in the rapidly rising intensity, but is still discernible as a regular feature of the intensity profile.

For all currents, there is no appreciable 488 nm line intensity for the first 10-20 μs after breakdown (Figure 3-19). Once the transition from glow discharge to arc occurs at breakdown, the terminal voltage drops precipitously within a fraction of a microsecond. Within the first 10-20 μs, the voltage has dropped to close to its steady state operating value and the current has risen to several hundred or thousand amperes. A simple calculation of the electron diffusion velocity resulting from the initially high electric fields (neglecting the effects of magnetic fields and pressure gradients in the first few microseconds) shows that the resident time of the electrons accelerated by high initial electric fields is a fraction of a microsecond.[24] Since the Einstein coefficient for the 488 nm transition is on the order of 10^8 s^{-1}, the excited ionic state emits the 488 nm light in a time following excitation that is very short compared to the time scale for which all measurements were made.[25] Therefore, it seems unlikely that the electrons accelerated by the initial high voltages play a significant role in the creation of the transient bright peak.
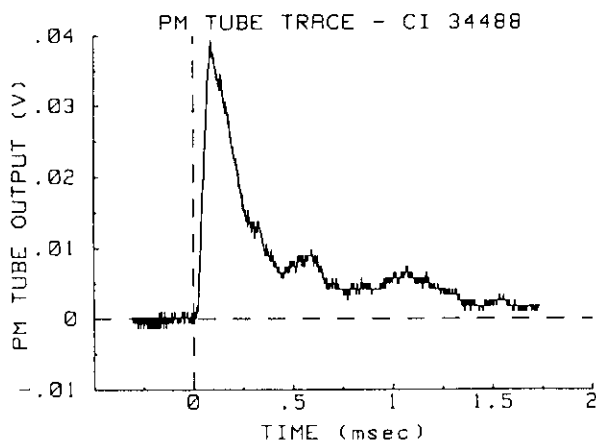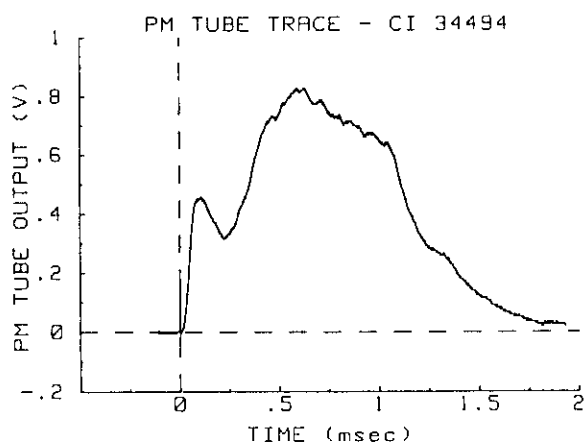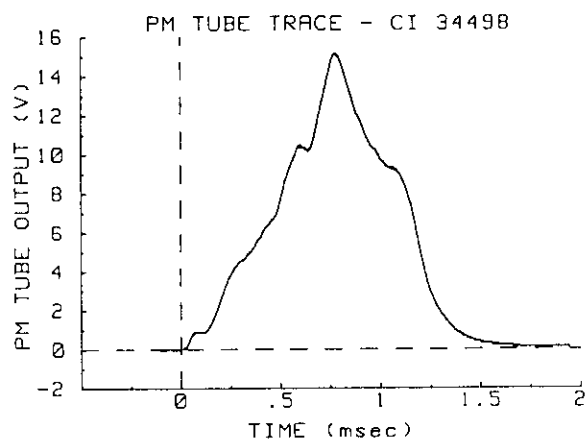
Photomultiplier Output
$\dot{m}$ = 5.9 g/s, End View, 488 nm light
Figure 3-17

Ratio of S.S. to Initial Peak Intensity vs. Current

Figure 3-18

VOLTAGE TRACE - CI 34489

Voltage

CURRENT TRACE - CI 34488

Current

PM TUBE TRACE - CI 34488
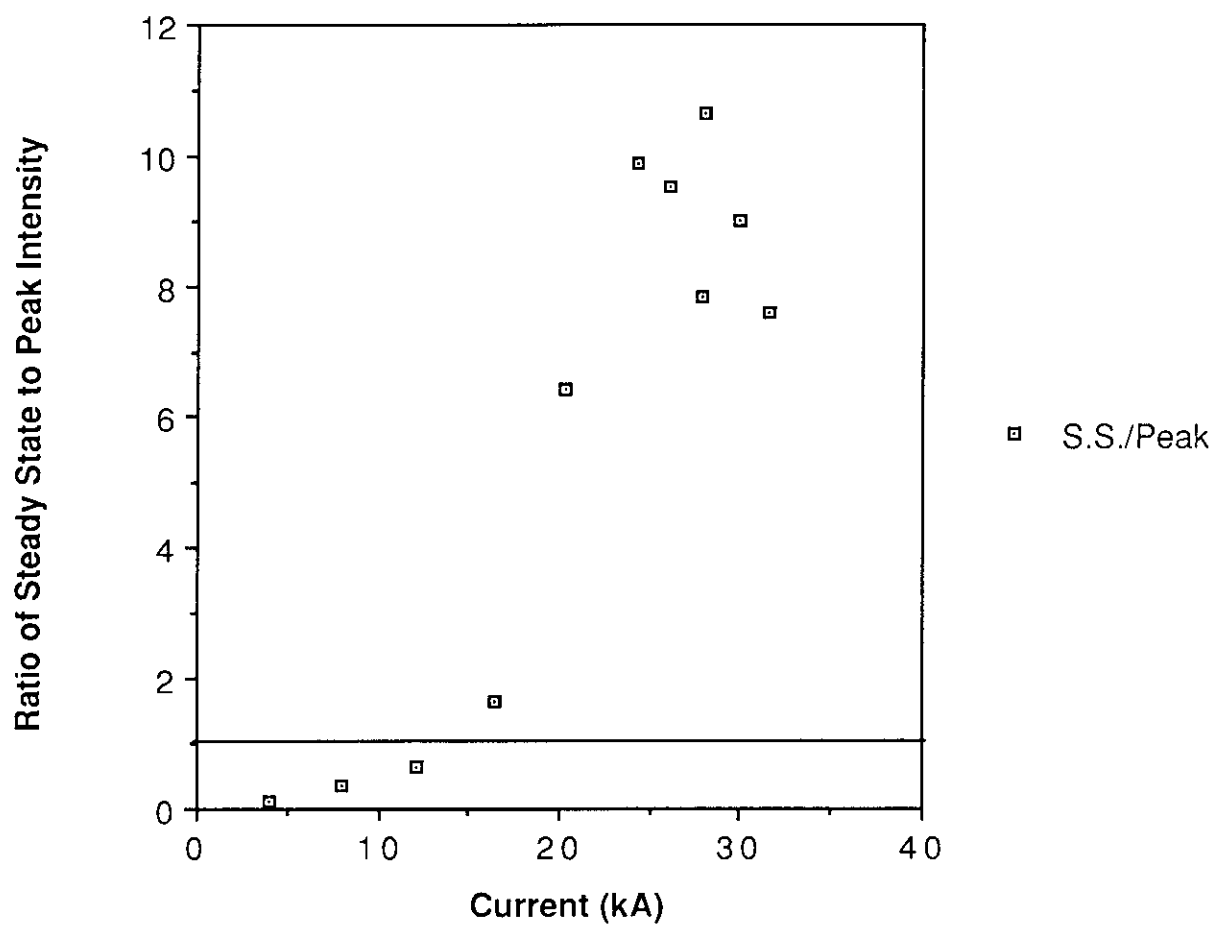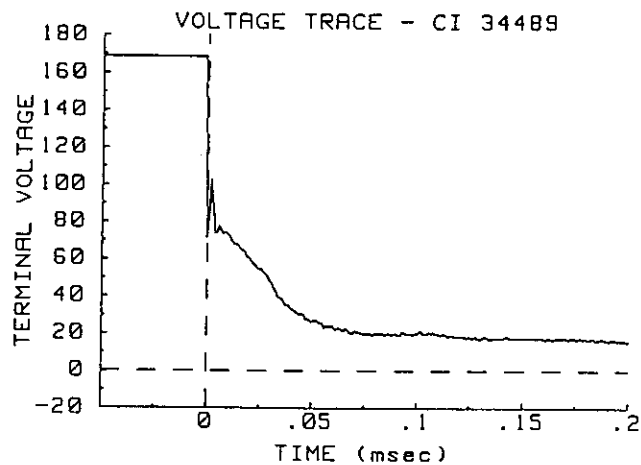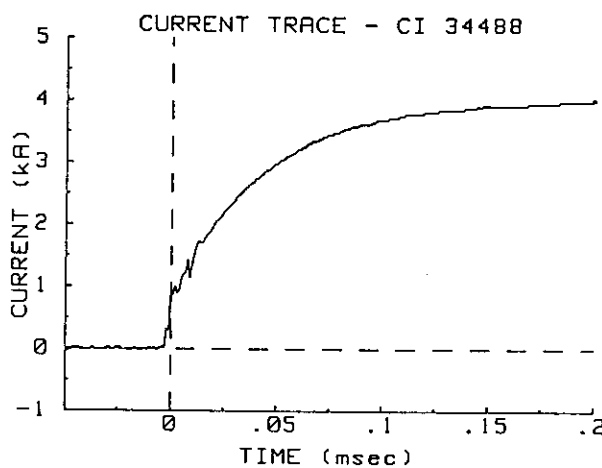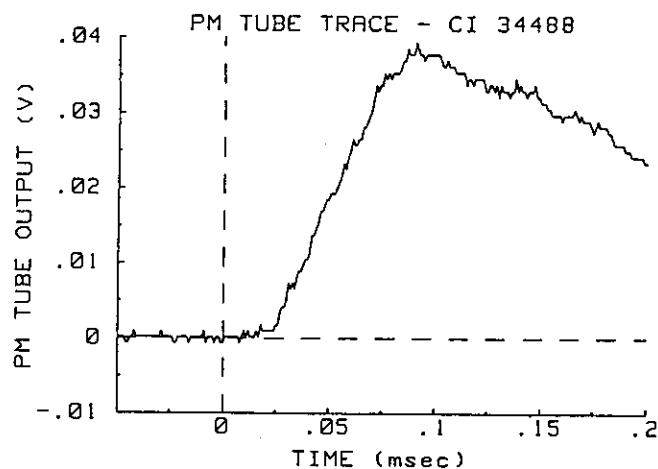
PM Tube Output

Detail of Voltage, Current, and PM Tube Data
at Beginning of Discharge: J = 4.0 kA, $\dot{m}$ = 5.9 g/s
Figure 3-19

In all cases, the peak (or the plateau) in intensity occurs approximately 100 μs after breakdown, independent of current or intensity. The rise time of the current, set by the pulse-forming network configuration, is also about 100 μs independent of current. When the configuration was altered to give a rise time of 45-55 μs, the peak intensity occurs between 50 and 80 μs after breakdown. Therefore, the mechanism responsible for the bright phase is tied to the time derivative of the current. As the current begins to rise rapidly during the transition from glow discharge to arc, the large time derivatives of the self-induced magnetic field generate electric fields opposing the applied electric field according to Faraday's Law[1]:

$$\nabla \times E = -\partial B / \partial t.$$

The net effect is to discourage conduction in the downstream portion of the thruster and thus concentrate most of the current at the base of the cathode, as was noted previously. Magnetic field probe measurements at several axial positions near the cathode surface show very little current emanating from the cathode downstream of 3 cm from the backplate for the first 100-150 μs. Probe measurements downstream of the anode at larger radii occasionally show a small peak at 100 μs, but downstream current conduction is generally negligible until the total thruster current reaches its steady state value.

Although the current is temporarily constrained to flow near the back of the thruster, luminosity patterns show evidence of ionization throughout the thruster chamber and downstream of the anode face at least as far as the cathode tip. Such widespread evidence of ionized flows indicates that hot plasma from that region impinges on the slow-moving cold flow downstream and loses energy to ionization. As the total current reaches its steady state value, the time derivatives disappear, and the current pattern is free to convect downstream. As the flow accelerates, the densities drop, leading to the observed decrease in 488 nm intensity.

After the bright phase, all side view sequences show that the discharge eventually expands again downstream after a period of diminished axial extent. The times taken to establish the steady state configuration in the axial direction range from 700 μs at 4 kA to 150 μs at 24 kA, which are

comparable to the asymmetric transient times measured from an end view. Probe measurements of the time until the steady state magnetic field is established downstream of the anode agree with these visual observations. In contrast, Barnett[16] measured transient times in the axial establishment of the magnetic field pattern in the same region that tended to increase with current. However, Barnett was measuring transients induced by a change in thruster current in an established discharge.

Since the axial behavior observed in this study is associated with the initial transient, it gives a possible clue to the mechanisms controlling the establishment of a steady state, axisymmetric discharge. Careful examination of the unfiltered 4 kA sequence in Figure 3-10 reveals the presence of luminous spots on the cathode. First appearing in frame 5 (230 μs), these spots are confined to a region close to the base of the cathode until frame 14 (640 μs), when new spots begin to appear in clusters further downstream. The clusters spread and move back upstream at approximately .5 cm per frame, or 100 m/s, until they uniformly cover the cathode at 780 μs. The axial expansion and stabilization of the discharge roughly corresponds with the appearance and spread of the spots until they uniformly cover the cathode.

Cathode spots are small regions of very high current density that form on cold cathodes with a high work function because the cold cathode is unable to sustain the required electron current purely through field emission. The current is therefore concentrated into small filaments that resistively heat spots on the cathode to allow thermionic emission. It is a well-known, but little-understood phenomenon that spots are unstable, constantly moving to new sites, and, in a low pressure environment, they will tend to move in the direction opposite the $j \times B$ force, i.e. upstream, as was also observed here.[26] In addition, this "retrograde" motion has the effect of spreading out clusters of spots since they will also move opposite the local $j \times B$ direction.[27] The tendency to move in the retrograde direction provides a possible explanation as to why the spots take so long to begin spreading over the cathode, since they start at the base of the cathode and will not tend to move downstream.

At 8 kA and 5.9 g/s, cathode spots can be faintly seen to cover the cathode after about 400

μs, the same time needed for axial stabilization to take place and comparable to that observed for the establishment of azimuthal symmetry in end view sequences obtained at the same conditions. Spots cannot be seen at higher currents because the plasma radiation washes out the light emitted from the spots. Although the overall intensity of the plasma radiation increases rapidly with current, the current in a single spot is limited, and more spots are formed as the total current rises.[27] Therefore, the temperature of each spot also tends to remain constant regardless of total thruster current, and it stands to reason that the intensity of light emitted from the molten spot also remains constant with increasing current.

Summary

Photographic sequences reveal asymmetric behavior at all conditions except at the very highest currents studied. However, this behavior is always associated with the initiation of the pulse and is transient in nature. At values of $J^2/\dot{m}$ of 10 kA^2s/g and below, unsteady and non-uniform behavior, distinct from the overall asymmetry of the initial transient, appears throughout unfiltered sequences. During the asymmetric transient, the region of highest intensity remains stationary while the emitting plasma diffuses around the cathode to establish a symmetric distribution. Once a symmetric pattern has been established, asymmetric behavior does not recur, nor is there any evidence of rotating or oscillating spokes. Finally, unfiltered side view sequences reveal that appearance and spread of cathode spots coincides with the establishment of a symmetric luminosity pattern.

Chapter 4

MAGNETIC FIELD PROBE STUDIES

4.1 Interpretation of Magnetic Field Data

An essential prerequisite for understanding the observed asymmetric luminosity patterns is knowledge of the three dimensional and temporal behavior of the associated current patterns. Because the presence of a current probe would disturb the local current distribution and the angular orientation of the asymmetric discharge often changes from shot to shot, it is not possible to make direct measurements of the local current density to generate a three dimensional map of the current distribution. However, magnetic field measurements can indirectly yield information about the current distribution since fields in a self-field thruster arise solely from the current distribution in the discharge and electrodes. The magnetic field at a position, $\mathbf{r}$, can be calculated using the Biot-Savart Law:[1]

$$\mathbf{B(r)} \ = \ (\mu_0/4\pi) \int \mathbf{j(r')} \ X \ \mathbf{(r-r')} \ dV'/|\mathbf{r-r'}|^3,$$

where μ_0 is the permeability of free space, $\mathbf{j(r')}$ is the current density, dV' is a volume element, and $\mathbf{r'}$ is the position vector of a differential current element, $\mathbf{j(r')}dV'$. Because of the integrated nature of the contribution of current elements to the magnetic field at a given point, measurements of the field can yield, in a single discharge, information about the collective behavior of the current pattern. This overall view of the current pattern is precisely what is desired in the study of bulk asymmetric behavior. Moreover, magnetic field probe data are more easily quantified than luminosity data and have much higher temporal resolution than the 20-30 μs framing periods of the photographic sequences provide. For these reasons, four probes were constructed and mounted axisymmetrically as described in Chapter 2 and Appendix C.

For an axisymmetric discharge, in which there is no azimuthal component of the current density, it can be shown that the only component of the magnetic field is in the azimuthal direction. From $\nabla \cdot \mathbf{B} = 0$, all magnetic field lines must close on themselves. In the absence of an azimuthal

component of current density, it is not possible for the field lines to have constant, non-zero axial or radial components and still return to their original location after one cycle in the azimuthal direction. In an asymmetric discharge, both axial and radial magnetic field components may be present, but if the asymmetry is relatively small, the main component will still be azimuthal. Therefore, the probe coil axes were oriented azimuthally for all tests.

Assuming that the time derivative of the electric displacement is negligible, Ampere's Law, a useful form of the Biot-Savart Law, applies:

$$\oint \mathbf{B} \cdot \mathbf{dl} = \mu_0 J_{enc},$$

where the integral is along a closed contour and J_{enc} is the current enclosed by that contour. The assumption of symmetry and the use of a circular contour centered on the axis yields the familiar relation:

$$B_\theta = \mu_0 J_{enc}/2\pi r,$$

where r is the distance to the axis of symmetry. This relation provides a simple approximation for the magnetic field in nearly symmetric discharges.

For most tests, the probes were placed inside the thruster at an axial position 2 cm downstream of the backplate. For all tests, the radial position of the probes was 4.5 cm, the largest radius at which the probes can fit inside the anode orifice. This location has several advantages for observing the asymmetric behavior of the discharge. Previous maps of steady state current contours have shown this to be a region of low current densities upstream of almost the entire current.[16,21] To reduce the differences in the measured field caused by small differences in the axial and radial position of the probes, it is desirable to place the probes in a region of small field gradients. Using the differential form of Ampere's Law and the approximation for a nearly symmetric discharge just described, the radial gradient of the magnetic field is:

$$\partial B/\partial r \approx \mu_0 j_z(r) - \mu_0 J_{enc}(r)/2\pi r^2,$$

where $J_{enc}(r)$ is the enclosed current and $j_z(r)$ is the axial current density at radius r. The axial gradient of the field is:

$$\partial B/\partial z \approx \mu_0 j_r(z),$$

where j_r is the radial current density. A small local current density and large radial position ensure small gradients.

Placing the probes upstream of most of the discharge has the further advantage of allowing an unambiguous interpretation of asymmetric probe measurements. In the symmetric case, the magnetic field is, of course, equal in magnitude and azimuthal direction on opposite sides of the thruster (Figure 4-1, top). In addition, Ampere's Law predicts no field downstream of the discharge essentially because the contributions to the field there from differential current elements throughout the discharge will tend to cancel out. In the asymmetric case (Figure 4-1, bottom), some of the current elements have shifted from one side of the thruster to the other. This situation results in higher fields upstream of the side with highest current densities because there are more current elements nearby to contribute to the field. However, as one moves downstream through the discharge, the field on the side with higher current density actually becomes _less_ than the field on the opposite side and may, in fact, reverse direction. This situation occurs because the increased current density at the top of the figure produces contributions to the nearby downstream field that are out of the page and are not canceled by the weaker current densities on the opposite side of the thruster. At axial positions between these extremes, the relationship between higher fields and higher current densities is ambiguous.

The most important consideration in the placement of the probes is to position them where they are most sensitive to overall asymmetric behavior of the thruster and least sensitive to local fluctuations in the magnetic field. Certain regions of the thruster chamber exhibit oscillations with an amplitude that are a significant fraction of the average field. Since the major components of these oscillations are not correlated between probes, they are not associated with shifts in the bulk of the plasma and are not of primary interest in this study. The larger the amplitude of these local oscillations, the more they will obscure the overall asymmetric behavior of interest. At the top of Figure 4-2, a plot of the normalized amplitude of these oscillations is given as a function of axial

ANODE

B
⊗ ⊗
⊗ ⊗
⊗ ⊗ ⊗ ⊗

CATHODE ⟵——— j

⊙ ⊙ ⊙ ⊙
⊙ ⊙
⊙

no magnetic field
downstream of the discharge

Symmetric Discharge

all magnetic fields in same
azimuthal direction

Direction of magnetic field: ⊙= out of page   ⊗ = into page

ANODE

B
⊗ ⊗
⊗ ⊗ ⊙
⊗ ⊗ ⊗ ⊙ ⊙
⊗ ⊙

CATHODE ⟵——— j

⊙ ⊙
⊙
⊙

magnetic field downstream
of strong region of discharge
opposite to "normal" direction

Asymmetric Discharge
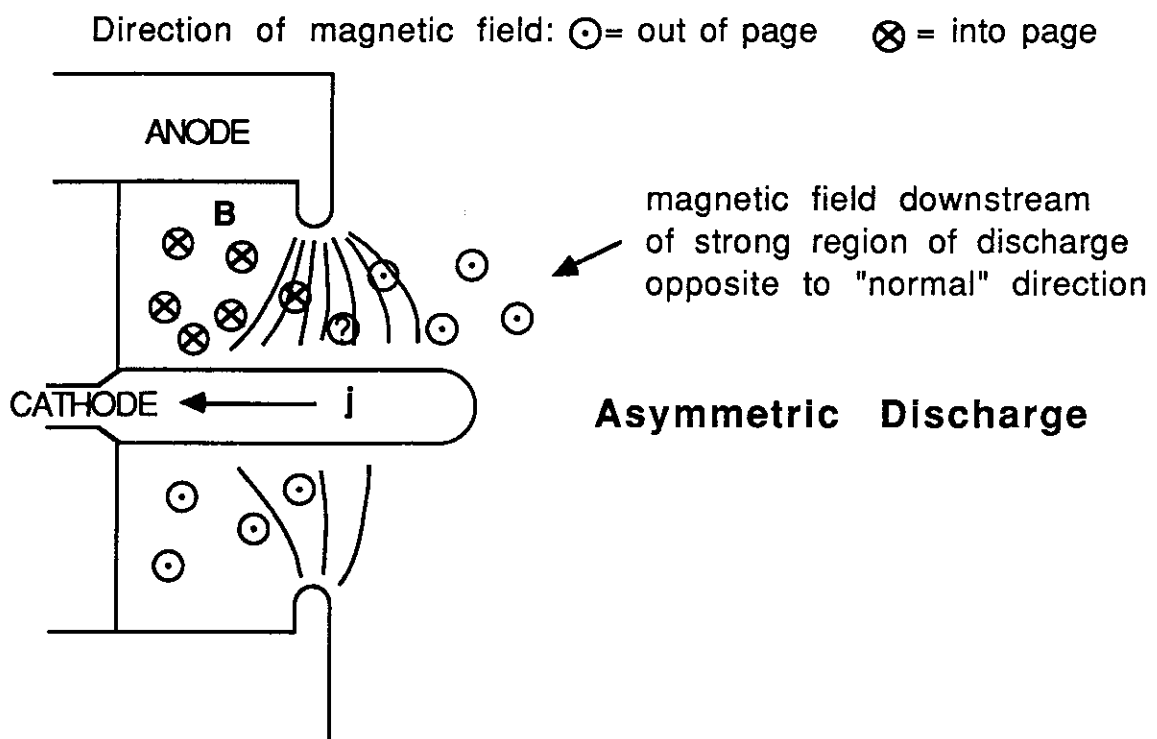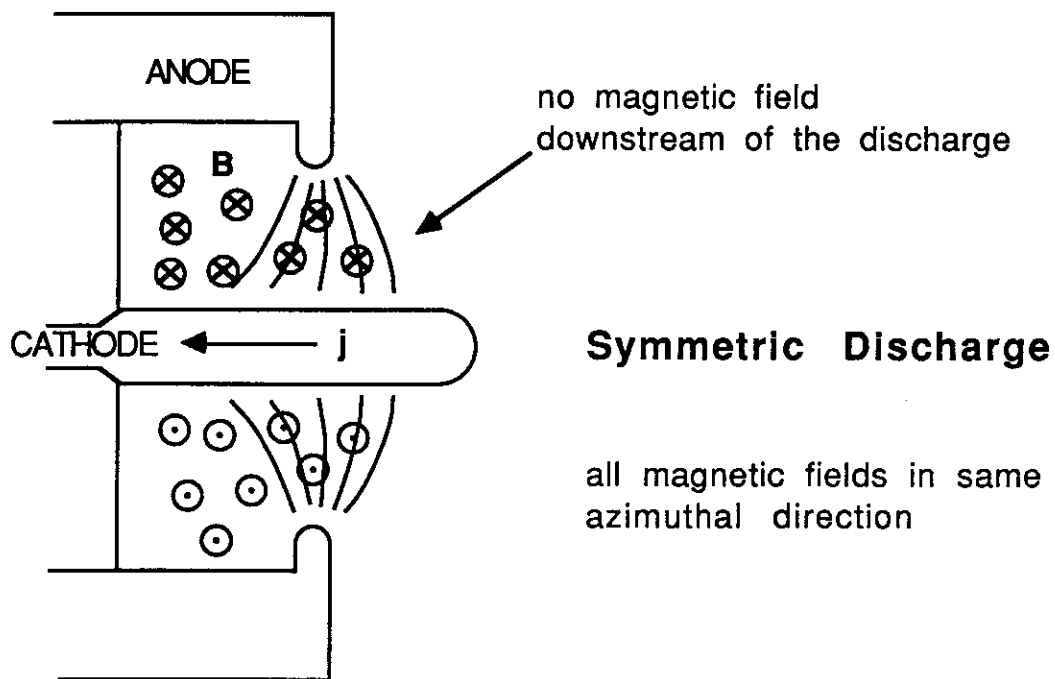
**Comparison of Magnetic Field Configurations
for Symmetric and Asymmetric Discharges
Figure 4-1**

Magnetic Field Oscillations vs. Axial Position

Average peak-to-peak oscillation amplitude divided by average magnetic field
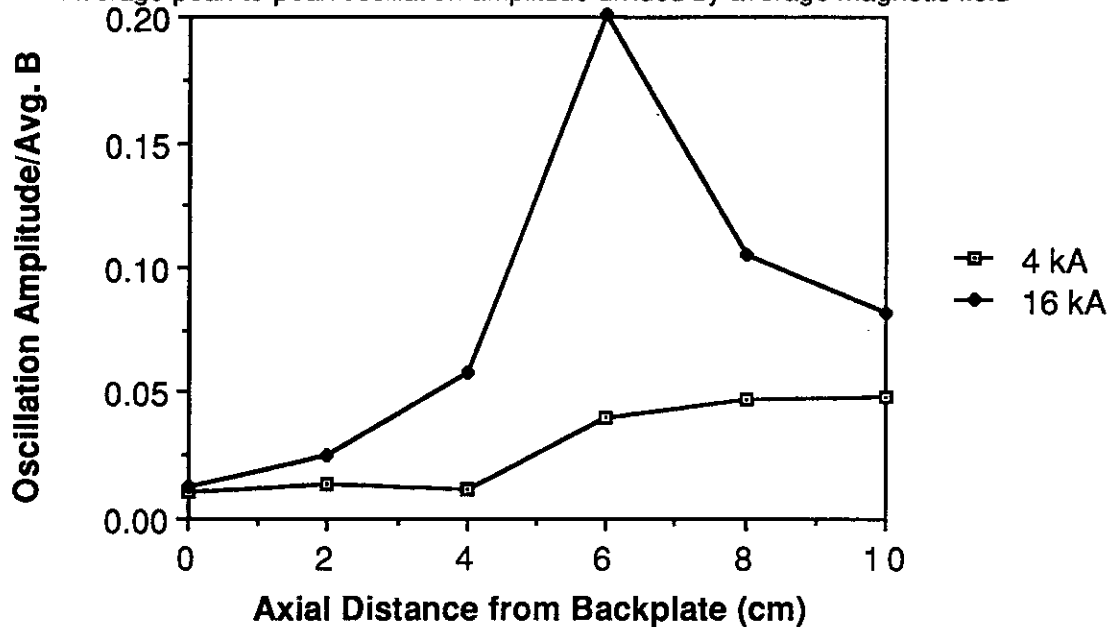
Axial Magnetic Field Gradient vs. Axial Position

Avg gradient in B field divided by avg field between measurement positions

Anode 5-6 cm
from backplate
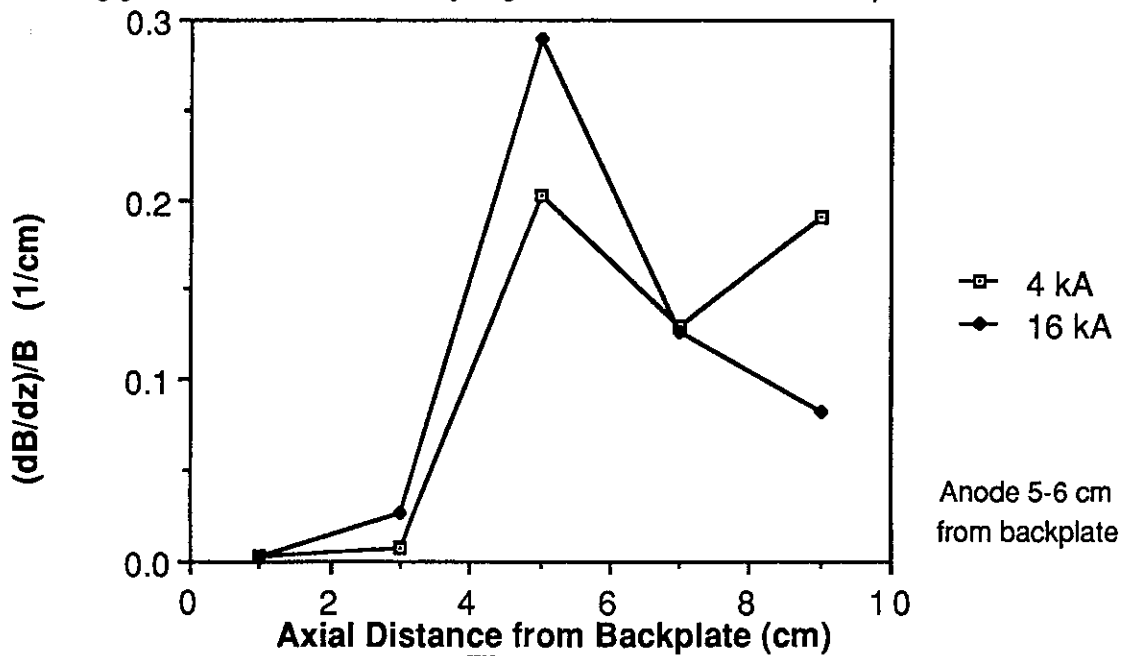
Figure 4-2

position at 4.5 cm radius for two currents. This plot shows that the oscillations are highest near the anode and lowest inside the thruster chamber near the backplate.

These regions have also been observed to be regions of high and low current densities, respectively. From Ampere's Law, the radial current density is proportional to the axial gradient of the magnetic field in a symmetric discharge. At the bottom of Figure 4-2, the plot of this gradient, divided by the average local field as in the plot at the top, demonstrates that regions of high current density coincide with regions of large amplitude oscillations. This observation is consistent with the fact that because the contribution to the magnetic field from a current element falls off as the square of the distance, fluctuations in current density close to the probe yield large amplitude magnetic field oscillations. Therefore, it is best to place the probes out of regions of high current density.

It is also apparent that the local current density is related to the reciprocal of the length scale of the magnetic field:

$$j_r/B_\theta \sim (\partial B_\theta/\partial z)/B_\theta = 1/\lambda_z,$$

where λ_z is the axial length scale of the magnetic field. The length scale of the magnetic field at a given location acts as a measure of the scale of non-uniform behavior that will dominate differences in the field at the different probes. In regions with a short length scale, such as near the anode, small scale non-uniformities have a predominant effect. In regions of moderate length scale, small scale fluctuations average out, and only asymmetric behavior on the scale of the whole thruster becomes important. In regions of long length scales, such as near the backplate, the fields become less sensitive to asymmetric patterns in the plasma and are dominated by the essentially symmetric current distributions in the electrodes. Thus, it is important to place the probes as close as possible to the conducting plasma, but far enough away to limit the effect of local fluctuations. The empirically determined optimum lies 2 cm from the backplate at the 4.5 cm radius.

To permit simultaneous visualization of the data from the four probes, a parameter has been devised analogous to a "current centroid". Consider a current pattern that is cylindrically

symmetric, but shifted off the centerline of the thruster a distance D_{13} along the diagonal axis between probes 1 and 3 (Figure 4-3a). If the probes lie outside the current pattern, the magnetic field measured at probe 1 is given by Ampere's Law as:

$$B_1 = \mu_o J / 2\pi R_1,$$

where R_1 is the distance from the center of this hypothetical current distribution, and J is the total current. The ratio of the fields measured by two opposing probes would then be:

$$B_1 / B_3 = R_3 / R_1 = (D_{13} + R) / (D_{13} - R),$$

where R is the radial distance to the probes from the center of the thruster. Solving for D_{13}/R, the normalized distance from the thruster centerline to the centroid along the 1-3 axis, one obtains:

$$D_{13}/R = (B_1/B_3 - 1) / (B_1/B_3 + 1).$$

Along with a similar parameter obtained for the other two probes, these coordinates define the position of the "current centroid" relative to the thruster centerline. Typical data from the four probes, obtained at this position for a discharge with 4 kA current and 5.9 g/s mass flow, are displayed in Figure 4-3b. The centroid position is plotted for each point in time at the top of Figure 4-3c for the data in Figure 4-3b. In this plot, and all like it that follow, sequential centroid positions are connected by lines to show the centroid's course in time. The radial distance from the center of the thruster to the centroid position is defined as the non-dimensional "asymmetry parameter":

$$A = ((D_{13})^2 + (D_{24})^2)^{1/2}/R$$

and is plotted versus time for this discharge at the bottom of Figure 4-3c.

4.2 Characterization of Asymmetric Behavior

Plots such as the two in Figure 4-3c, made for a wide range of current and mass flow conditions, reveal several consistent features of the current pattern behavior. First, the asymmetric behavior is largely confined to a transient that is always associated with the beginning of the discharge. After a few hundred microseconds of operation, the asymmetry parameter generally drops to a value of less than 0.03. The asymmetry parameter that remains after the transient, which

66
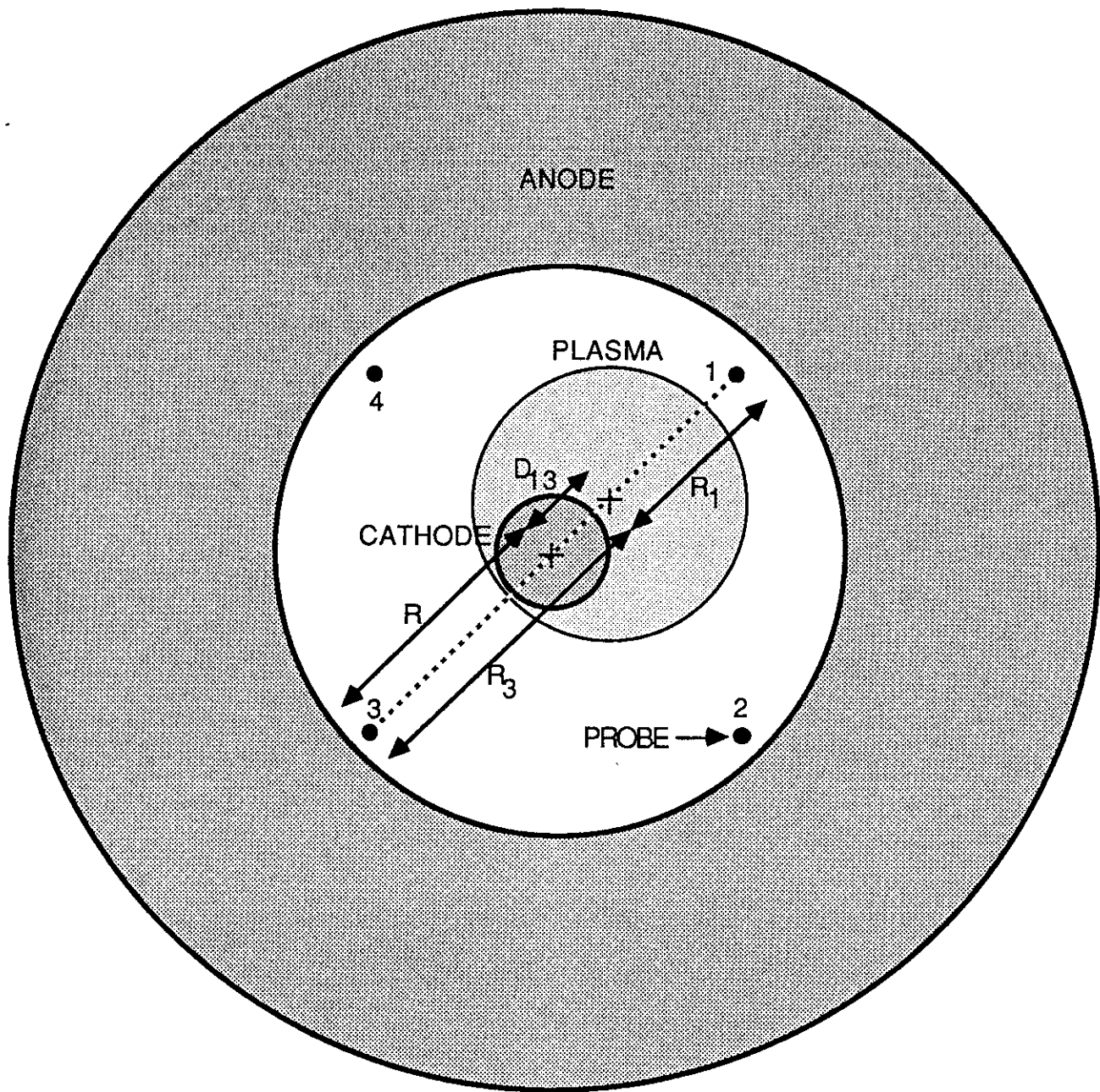
End View

Figure 4-3a
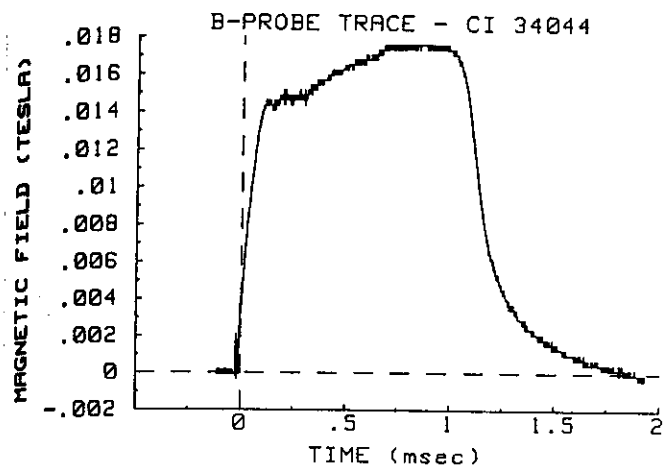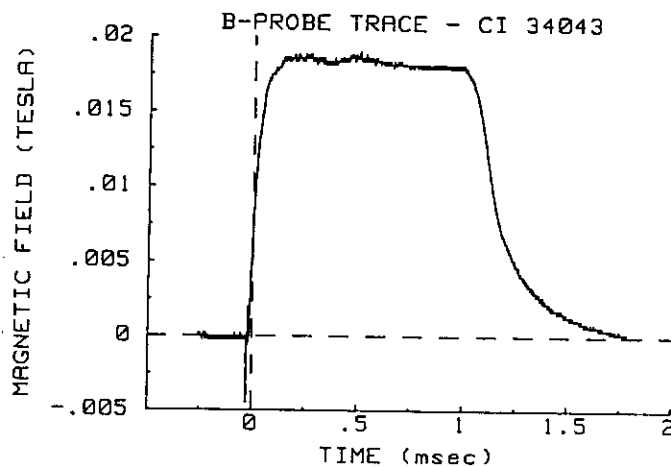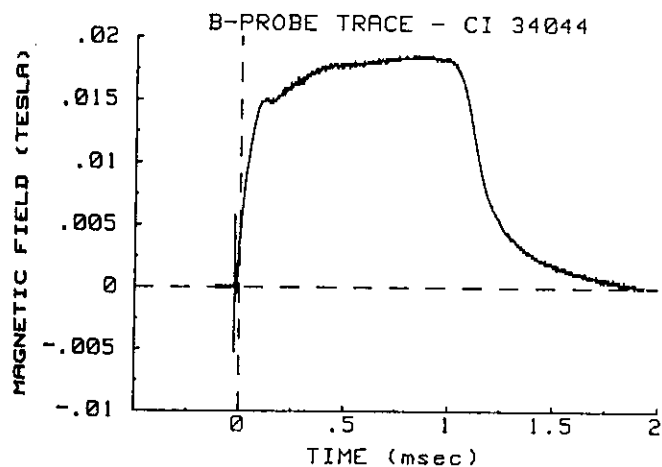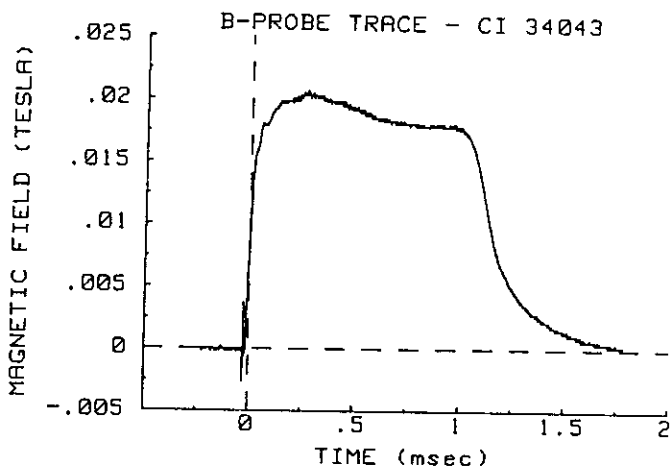
Typical Data from Magnetic Field Probes

J = 4.5 kA, $\dot{m}$ = 5.9 g/s, Probes 2 cm from Backplate

Figure 4-3b

CURRENT CENTROID
FILES 34043 & 34044

ASYMMETRY PARAMETER VS. TIME
FILES 34043 & 34044
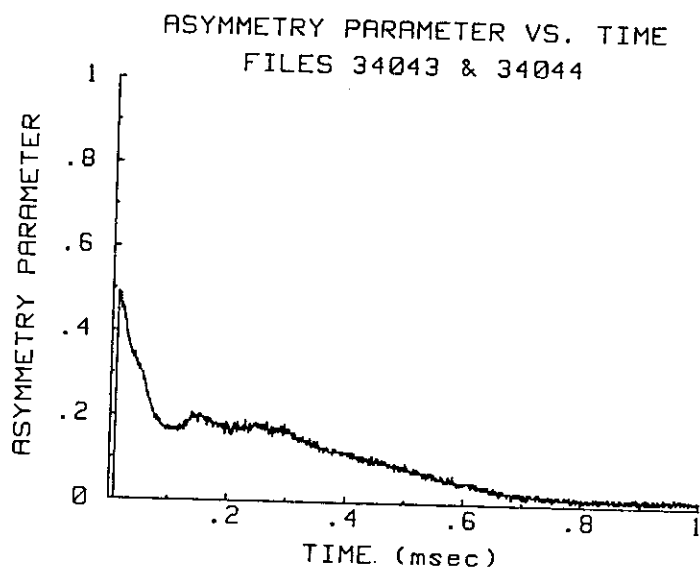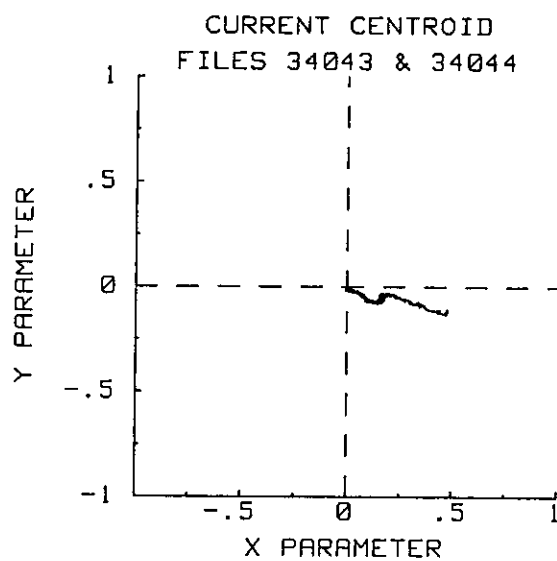
J = 4.5 kA,   ṁ = 5.9 g/s,   Probes 2 cm from Backplate

Figure 4-3c

will be referred to as the steady state offset, is caused by three factors. First, uncertainty in the probe calibration and positioning is expected to contribute up to 0.02 to the asymmetry parameter. Second, uncorrelated oscillations in the field at each probe are unassociated with bulk asymmetry, but they do contribute to the parameter. From the top graph on Figure 4-2, it is obvious that these fluctuations increase with total current. Experience has shown that they actually increase with $J^2/\dot{m}$ and can have quite a significant effect on the parameter at values of $J^2/\dot{m}$ over 100 kA^2s/g. Third, there is a possible contribution from steady asymmetric behavior. In a few of the discharges at 4 kA, asymmetry parameters of .1 or more persisted throughout the pulse, indicating either a transient time longer than 1 ms or a mode of steadily asymmetric behavior that occurs infrequently and only at this low a current. However, for most discharges, the asymmetry parameter drops below 0.03, and the possible contribution from steady asymmetric behavior is only a fraction of that, so the degree of overall asymmetric behavior is negligible after the transient ends.

An additional evaluation of the steady asymmetric behavior can be made by using the probes to measure the azimuthal variation in magnetic fields at other axial positions. Figure 4-4 shows a plot of the asymmetry parameter with the probes at the 4.5 cm radial position as a function of axial positions, using the time average of the magnetic field at each probe between 700 and 800 μs to calculate the parameter. Since the time dependent fluctuations average out, the values of the asymmetry parameter in this plot are due to steady azimuthal variations in the field. These data validate the assumption of azimuthal symmetry when measuring the field with a single probe. The asymmetry parameter is approximately equal to the maximum deviation of the steady field at one probe from the average steady field at that axial and radial position, divided by that average steady field:

$$\text{Max } |B_i - B_{avg}| / B_{avg},$$

where $i = 1, 2, 3,$ or 4. B_i is the time average field at probe i, and $B_{avg} = \Sigma B_i/4$. The plot in Figure 4-4 shows that most variation in steady state field measurements occurs near the anode. In addition, the fields at lower currents show more variation than those at higher currents, indicating a

Asymmetry Parameter vs. Axial Position

Asymmetry Parameter calculated from steady state magnetic field
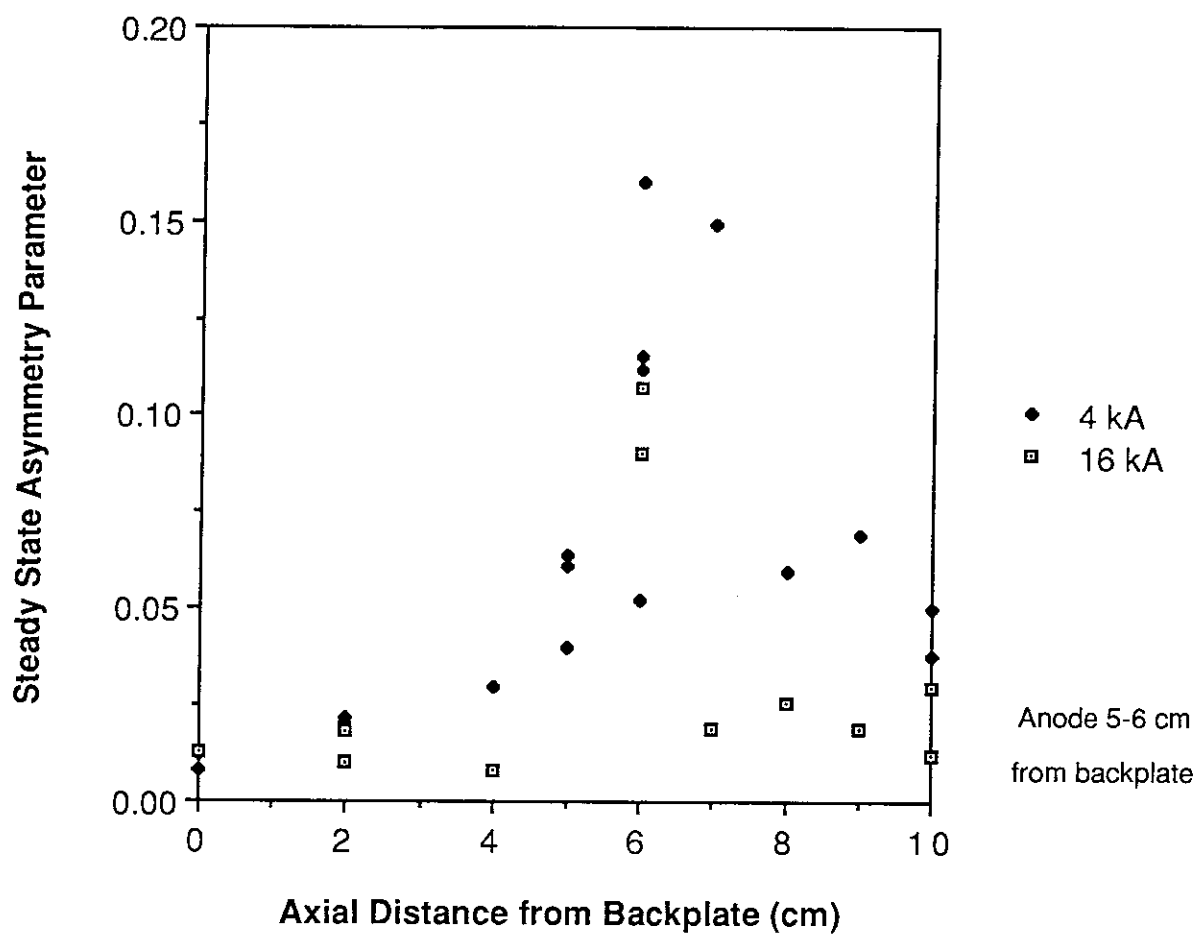
Figure 4-4

greater susceptibility to steady asymmetric behavior at lower currents. However, these variations are small everywhere except near the anode when compared with other uncertainties associated with making absolute magnetic field measurements.

The angular position of the steady state offset has no correlation with the maximum field during the transient (Figure 4-5), so these steady state variations in the field are not merely a residual part of the asymmetric transient phenomenon. Since the largest deviations from azimuthal uniformity occur only in regions of high current density, they can be attributed to small variations in the current density local to the probe, rather than with overall asymmetric behavior. Therefore, the overall steady behavior, as indicated by the steady state parameter at the 2 cm position, is very symmetric, even though larger steady variations exist near the anode.

Magnetic field measurements taken simultaneously with photographic sequences demonstrate the correlation between luminosity patterns and the field measurements at the 2 cm position (Figure 4-6). On the left side of the figure is the first ten frames of the photographic sequence, with the time after discharge initiation for each frame. The cathode is visible as the light disk in the center of each frame. The plot to the upper right shows the position of the current centroid during each frame. At the lower right, the asymmetry parameter is plotted versus time for the duration of the discharge. The location of each frame in the development of the discharge is marked by the dashed vertical lines. The parameter of 0.02 that persists throughout the discharge, as well as the fact that the calculated centroid position in frames 9 and 10 lie slightly off center, can be attributed to uncertainties in the probe calibration and positioning. Over the development of the discharge, the central angular position of the luminosity corresponds to the position of the current centroid, demonstrating that the luminosity pattern around the cathode is a good indicator of the azimuthal distribution of current. Figure 4-7 demonstrates an excellent correlation between the central angular position of luminosity in time-integrated photographs and the position of the current centroid during the initial transient for discharges at 4 kA and 5.9 g/s. The uncertainty on both axes is ±10°. It is clear from this correlation that the asymmetric behavior observed in the luminosity studies is

72

Angular Position of Steady Offset vs. Initial Asymmetry
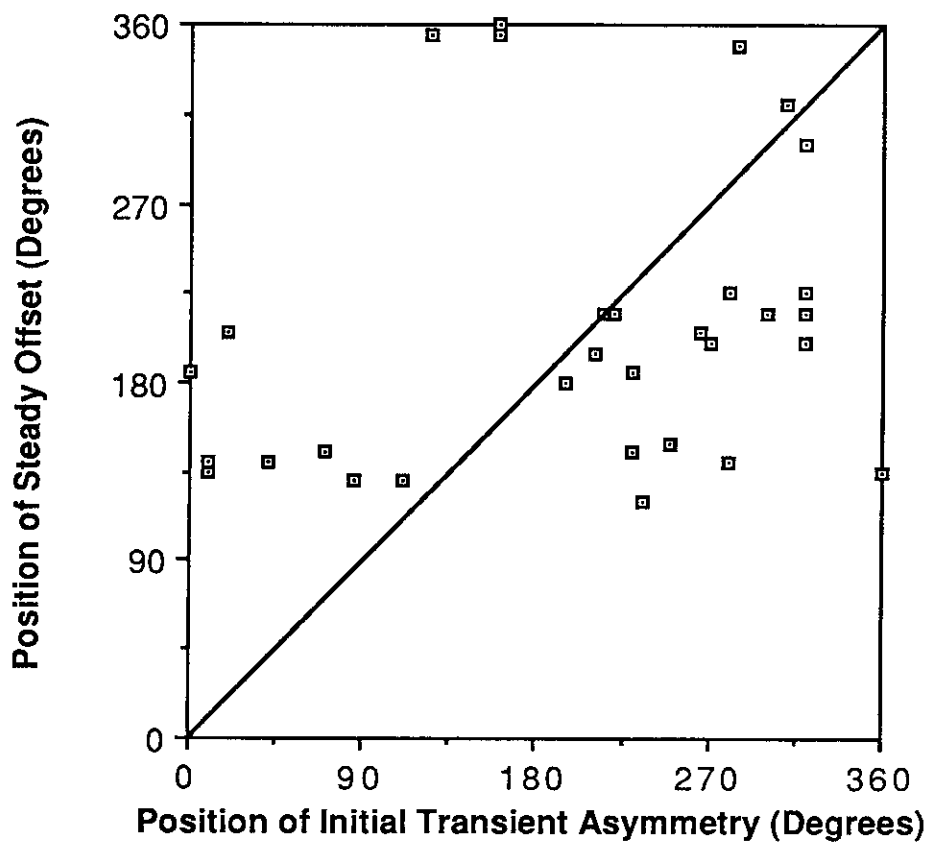
Figure 4-5

Fr.	Time (μs)
1	43
2	93
3	143
4	194
5	244
6	294
7	344
8	394
9	445
10	494

Framing Period = 50.2 ± .1 μs

Absolute Uncertainty = ± 2 μs

CI_34467-9

CURRENT CENTROID
FILES 34468 & 34469

Y PARAMETER
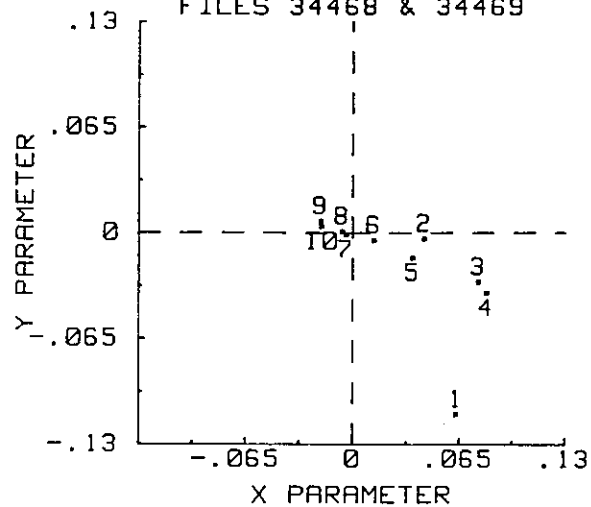
X PARAMETER

ASYMMETRY PARAMETER VS. TIME
FILES 34468 & 34469

ASYMMETRY PARAMETER

TIME (msec)
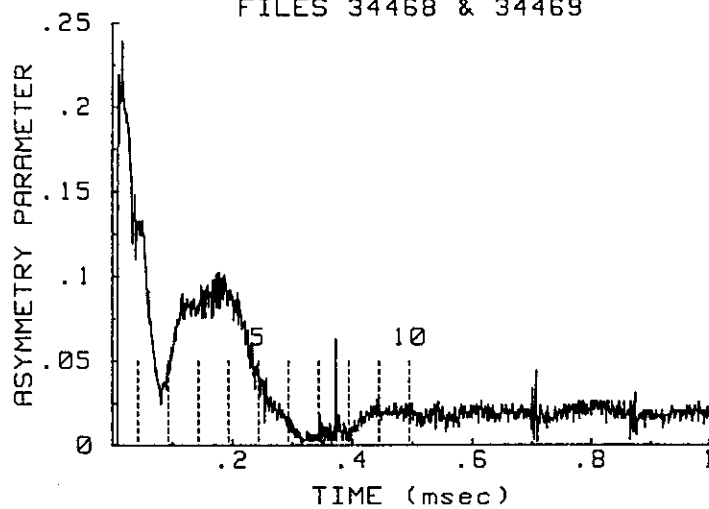
488 nm light,   J = 7.7 kA,   ṁ = 5.9 g/s
Figure 4-6

Angular Position of Asymmetry: Probes vs. Photographs
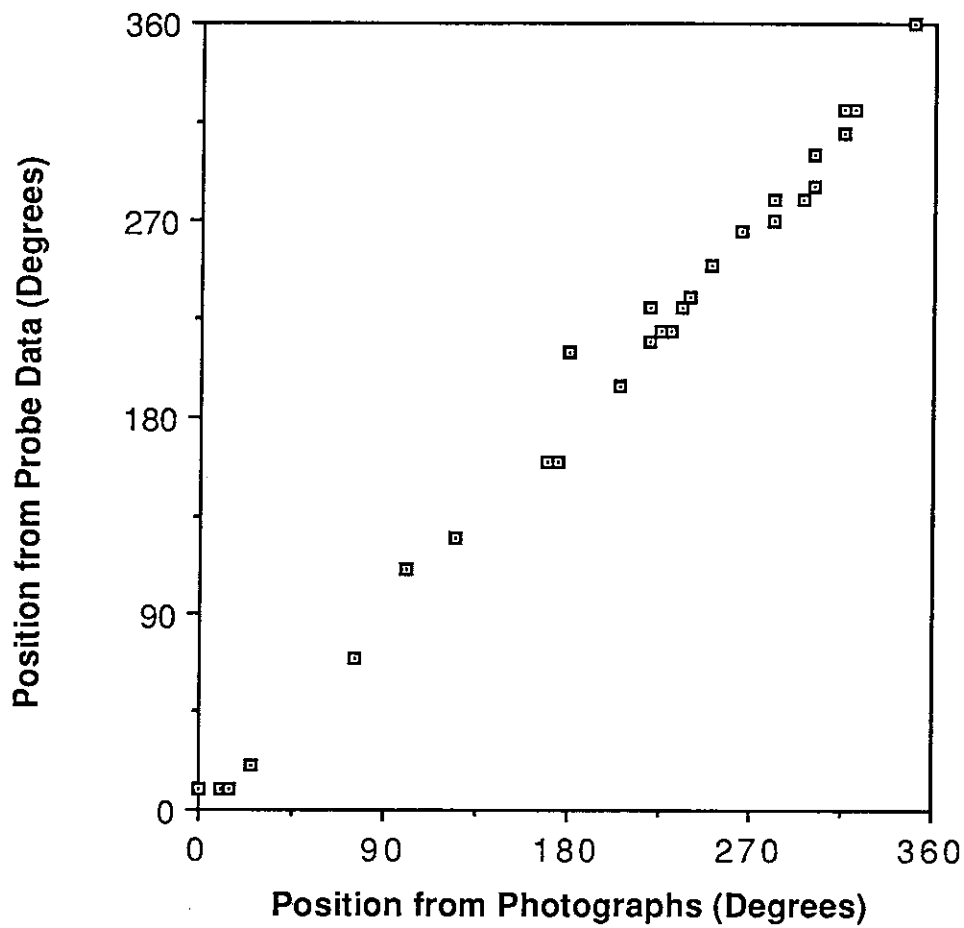
Figure 4-7

strongly associated with the transient behavior observed in the magnetic field measurements at 2 cm from the backplate.

An important feature revealed by the plots of magnetic field data is that the current centroid does not revolve or oscillate around the center of the thruster. The measured position of the centroid stays at roughly the same azimuthal position while moving in radially until it reaches the center, which corresponds to the establishment of a symmetric discharge. This observation is also consistent with the observation made in Chapter 3, and apparent in Figure 4-6, that the azimuthal position of maximum luminosity is stationary while the plasma spreads equally around the cathode in both directions. These results demonstrate conclusively that the eventual symmetric appearance of the luminosity is due to a symmetric discharge pattern, not due to a rapidly moving spoke, as is sometimes the case in an applied field thruster.[28]

The dip in the asymmetry parameter at about 100 μs in Figure 4-6 is a feature exhibited by several, but not most discharges. Figure 4-6 shows how this dip is accompanied by a more uniform luminosity pattern, suggesting that the current distribution is temporarily more symmetric. Since the dip usually occurs at about 100 μs, it is associated with the bright phase and the disappearance of a time derivative in the total current. Because of the widespread 488 nm radiation during the bright phase, charged species number densities are hypothesized to be high throughout the thruster, which may lead to a more uniform conductivity in some cases. The current centroid, as well as the center of the luminosity pattern, usually retains its azimuthal position after the dip is over.

Two other features of the luminosity patterns were not well correlated with magnetic field measurements. Although a typical magnetic field trace just downstream of the anode at 4 kA and 5.9 g/s (Figure 4-8, top) has irregular fluctuations similar in occurrence and duration to the luminous spikes and bulges seen in unfiltered sequences at the same conditions (Figure 3-9), a limited series of simultaneous measurements did not show a direct correlation between the two. As $J^2/\dot{m}$ increases, the fluctuations in the magnetic field increase in frequency and amplitude

4.2 kA, 5.9 g/s

B-PROBE TRACE - CI 34022

16.6 kA, 5.9 g/s

B-PROBE TRACE - CI 34019
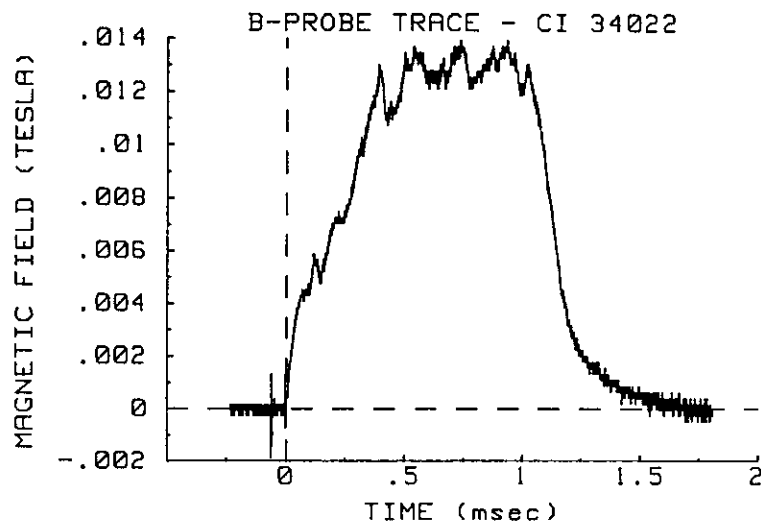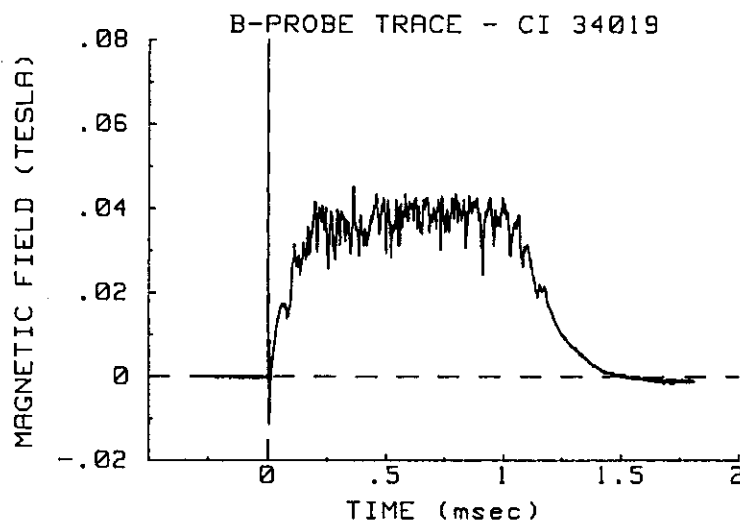
Magnetic Field Data with Probes 6 cm from Backplate

Figure 4-8

(Figure 4-8, bottom). However, no accompanying phenomena is observed in the luminosity for two possible reasons. First, the oscillations have a high enough frequency (> 100 kHz) that any luminous signature would wash out over the course of one framing period. Second, the increased pumping force tends to induce steep radial gradients in the number density of charged particles. Any non-uniformities in the current density might not be visualized because of the relatively low number density of argon ions outside the barrel radius. Attempts to correlate the local appearance of the irregular luminosity that appears near the anode at currents of 12 and 16 kA at 5.9 g/s (Figure 3-12) also proved unsuccessful. Since the frequency and duration of this type of luminosity is not consistent with the character of the magnetic field oscillations, it is not likely that this anomalous luminosity is correlated with changes in the local current distribution.

4.3 Effect of Thruster Condition on Asymmetric Behavior

As was discussed in section 3.2, the fact that the angular position of the initial asymmetry may change from shot to shot, but has preferred positions, suggests that the position is determined by some physical aspect of the thruster,such as the mass injection system or the electrode surfaces. An early study suggested the possibility of a correlation between the preferred location of the asymmetry and slight differences in the flow rates of the 12 outer injection holes. To investigate that possibility, a series of tests was conducted at 4 kA current and 5.9 g/s total mass flow rate, in which up to three adjacent outer holes were blocked with boron nitride plugs. The results showed no correlation between the position of the plugged holes and the position of the initial transient asymmetry or the position of any steady state offset (Figure 4-9). The discharges tend to group at particular positions for each series, but these positions are not consistently directed toward or away from the plugged holes.

To evaluate the effect of the plugs on the degree of asymmetry, the average asymmetry parameter was determined for each discharge by integrating the asymmetry parameter by time over the entire pulse and dividing by the length of the pulse:

Position of Transient Asymmetry vs. Position of Plugged Holes
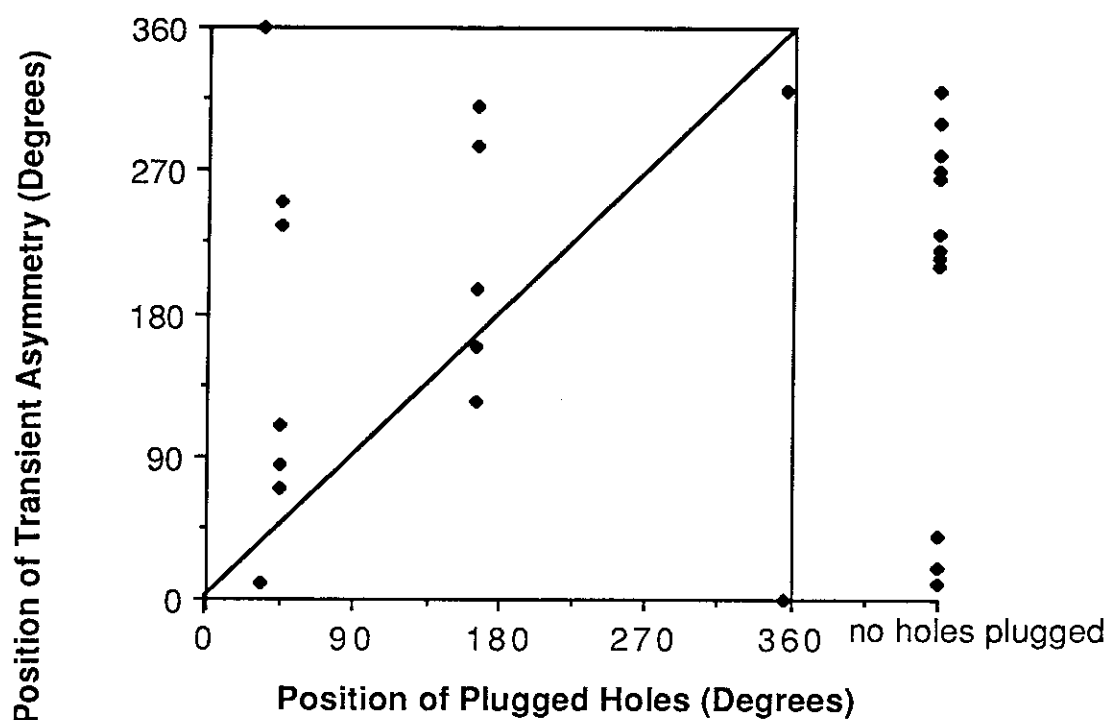
Position of Steady Offset vs. Position of Plugged Holes
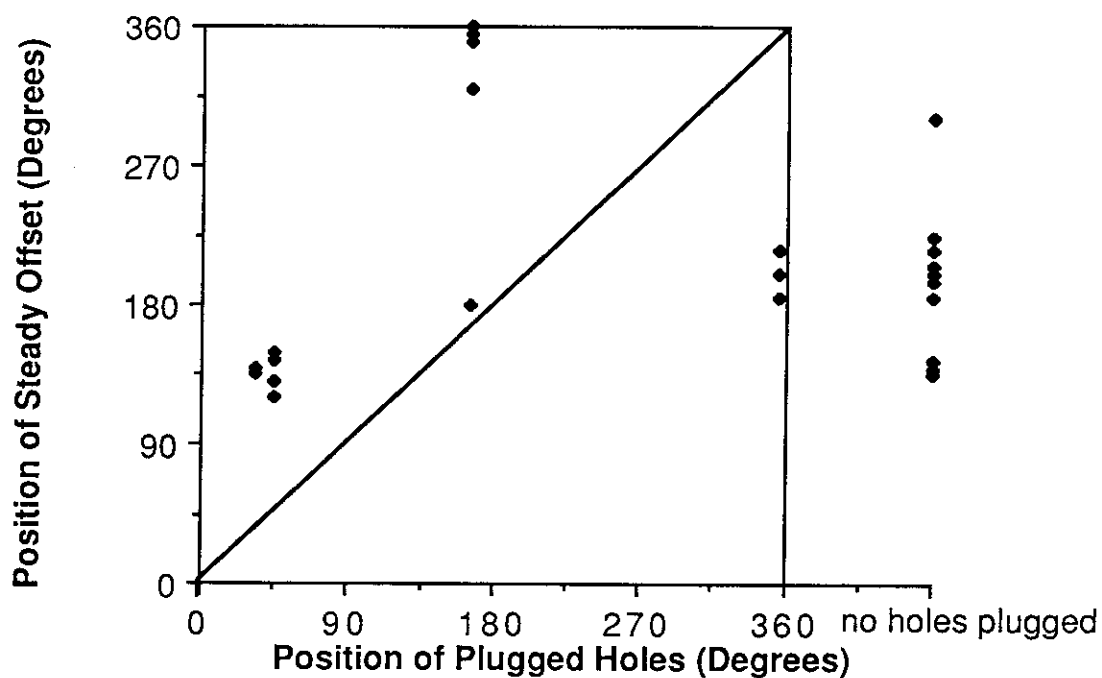
Figure 4-9

$$\langle A \rangle = [\int_0^T A(t) \, dt] / T,$$

where T is 1 ms, the pulse length. From Section 4-1:

$$A(t) = \{[D_{13}(t)]^2 + [D_{24}(t)]^2\}^{1/2} / R.$$

The results, plotted in Figure 4-10, demonstrate that the presence of plugs does not increase the average asymmetric behavior over the whole pulse. However, examination of the average asymmetry parameter over the last 100 μs of the discharge reveals some significant changes in the steady state offset over the course of this test series (Figure 4-11). The interesting aspect of this data is that the increase in steady state asymmetry over the first 15 discharges is not dependent upon the presence of plugged holes. When all plugs are removed after discharge 14, the asymmetry parameter does not revert to earlier low levels. Instead, the asymmetry is found to decrease after firing several high current discharges. The increase in steady asymmetric behavior noted earlier can be linked to venting the tank and handling the thruster to change the number of plugs. The high current discharges restore the steady asymmetry to the previous low level. When high current discharges were fired after subsequent venting events, little or no increase in asymmetry was noted.

When the thruster was fired with 16 kA current at 5.9 g/s, however, the current density and luminosity drop dramatically in the azimuthal location adjacent to the plugged holes. The three plugged holes are located at 135°, 165°, and 195° counter-clockwise from horizontal in the top photograph in Figure 4-12. Note that they are on exactly the opposite side of the thruster in the bottom photograph. The short, bright lines near the anode inner edge are the probes as viewed axially and through the circular probe support ring (cf. Figure 2-5). The magnetic field 9 cm downstream of the backplate exhibits steady azimuthal gradients of 40% across the thruster, demonstrating that the effect of the decreased current density persists well outside the chamber. The strong dependence of discharge symmetry on mass injection symmetry at high values of $J^2/\dot{m}$ is consistent with the recent observation by Merke et al.[29] that the onset condition can be raised by ensuring a more symmetric mass flow.

The effect of the anode condition on symmetry was demonstrated fortuitously when the

Average Asymmetry Parameter for Plugged Hole Series

Integral average of the asymmetry parameter over the whole pulse
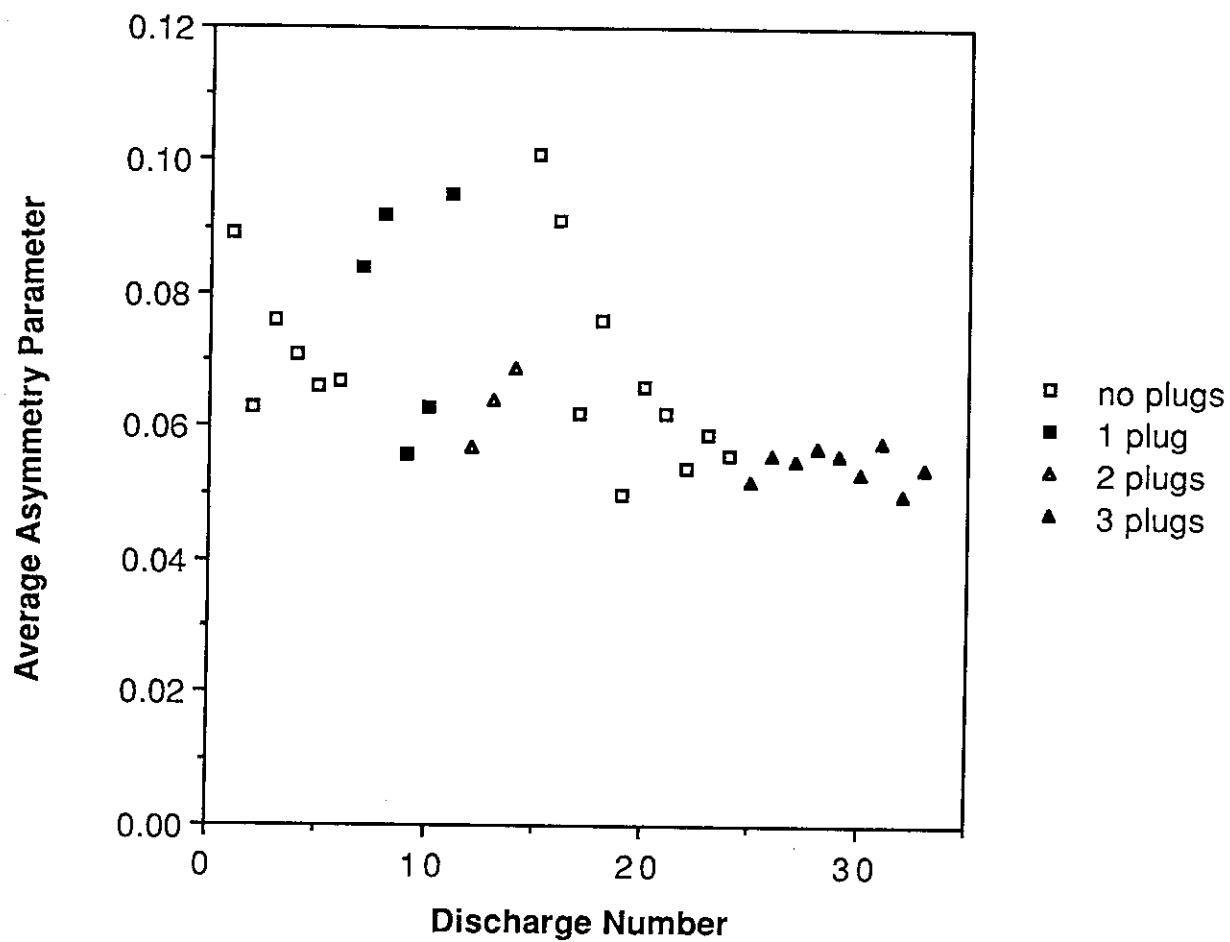
Figure 4-10

Steady Asymmetry Parameter for Plugged Hole Series

Average asymmetry parameter over last 100 microsecs. for 4 kA discharges

Several 24 kA conditioning discharges

were fired at these points in the test series

no plugs
1 plug
2 plugs
3 plugs

Discharge Number

Avg. Asymmetry Parameter During Steady State
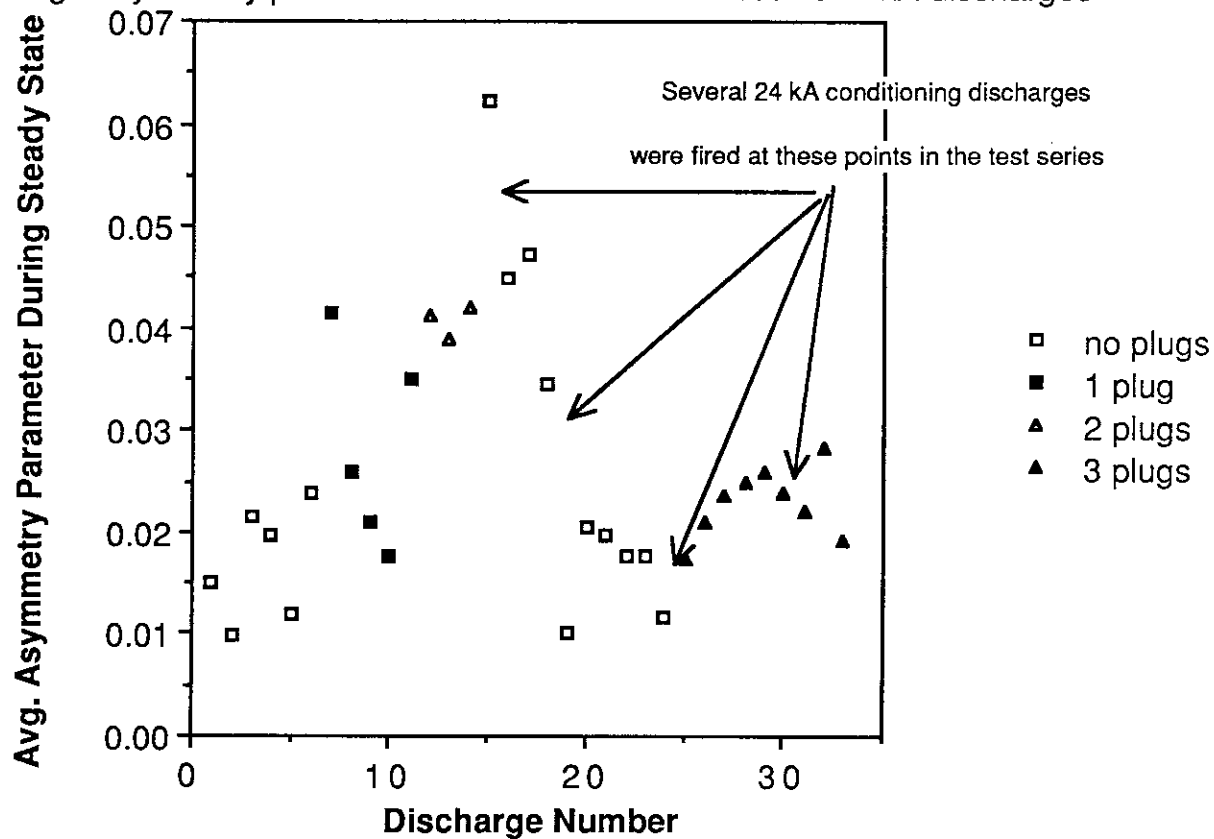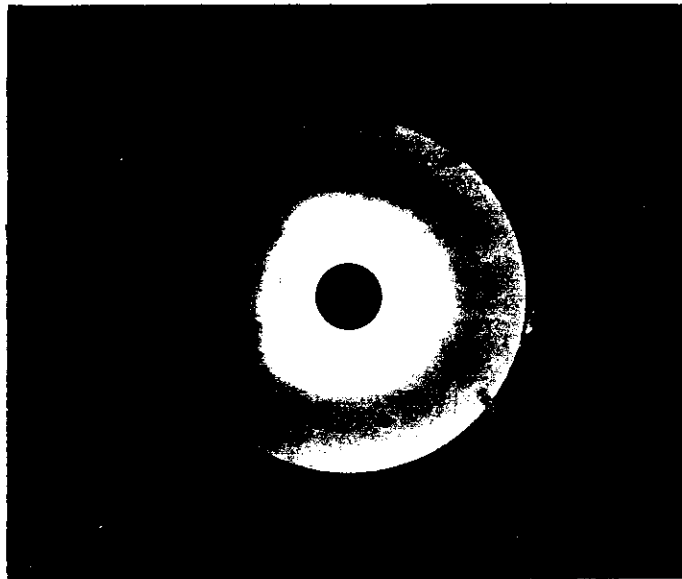
Figure 4-11

16.3 kA;   5.9 g/s

Plugs in upper left
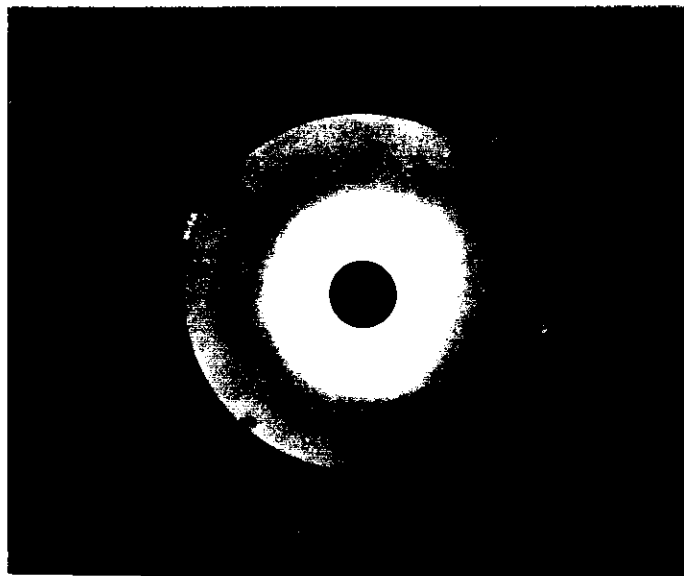
16.4 kA;   5.9 g/s

Plugs in lower right

End View 488 nm Photographs

of Discharge with Plugged Holes

Figure 4-12

anode became contaminated during an earlier series of discharges and could conduct only at selected sites. The change in anode condition was signaled by the appearance of bright regions of 488 nm radiation over the anode surface along its inner edge. In addition, the current centroid is off center in the direction of the brightest spots with a steady offset of 0.08 (Figure 4-13). These observations suggest that the increasing steady offset in the first 15 discharges of the plugged hole tests (Figure 4-11) is due to changes in the anode surface condition resulting from handling during insertion and removal of the plugs. Subsequent high current operation may have removed the contamination and restored the anode to its original condition. The role of the anode in determining the symmetric nature of the steady state discharge is consistent with Nishida's work[10], which shows that the use of an azimuthally segmented anode with equal current flow to each segment produces visually uniform discharges.

The most striking feature of the discharges with abnormal anode conduction is that the location of the initial asymmetry is independent of the asymmetric anode conditions. Along with the observations that argon ion radiation first appears in a few sites near the base of the cathode and that the direction of the asymmetry is also independent of the mass injection symmetry, this observation indicates that non-uniformities of the cathode surface determine the angular position of the initial asymmetry. Although a controlled, direct study of the effect of the microscopic condition of the cathode surface was not feasible, this conclusion is consistent with the fact that cathode emission processes have the dominant role in determining when and where breakdown occurs. The exact location of breakdown is known to depend on the condition of the cathode surface, namely the local work function and microscopic geometry, and the presence of impurities such as dust particles.[26] The work function in an area of the cathode may be lowered by chemical changes of the surface layer resulting from contamination.[30] If these changes in the surface layer are not removed by low current arcs, the arc may strike repeatedly in one region. In summary, all observations are consistent with the hypothesis that the local conditions of the cathode surface determine the angular position of the initial asymmetry.

CURRENT CENTROID
FILES 34277 & 34278

ASYMMETRY PARAMETER VS. TIME
FILES 34277 & 34278
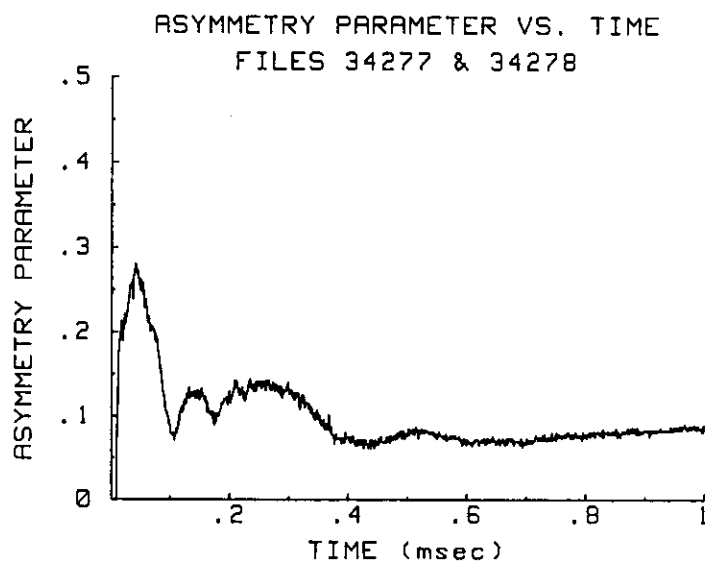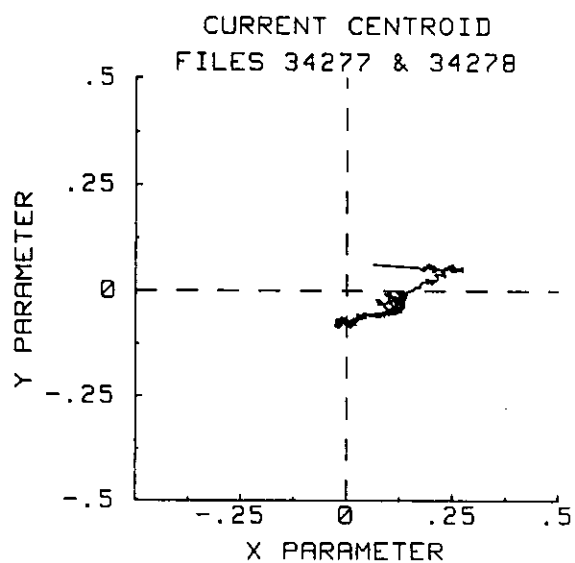
5.75 kA, 5.9 g/s Discharge

with Abnormal Anode Conduction Pattern

Figure 4-13

4.4 Effect of Operating Condition on Asymmetric Behavior

Four major factors contribute to the value of the average asymmetry parameter: initial transient asymmetry (the major contributor under most conditions), steady asymmetry (shown to be negligible in most discharges), uncorrelated field oscillations (which grow with $J^2/\dot{m}$), and experimental uncertainty (independent of the operating condition). As $J^2/\dot{m}$ increases, the contribution of the field oscillations, which do not indicate overall asymmetric behavior, dominates that of the overall asymmetric behavior and makes this parameter questionable as a measure of overall asymmetric behavior. The plots in Figure 4-14 show typical magnetic field data for a 20 kA, 3.5 g/s discharge. Magnetic field oscillations, manifest in the plot at the top, induce large non-zero values in the calculated asymmetry parameter even though the discharge is essentially symmetric after 200 μs.

To remove the effect of these oscillations, the "net asymmetry parameter" is defined as the average asymmetry parameter over the whole pulse minus the steady state offset:

$$N = <A> - <A>_{ss} = [\int_{o}^{1\,ms} A(t)\,dt]\,/\,[1\,ms]\ -\ [\int_{t_{tr}}^{t_{ss}} A(t)\,dt]\,/\,[1\,ms - t_{tr}],$$

where t_{tr} is the transient time. Since the steady state offset represents the combined contribution of steady asymmetry, experimental uncertainty and local field oscillations, the net asymmetry parameter is a measure of the initial transient asymmetry alone. The net asymmetry parameter is plotted versus current and $J^2/\dot{m}$ in Figure 4-15 for a range of flow rates with the probes 2 cm from the backplate. The data obtained at different flow rates indicate a dependence of the asymmetric behavior on mass flow rate and that asymmetry is enhanced at higher flow rates (lower $J^2/\dot{m}$). The $J^2/\dot{m}$ plot shows better mixing of data from different flow rates, demonstrating that $J^2/\dot{m}$ is the more appropriate scaling parameter for asymmetric behavior than current. The plot also shows a sharp decrease in asymmetry with rising $J^2/\dot{m}$.

The duration of the transient, t_{tr}, has been estimated to within ± 50 μs for each discharge from the plots of asymmetry parameter versus time. For example, the transient time for the discharge in Figure 4-3c is 700 μs. The plots of transient time versus current and $J^2/\dot{m}$ in
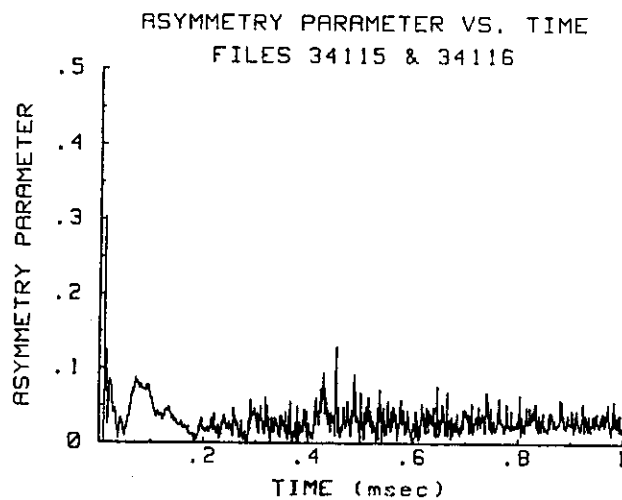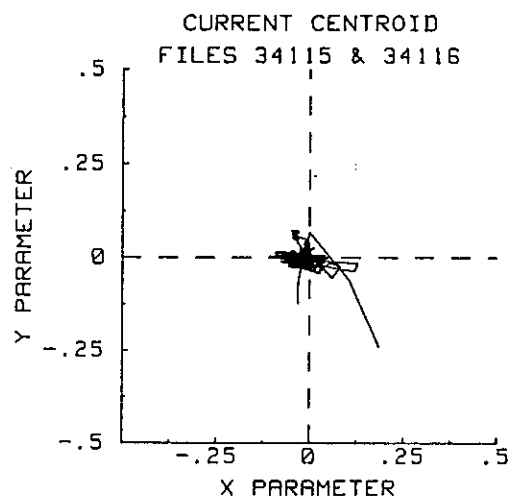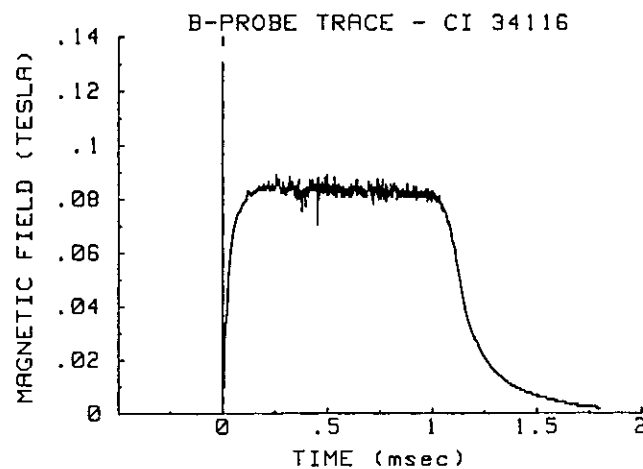
Magnetic Field Probe Data
J = 19.6 kA,   ṁ = 3.5 g/s,   Probes 2 cm from Backplate
Figure 4-14

Net Asymmtery Parameter vs. Current

Avg. during steady state subtracted from avg. over whole pulse
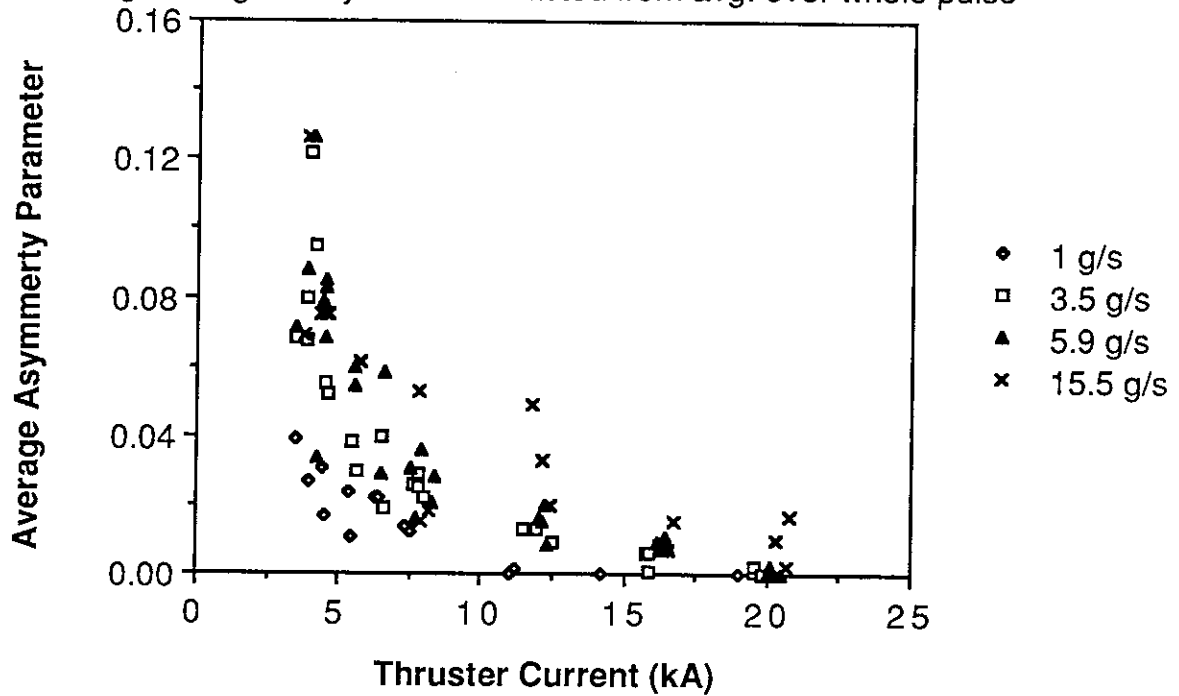
Net Asymmetry Parameter vs. J^2/mdot

Avg. during steady state subtracted from avg. over whole pulse
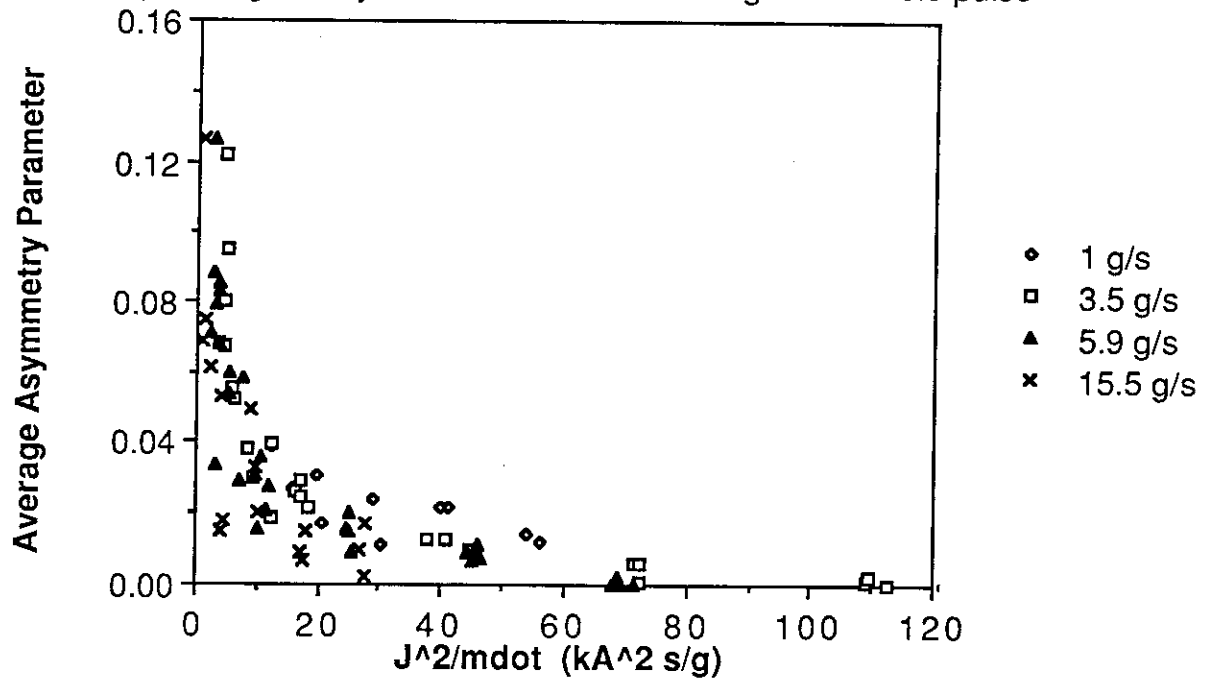
Figure 4-15

Figure 4-16 demonstrate a clear scaling with $J^2/\dot{m}$, and a sharp drop with increasing $J^2/\dot{m}$. These times have the same magnitude and trend as those measured from the photographic sequences. In addition, the time for axial stabilization of the current distribution, as measured by the probes at various axial positions, is similar to the time taken to achieve a symmetric discharge as well as the time in which the luminosity pattern achieves its steady state axial extent.

Since the net asymmetry parameter is essentially an integral under the asymmetry parameter versus time curve, it represents the product of the transient time and the average severity of the asymmetric behavior. In dividing the net asymmetry parameter by the fraction of the pulse over which the transient occurs, the average asymmetry parameter during the transient can be obtained, representing the severity of the asymmetric behavior. The plot of this average asymmetry parameter during the transient versus $J^2/\dot{m}$ in Figure 4-17 demonstrates a clear decrease in the severity of asymmetry with increasing $J^2/\dot{m}$. Figures 4-16 and 4-17 show that asymmetric behavior decreases in both duration and severity as $J^2/\dot{m}$ is increased.

Finally, the effect of the current rise time and capacitor bank charging voltage on asymmetric behavior was investigated by changing the configuration of the pulse-forming network (PFN). No evidence of a change in asymmetric behavior was observed by changing the current pulse rise time from 100 to 50 μs. Although no strong dependence on the charging voltage was observed, there is some evidence that increased charging voltages reduce the average asymmetry parameter for a given set of current and mass flow conditions. In two consecutive series of three discharges each, the PFN was configured such that the charging voltage required to produce a 4.5 kA discharge was 575 V and 1100 V, respectively. The average asymmetry parameter for the two configurations was 0.05 ± 0.01 and 0.029 ± 0.02, respectively. This trend is consistent with previous measurements[4] with a different PFN configuration, in which the bank was charged to 10 kV, and the discharge stabilization times for a 16 kA discharge at 6 g/s were typically as low as 20 - 30 μs as opposed to 100 to 300 μs seen with the present charging voltage of 2 kV for 16 kA. As discussed in the previous chapter, higher charging voltages tend to produce more locations of discharge initiation

89

Transient Time vs. Current

Times estimated from magnetic field probe data

Asymmetric Transient Time (ms) vs **Current (kA)**

Legend:
- ◇ 1 g/s
- □ 3.5 g/s
- ▲ 5.9 g/s
- ✕ 15.5 g/s

Transient Time vs. J^2/Mass Flow

Times estimated from magnetic field probe data

Asymmetric Transient Time (ms) vs **Current^2/Mass Flow (kA^2 s/g)**

Legend:
- ◇ 1 g/s
- □ 3.5 g/s
- ▲ 5.9 g/s
- ✕ 15.5 g/s
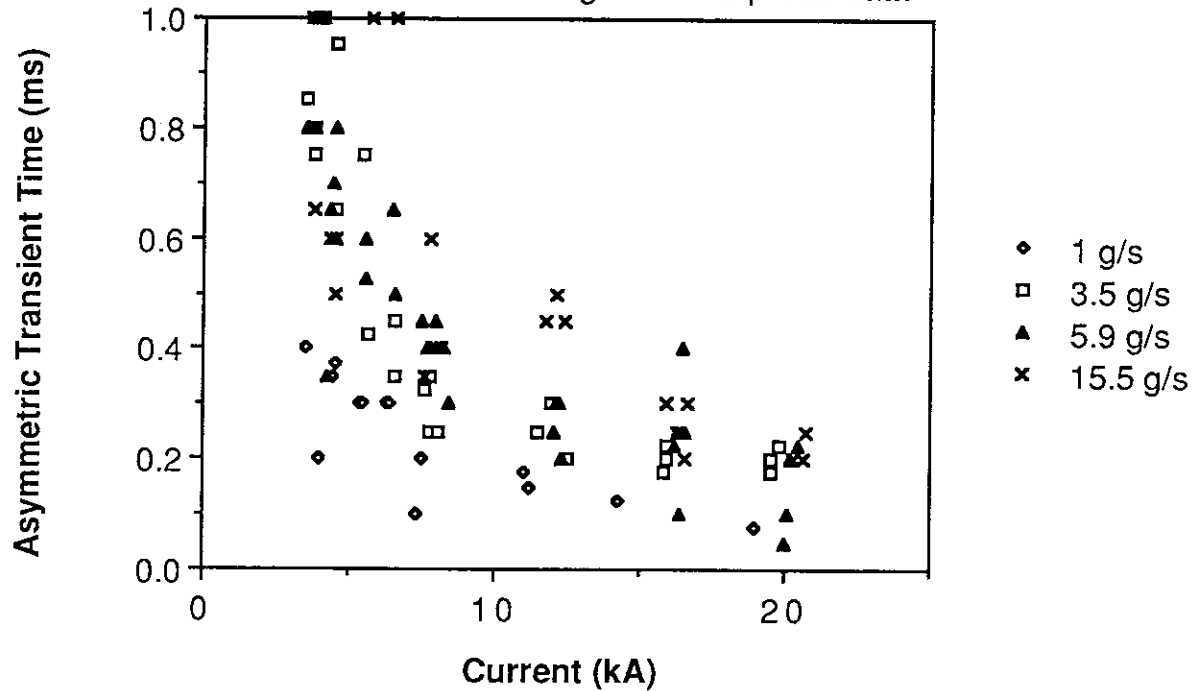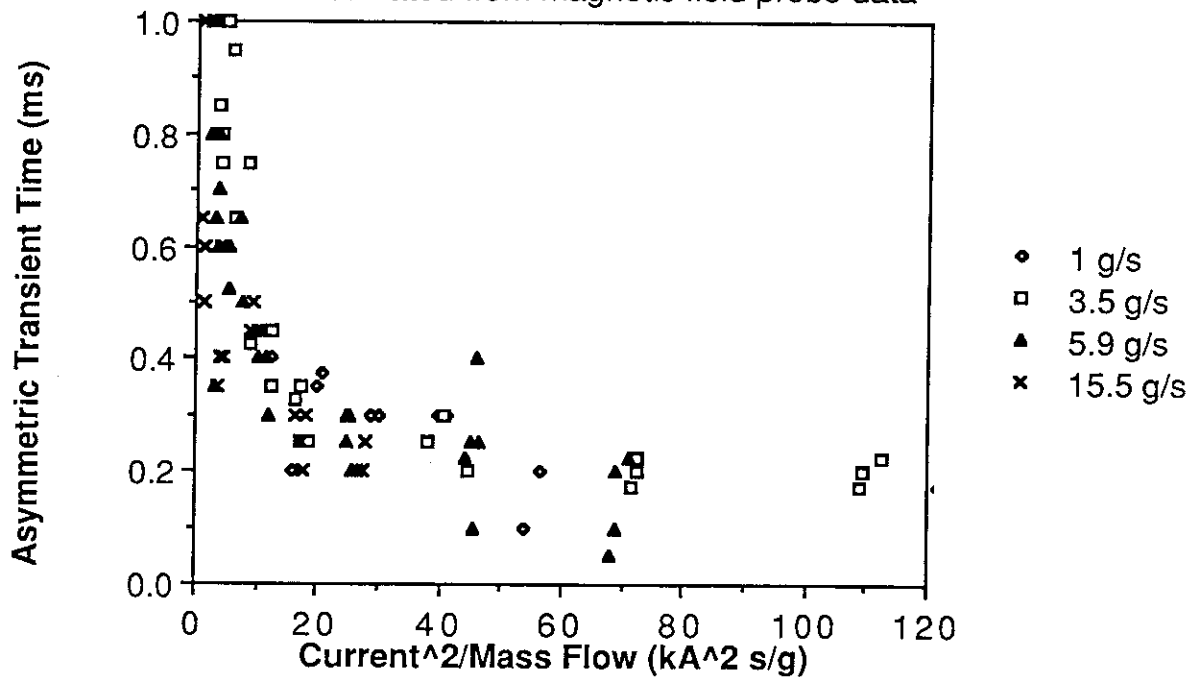
Figure 4-16

Asymmetry Parameter vs. J^2/mdot

Average Parameter During Transient
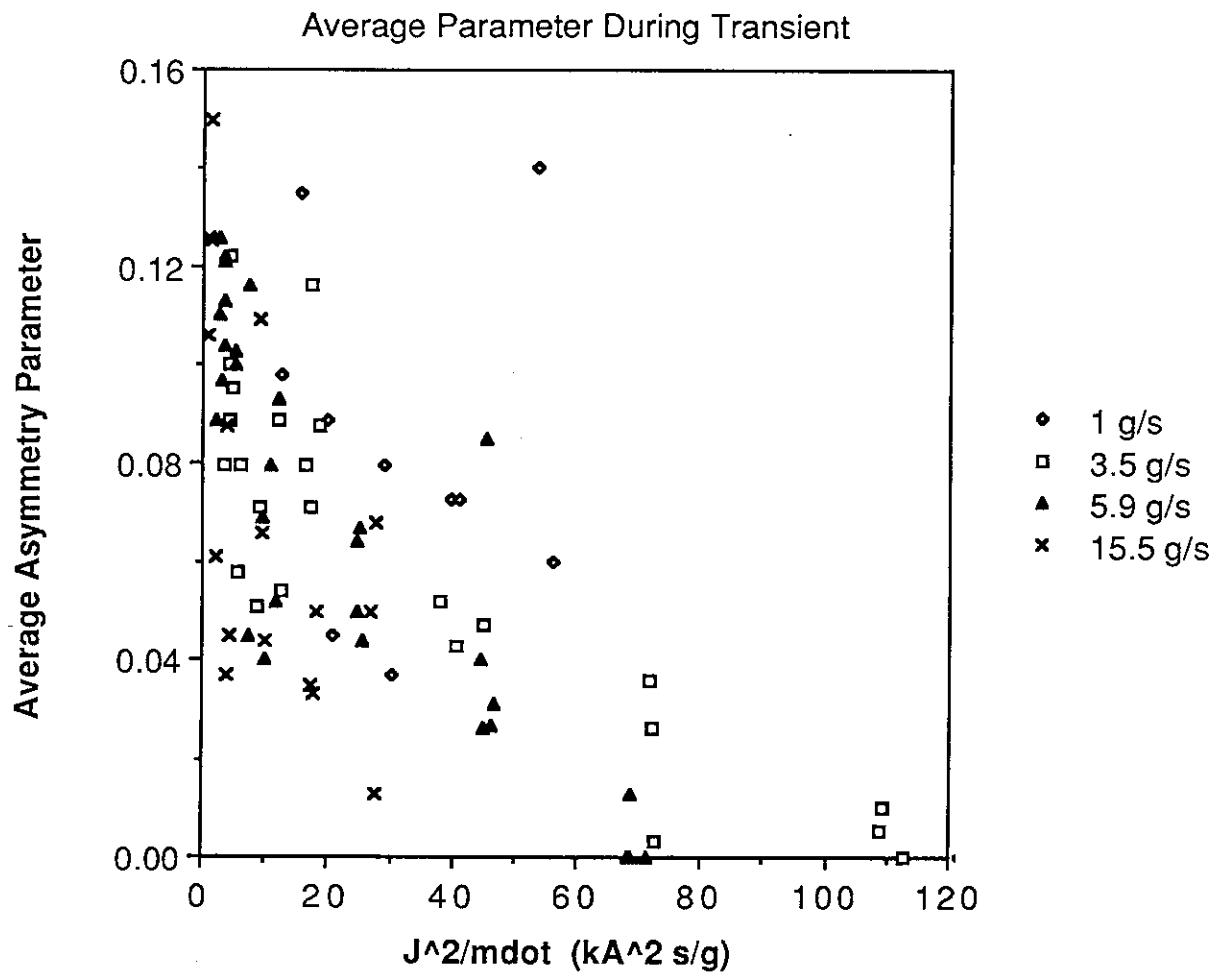
Figure 4-17

distributed around the cathode, and are expected to reduce the degree of asymmetric behavior since a higher voltage tends to produce a discharge that is initially more symmetric.

Chapter 5

DISCUSSION

5.1 Introduction

The picture that emerges from the data discussed in Chapters 3 and 4 is of a transient asymmetric phenomenon that begins with breakdown. As the discharge proceeds rapidly from an abnormal glow discharge to an arc, the large time derivative in the magnetic field induces electric fields that confine the current conduction to the upstream portion of the thruster. The transition to an arc occurs in a fraction of a microsecond when small spots at the base of the cathode, heated by a combination of internal resistance in the tungsten and ion bombardment, begin producing large quantities of electrons by thermionic emission. The initiation of one of these breakdown sites is favored by a locally low work function due to oxidation and other impurities[30] and a locally high electric field due to microscopic protrusions and dust particles.[26] Because cathode spots on tungsten are limited to currents of about 300 A, these initial spots split and form more spots in a cluster around the original site as the thruster current rises further.[27]

Meanwhile, electrons in regions of high current density ionize argon atoms in the flow over the cathode spots to produce a region of rising conductivity. These regions of ionization over the initial spot clusters are visible in end view photographic sequence frames taken during the first few microseconds of the discharge pulse (Figures 3-7 and 3-13). The scalar conductivity of a weakly ionized plasma increases linearly with the number density of charged particles:

$$\sigma = n_e e^2 / m_e \nu_{en},$$

where n_e is the electron number density, e is the fundamental charge, m_e the electron mass, and ν_{en} is the collision frequency between electrons and neutrals. Neglecting recombination, the increase in n_e is given by :

$$dn_e/dt \approx n_e u_e n_n Q_{en}{}^i = (j/e) n_n Q_{en}{}^i,$$

where the current density, j, is assumed to arise primarily from electron flow, and $Q_{en}{}^i$ is the

93

collision cross section for electron impact ionization. Therefore, regions of high current density experience a more rapid increase in conductivity. Regions of higher conductivity, in turn, will carry a higher current density for a given electric field.

When the ionization fraction reaches a few tenths of a percent, the conductivity is controlled by coulomb interaction between electrons and ions and no longer depends strongly on the electron number density. Instead, conductivity is proportional to the electron temperature to the 3/2 power.[24] Assuming the plasma to be stationary for the time being, neglecting losses to radiation, and assuming that heating the plasma occurs in a time short compared to that required for conduction, the temperature of a volume element of plasma rises at a rate proportional to the power input per unit volume by resistive heating. That is,

$$\rho \, \partial(c_p T)/\partial t \; = \; \mathbf{j} \cdot \mathbf{E} \; = \; \sigma E^2,$$

where ρ is the density, c_p is the specific heat, and E is the electric field in the plasma. So, even in a more fully ionized plasma, the conductivity has a tendency to increase more rapidly in regions where there is already high conductivity. It is this thermal instability, especially in the initial weakly ionized plasma, which generates the asymmetric discharge pattern at the start of the pulse. The main question to be answered is what mechanism controls the eventual establishment of a symmetric discharge. Of the three mechanisms discussed in the following sections, one involves electrode control and two involve plasma control of the asymmetric behavior.

5.2 Cathode Spots

The observation in Chapter 3 that the luminous plasma becomes uniform around the cathode only when cathode spots have distributed themselves uniformly over the cathode surface casts suspicion on the motion of spots as a factor in the establishment of a symmetric discharge. In addition, although magnetic field probe data show good consistency within a test series, small but definite changes in the degree of asymmetry were observed between test series. These changes coincide with exposure to atmosphere or handling, both of which can change the condition of the

cathode surface. Studies of the motion of cathode spots have shown that the condition of the cathode surface has a strong effect on the speed of spots over the surface.[31] Since pulsed MPD thrusters tend to operate with the cathode too cold for adequate electron emission at the field strengths typically found at the cathode surface, significant current densities in the plasma over a region of the cathode must coincide with the presence of cathode spots. If the spread of cathode spots controls the spread of plasma rather than vice versa, the time required to establish a symmetric discharge would be dependent upon the manner in which the spots ultimately populate the surface.

Most work on the motion of cathode spots in the presence of a magnetic field has centered on vacuum arcs, in which the motion of the spot controls the motion of the arc since the spot itself provides the metal vapor for the plasma. Despite repeated efforts, spot motion is not well understood theoretically, but it is well documented experimentally.[27] Three observations in particular are pertinent to this discussion. First, at low pressures the spots move "retrograde" or opposite the usual direction of the $\mathbf{j} \times \mathbf{B}$ Lorentz force. Retrograde motion occurs not only in applied fields; clusters of spots have also been observed to move retrograde in their own self magnetic field. In other words, they spread out, in contrast to the expected constricting action of the self magnetic field. This retrograde motion might explain the spreading of the MPD discharge in the azimuthal direction from an initial cluster of spots. Second, for magnetic fields up to about 5×10^{-2} T, there is a linear increase in retrograde spot velocity with magnetic field strength. Since larger thruster currents will tend to generate larger magnetic fields, the dependence on field strength is consistent with the decrease in transient times at higher currents.

The third observation is that as the pressure of the gas over the cathode is increased, the spot velocity slows and eventually stops at a certain pressure that depends on the experimental conditions. Above that pressure, the spot motion reverses and proceeds in the expected $\mathbf{j} \times \mathbf{B}$ direction.[27,32] Measurements of the reversal pressure for argon over a tungsten cathode range from 50 to 600 mm Hg.[33] By comparison, Cory[34] measured the pressure at the wall of the chamber in the thruster used in this study to be 1 to 30 mm Hg, which is within the range for retrograde

95

motion. The decrease in spot velocity with increasing pressure is consistent with the increase in transient time with increased mass flow rate.

In spite of these promising indications, however, several factors make it unlikely that the spread of spots governs the establishment of a symmetric discharge. First, in addition to finding that the chamber pressure is a slightly increasing function of mass flow rate, Cory also found that pressure was a strongly increasing function of thruster current. This trend runs counter to the observation of a strong decrease in asymmetric transient times as current increases. Also, Cory's measurements were conducted at the outer radius of the chamber. The pressure at the cathode is increased significantly by the magnetic pumping force. Because the magnetic pumping force is also an increasing function of current, the pressure at the cathode surface should be an even stronger function of thruster current. Moreover, the sudden appearance of spots downstream on the cathode in frame 14 of Figure 3-10, with no evidence of migration from previously existing spots, demonstrates that the spots are not constrained to spread from an origin. Instead, spots may discontinuously appear on new regions on the cathode under these conditions, making it impossible to identify a spot migration speed from which a transient time may be predicted. So from a purely empirical perspective, it seems unlikely that the spread of cathode spots governs the establishment of a symmetric discharge.

5.3 Ambipolar Diffusion

The first plasma-based mechanism for establishing a symmetric discharge is the ambipolar diffusion of highly conductive plasma into regions of lower conductivity due to the large azimuthal gradients in pressure present in the asymmetric discharge. Although it is true that regions of higher current density increase the local conductivity by increasing the local temperature and charged particle number density, these higher temperatures and number densities create gradients that promote diffusion of the hot charged particles away from the regions of high conductivity. To assess the effectiveness of this mechanism, the ambipolar diffusion velocity will be estimated and

96

compared with speeds required to account for observed transient times.

Assuming that the perturbation from symmetry is small, the axial and radial components of the magnetic field have a negligible effect on the diffusion velocity. Because of the co-axial geometry of the thruster, there will be no azimuthal component of the electric field. The ambipolar diffusion velocity of the plasma through the surrounding neutral atoms is simply:

$$U_D = 1/m_{in}\nu_{in} \ (\nabla p_e/n_e + \nabla p_i/n_i), \quad 24$$

where $m_{in} = m_i m_n/(m_i + m_n) \approx m_n/2$. ν_{in} is the collision frequency between ions and neutrals:

$$\nu_{in} = n_n Q_{in}^{(e)} v_{in} = n_n Q_{in}^{(e)}(8kT/\pi m_i)^{1/2},$$

where $Q_{in}^{(e)}$, the elastic collision cross section between ions and neutral atoms, is $35 \times 10^{-20} \, m^2$.[35]

The number density of neutrals is estimated assuming rapid expansion of the injected propellant near the backplate to a uniform flow across the thruster:

$$n_n = \dot{m}/m_n u_n A_{th},$$

where u_n, the cold flow velocity, is on the order of 1000 m/s, and A_{th}, the cross sectional area of the thruster, is 0.013 m². By assuming that $T_i = T_e = T$ and $n_e = n_i$,

$$U_D = [(2\pi m_i)^{1/2} u_n A_{th} / \dot{m} Q_{in}^{(e)} (kT)^{1/2}] \cdot [\nabla n_i kT/n_i].$$

It is possible to estimate a range for the gradient from the photographs at different apertures in Figure 3-4. Examination of the photographs shows that the intensity of 488 nm argon ion radiation varies by a factor of 16 over roughly 1 cm. The intensity of the radiation of that wavelength is proportional to the number density of the excited state from which the transition was made. Assuming the excited states fall roughly in a Boltzmann distribution, the intensity is proportional to the total number density of ions and to an exponential term containing temperature. At one extreme, assuming a uniform temperature of 2 eV, a typical value for electron temperature,[17,36] the term in brackets at the right can be approximated as:

$$kT \cdot \nabla n_i/n_i \approx kT \cdot \Delta n_i/\Delta x \, n_{i \, avg} = kT \cdot 2(n_i - n_i/16)/(n_i + n_i/16)\Delta x = kT \cdot 180 \, m^{-1}.$$

Inserting these values at a mass flow rate of 6 g/s into the formula for U_D above, yields a diffusion speed of 400 m/s. At this speed, the plasma would spread 3 cm, or half the circumference of the

cathode, in about 75 μs.

On the other hand, assume that charged particle number density is relatively uniform across the thruster and that the variation in 488 nm intensity is primarily due to a temperature gradient. Due to the exponential nature of the dependence of intensity on temperature, the temperature in the bright region need only be ln(16) = 2.8 times higher than the surrounding dark region. Assuming that the temperature in the bright, high conductivity plasma is 2 eV, the diffusion velocity is 150 m/s. At this speed, the plasma would spread half the circumference of the cathode in 200 μs.

Although this range is somewhat faster than a transient time of about 600μs typical at the conditions for which the intensity gradient was measured, it is remarkably close, considering the very gross approximations made. In addition, the actual diffusion will be slowed by axial and radial components of the magnetic field created by the asymmetric discharge since these components are perpendicular to the direction of diffusion and act to produce a magnetic pressure directed against the diffusion. A further argument in favor of the diffusion mechanism is the inverse dependence of the velocity on mass flow rate, which is consistent with the experimental trend of longer transient times at higher flow rates. To account for the strong dependence of the transient time on thruster current, one would have to suppose that higher total currents generate stronger pressure gradients without a commensurate increase in the magnetic pressure that retards the expansion.

5.4 Magnetic Reynolds Number and the Back Emf

A second plasma-based mechanism that explains the observed asymmetric behavior involves the interaction between the moving plasma and the magnetic field, otherwise known as the "back emf." Neglecting contributions due to the Hall current and ion slip, Ohm's Law becomes:[1]

$$E = j/\sigma - uXB,$$

where σ is the scalar conductivity, u is the flow velocity, and uXB is the back emf. The total voltage drop, V_T, across the gap between the anode and cathode is the sum of the drop across the

electrode sheaths, V_S, and the plasma, V_P:

$$V_T = V_P + V_S = \int E \cdot dl + V_S = \int (j/\sigma) \cdot dl - \int (u \times B) \cdot dl + V_S$$

$$\text{along } j \qquad \text{along } j \qquad \text{along } j$$

Assuming that V_S does not vary much in the azimuthal direction, V_P must be the same no matter which current flow line is chosen for the path of integration for the right hand side of the equation. If the flow velocity arose primarily from the Lorentz force, **u** would be normal to the current flow, so:

$$V_P - \int uB \, dl = \int j/\sigma \, dl,$$

where the second term on the left is negative because **u×B** tends to be directed opposite **j** (see Figure 5-1).

As was demonstrated earlier, regions with high current density will tend to have high conductivity and vice versa for a plasma at rest. In the non-stationary case, however, a plasma region with high current density will tend to have a somewhat higher magnetic field strength since the field is generated by the current, as well as a significantly higher flow velocity since it is generated by a force proportional to both magnetic field and current density. As flow velocity increases, the equation above shows that the increased back emf will act to reduce the current density in that region (Figure 5-1). Some of the current requirement then shifts to regions with more moderate current densities and flow velocities.

By substitution of Ohm's Law into the expression for the total power input into the propellant, **j·E**, it is apparent that for the non-stationary plasma, only part of the power goes into Ohmic heating of the plasma:

$$j \cdot E = j^2/\sigma - j \cdot (u \times B).$$

j^2/σ represents the power that goes into heating the propellant, and **j·(u×B)** represents the power used to drive the propellant at the flow velocity, u.[1] As the local flow velocity increases, more power is being used to drive the propellant and less is available for the heating necessary to keep the
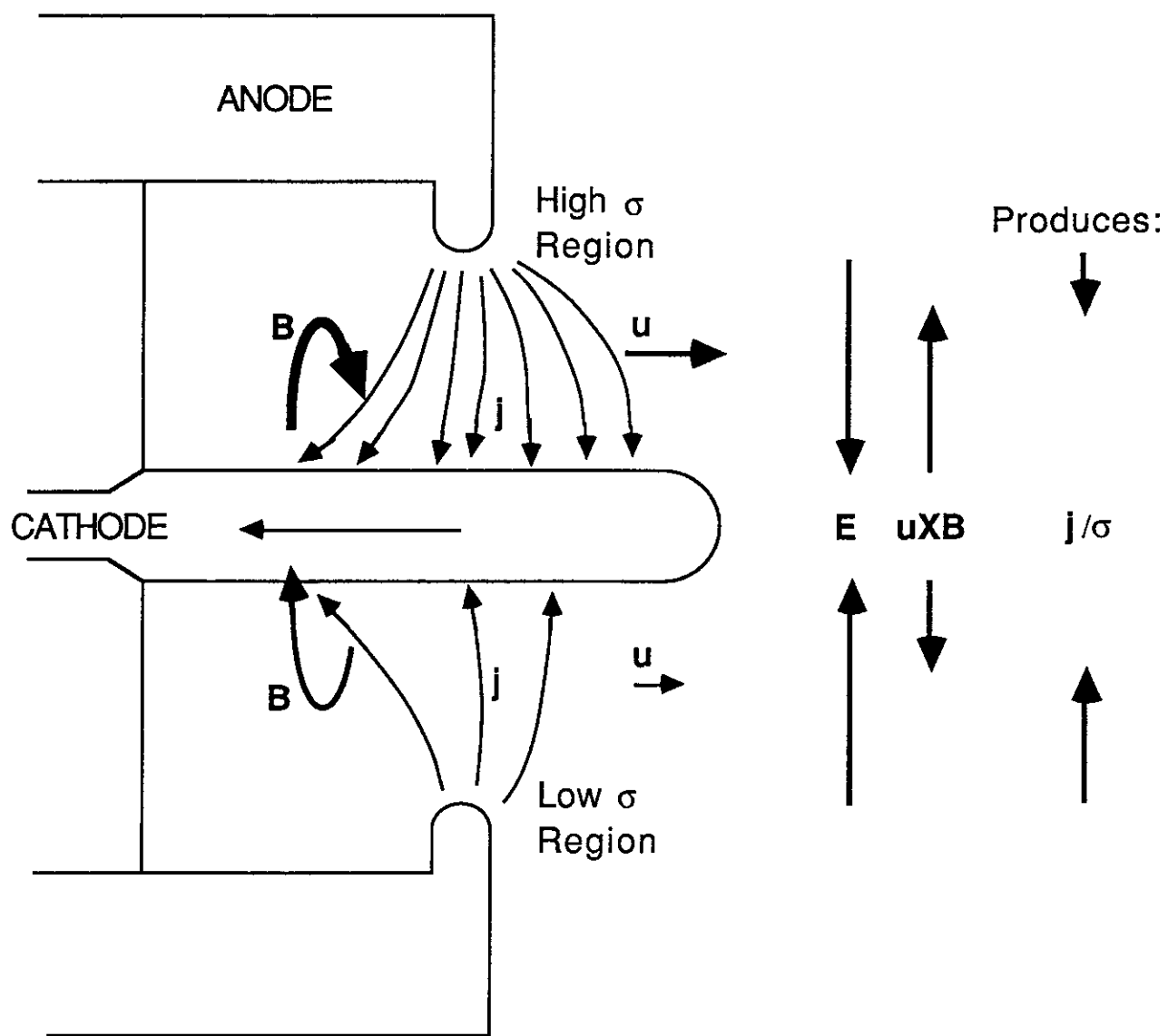
**Comparison of Back Emf between Regions
of Different Conductivity
Figure 5-1**

local conductivity high. As some of the total current requirement shifts to regions with lower conductivities, the increased power input there will involve proportionally more Ohmic heating because of the lower flow velocity in these regions. Under this mechanism the most stable configuration is one of azimuthal symmetry.

The impact of the back emf for given discharge conditions is determined by the importance of the $\mathbf{u} \times \mathbf{B}$ term relative to the $\mathbf{j}/\sigma$ term in Ohm's law. A good measure of this relative impact is the magnetic Reynolds number, which can be best understood from the magnetic diffusion equation. The magnetic diffusion equation is derived by eliminating $\mathbf{j}$ from Ohm's law with the Maxwell-Ampere relation:

$$(\nabla \times \mathbf{B})/\mu_0 = \mathbf{j},$$

and substituting $\mathbf{E}$ from Ohm's law into the Maxwell-Faraday relation:

$$(\nabla \times \mathbf{E}) = -\partial\mathbf{B}/\partial t.$$

Upon rearrangement of terms with the use of vector identities and the Maxwell relation, $\nabla \cdot \mathbf{B} = 0$, the magnetic diffusion equation emerges:

$$\partial\mathbf{B}/\partial t = (1/\sigma\mu_0)\nabla^2\mathbf{B} - (\nabla\mathbf{B})\cdot\nabla(1/\sigma\mu_0) + (\nabla(1/\sigma\mu_0)\cdot\nabla)\mathbf{B} + \nabla \times \mathbf{u} \times \mathbf{B}.$$

To derive the magnetic Reynolds number, this equation must be cast in non-dimensional form, which requires the following non-dimensional parameters:

$$\mathbf{B}' = \mathbf{B}/B_0, \quad t' = t/t_0, \quad \mathbf{u}' = (t_0/L_0)\mathbf{u} = \mathbf{u}/u_0, \quad \sigma = \sigma/\sigma_0, \quad \text{and } \nabla' = L_0\nabla,$$

where the subscript, $_0$, denotes characteristic values. Upon substitution,

$$\partial\mathbf{B}'/\partial t = (1/Re_m)[\nabla'^2\mathbf{B}' - (\nabla'\mathbf{B}')\cdot\nabla'(1/\sigma') + (\nabla'(1/\sigma')\cdot\nabla')\mathbf{B}'] + \nabla' \times \mathbf{u}' \times \mathbf{B}',$$

where $Re_m = \mu_0\sigma_0u_0L_0$. For $Re_m \ll 1$, the first three terms on the right, which depend on gradients in the conductivity, determine the current pattern. Therefore, the current pattern will be determined by the conductivity distribution. The conductivity distribution is determined by the production of heat and charged species, as described in section 5.1. In this regime, the discharge has a tendency to form a spoke, as happens in an electrothermal arcjet. For $Re_m \gg 1$, the last term on the right determines the current distribution. This is the convection term, which arises from the

101

back emf term in Ohm's law. In this regime, the discharge is highly sensitive to back emf, and azimuthal gradients in the flow velocity and magnetic field will tend to redistribute the discharge until it is symmetric.[17]

The magnetic Reynolds number can also be rearranged to show more explicitly that it represents the ratio of the back emf to the current conduction contributions:

$$Re_m = \mu_o \sigma_o u_o L_o \; = \; u_o B_o / (1/\sigma_o)[(1/\mu_o)(B_o/L_o)].$$

From Ampere's law $j_o \sim (1/\mu_o)(B_o/L_o)$, so:

$$Re_m \sim u_o B_o / (j_o/\sigma_o).$$

This formulation demonstrates that as Re_m becomes much larger than unity, the back emf dominates Ohm's Law, and the current conduction term becomes negligible in comparison.

An evaluation of the dependence of the magnetic Reynolds number on thruster condition reveals that it is consistent with observed asymmetric behavior. Since thruster-scale asymmetric behavior is of interest, the characteristic length scale, L_o, is defined as the diameter of the thruster, a geometric factor independent of the operating conditions. If the ionization fraction is above a few percent, the scalar conductivity depends only on electron temperature. Measurements have shown the steady state electron temperature to be relatively invariant with respect to operating conditions.[36] Thus, Re_m depends mainly on the flow velocity, which is proportional to $J^2/\dot{m}$. Therefore, the scaling of the asymmetric behavior with $J^2/\dot{m}$ can be explained by the dependence of asymmetric behavior on the magnetic Reynolds number.

Estimates of Re_m for the range of operating conditions used in this study show it to be of order one. The characteristic length is the diameter of the thruster, 0.1 m. The characteristic scalar conductivity calculated for an electron temperature of 2 eV is calculated by Spitzer's formula to be 8 $\times 10^3$ $(\Omega m)^{-1}$, which is confirmed by previous measurements in this thruster.[17] Typical values of the flow velocity, inferred from thrust data, are shown in Figure 5-2 and range from about 1 km/s to 20 km/s for the conditions used in this study.[37] These velocities yield values for Re_m of 1 to 20, respectively. Because Re_m is of order one, neither the effects of gradients in the conductivity, nor

Exhaust Velocities Inferred from Thrust Data
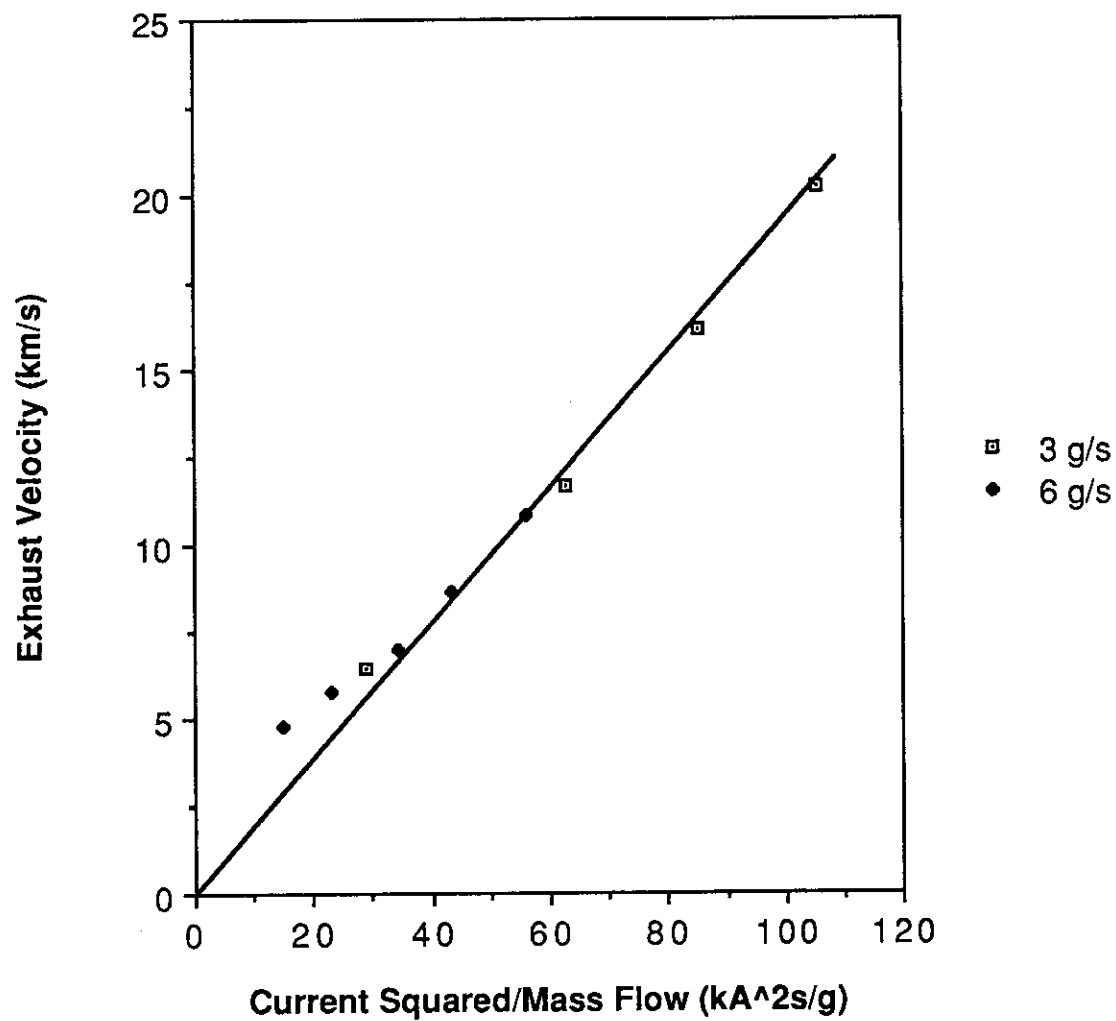
Figure 5-2

the back emf completely dominate the development of the discharge. Initially, when the flow is slow, the thermal instability of the conductivity described in Section 5.1 generates an asymmetric flow. As the flow accelerates to its steady state velocity, the effect of the $\mathbf{u} \times \mathbf{B}$ term becomes more prominent.

For $J^2/\dot{m} = 45$ kA^{2}s/g, which produces an exhaust velocity of about 10 km/s, calculations show that the back emf contribution to the plasma voltage drop is roughly ten times as large as the current density contribution. This means that for a difference of only 10% in back emf from one side of the thruster to the other, the value of the current density component will double. Figure 4-17 indicates that the average asymmetry parameter during the transient for such a value of $J^2/\dot{m}$ is roughly 0.04, which results from an average difference of 8% in the magnetic field from one side of the thruster to the other. When coupled with a difference in flow velocity, it is apparent that the back emf may cause significant adjustments in the conduction pattern during the initial transient.

The back emf mechanism can explain other observations as well. The fact that discharges at low values of $J^2/\dot{m}$ demonstrated more unstable steady state behavior, as seen in Figure 3-9, may be attributed to the fact that the magnetic Reynolds number is of order one for these conditions and the back emf has comparable importance to the conductivity distribution in determining the conduction pattern. If a local increase in conductivity occurs on a time scale short compared with the acceleration of the local flow, non-uniformities in the conduction patterns could exist temporarily before changes in the back emf develop to eliminate them.

The results of the test series in which the mass injection holes were blocked can also be interpreted in terms of the back emf. The observation in section 4.3 that 488 nm ion line intensity was reduced in the region over the plugged holes for a discharge with high $J^2/\dot{m}$ can be explained simply as a reduced ion number density due to the reduced mass flow in the area. However, since conductivity is essentially independent of the charged species number density for these conditions, reduced mass flow cannot directly explain the concurrent decrease in current density. On the other hand, for a given current density and magnetic field, which produces a given body force density, a

104

locally reduced mass flow would result in increased local flow velocity. This increased velocity would create a greater back emf and subsequently reduce the current density, as observed.

The primary appeal of the back emf mechanism is that it accounts for the observed scaling of the asymmetric behavior with $J^2/\dot{m}$. Unfortunately, it is not feasible to determine whether this mechanism can account for the degree of asymmetric behavior or transient times observed. For example, to theoretically predict the time taken to establish symmetry requires knowledge of both the acceleration processes in the discharge as well as the response of various regions to a changing Ohmic power input. The acceleration processes determine how quickly different flow velocities, and therefore different magnitudes of back emf, arise in response to different local values of the Lorentz force. The response of the temperature, and therefore conductivity, to a changing power input determines how quickly redistribution of the conduction pattern occurs. Such an analysis would require knowledge of the three dimensional temperature and flow velocity distributions, which are not available.

With the present analysis tools and knowledge of the propellant state, determination of the relative importance of the two plasma-based mechanisms is not within the scope of this thesis. The principle difference between these two models for the establishment of a symmetric discharge lies in the fact that the diffusion model relies on azimuthal pressure gradients to spread the high conductivity region, whereas the back emf model raises the conductivity surrounding the region of highest current density by Ohmic power deposition. In all likelihood, both mechanisms may work in concert to establish symmetry. Future work suggested at the end of the next chapter may help determine which is more active toward this end.

Chapter 6

SUMMARY AND INTERPRETATION

The azimuthally asymmetric behavior that is observed during operation of a quasi-steady MPD thruster operated at low $J^2/\dot{m}$ was investigated in this study. In addition to high speed photographic sequences, a set of four symmetrically placed magnetic field probes enabled an evaluation of the three dimensional nature of the developing current conduction pattern. A centroid of current parameter was defined to quantify the temporal behavior of the plasma as measured by the four probe rig. Excellent correlation between the luminosity patterns and the centroid of current was demonstrated. In addition, an asymmetry parameter was defined as the instantaneous distance of the current centroid from the center of the thruster. The average of this parameter over the duration of the pulse yields a quantification of the overall degree of asymmetry.

The asymmetric behavior was observed to be a non-recurring transient that is always associated with the initiation of the discharge pulse. The luminous plasma first appears near the base of the cathode in one or more lobes, with lower PFN charging voltages tending to produce a single lobe. As the discharge develops, it coalesces into a single lobe of high luminosity and current density. Throughout the transient, the angular position of this lobe remains the same while the discharge spreads around the thruster equally in both directions until a symmetric pattern is achieved. There is no evidence of a rotating or oscillating spoke. There is also no correlation between the angular position of the lobe and any asymmetry in the anode surface conduction or the mass injection. It is inferred that the angular position of highest current density and luminosity is determined by the local condition of the cathode surface at breakdown.

Because of the electric field induced by the rapidly changing magnetic fields at the beginning of the discharge, current conduction is confined to the rear of the thruster for the duration of the initial current rise, which is 100 μs for this apparatus. A transient peak develops in the overall luminous intensity in conjunction with the current rise and is especially pronounced at low

106

values of $J^2/\dot{m}$. A practical implication of this observation is that time-integrated spectroscopic studies at low values of $J^2/\dot{m}$ are dominated by the luminosity pattern during this bright phase, when the discharge is still very asymmetric. To obtain accurate spectroscopic data for the quasi-steady portion of the pulse, it is necessary to use time-resolved diagnostics.

After a few hundred microseconds, the degree of overall asymmetry, as indicated by the asymmetry parameter, drops to a negligible level, where it remains for the rest of the pulse. However, localized non-uniformities, distinct from the initial transient asymmetry, do persist throughout the pulse. At values of $J^2/\dot{m}$ below about 10 kA^{2}s/g, unsteady spikes and bulges appear for the duration of the discharge. These structures may compromise the validity of using an Abel inversion to generate radial profiles of plasma properties from measurements of intensity along transverse axes. Since the inversion assumes axisymmetry, the radial profiles produced by the inversion become less meaningful as these asymmetries become more pronounced. However, because the asymmetric features are non-steady and tend to average to an axisymmetric distribution, the deleterious effects of these structures could be attenuated by averaging intensity data over several hundred microseconds. Steady azimuthal gradients in the magnetic field are generally small, i.e. less than a 6% difference between the field at opposite sides of the thruster. These steady gradients tend to be worse at lower values of $J^2/\dot{m}$ and in regions of high current density, such as near the anode. For the purposes of probing for magnetic field mapping, the minor effects of temporal variability and azimuthal non-uniformity can be reduced further by averaging over several samples.

The effect of the physical condition of the thruster on overall asymmetric behavior was also investigated. Asymmetric mass injection through the outer holes has no discernible effect on the degree of either transient or steady state asymmetry at low values of $J^2/\dot{m}$. However, at a value of $J^2/\dot{m}$ of 40 kA^{2}s/g, the asymmetric mass injection induces a large, steady decrease in both the luminosity and current density downstream of the plugged holes. Small, but definite changes in asymmetric behavior after exposure of the thruster to air or over the course of several test series

indicate that the surface condition of the electrodes influences asymmetric behavior. The onset of localized changes in the appearance of the anode surface were observed to coincide with steady asymmetric conduction patterns at a wide range of operating conditions and are inferred to correspond to changes in the surface conductivity. Finally, the observation that the establishment of a symmetric discharge is concurrent with the uniform distribution of cathode spots indicates that cathode surface condition may affect the degree of asymmetry. However, an investigation into the effect of operating condition on spot motion shows that the motion of the spots is not the limiting factor in the establishment of symmetry.

Finally, the effect of operating conditions was investigated. The most significant result is that both the duration and severity of the asymmetric behavior were found to decrease strongly with increasing current and less strongly with decreasing mass flow rate. Moreover, the results of the probe studies demonstrate that the severity and duration of asymmetric behavior scales inversely with $J^2/\dot{m}$ for the conditions studied. The fact that it scales with $J^2/\dot{m}$, rather than simply J, has positive implications for the use of MPD thrusters scaled to operate at lower powers. Although the lower powers will entail lower currents, the value of $J^2/\dot{m}$ will have to be kept high to provide high levels of specific impulse. Reconfiguring the PFN to apply twice the charging voltage to the thruster at breakdown for the same steady state current, results in a slight decrease in the asymmetric behavior. This trend has the positive implication that asymmetric behavior can be reduced simply by designing the pulse-forming network to give very high applied voltages at breakdown.

Modeling shows that the initial asymmetric discharge pattern is established when the thermal instability of the conductivity initially causes the current to concentrate in regions of high conductivity. Two mechanisms for the subsequent establishment of a symmetric discharge were discussed. In the first, the high conductivity plasma spreads into regions of low conductivity by diffusion driven by pressure gradients. An estimate of the diffusion velocity shows it to be fast enough to account for the observed transient times. In the second mechanism, the back emf

generated by the interaction between the magnetic field and the moving flow in regions of high conductivity tends to decrease the current flowing there. The redistribution of current flow and the resulting increase in Ohmic power deposition in regions of low conductivity eventually results in an azimuthally symmetric discharge. The mechanism predicts that the severity and duration of the asymmetric behavior should scale with the importance of the back emf term relative to the current conduction term in Ohm's Law. The strength of the back emf term is proportional to the magnetic Reynolds number, $Re_m = \mu_o \sigma_o u_o L_o$, which in turn scales approximately with $J^2/\dot{m}$. Thus, this mechanism is consistent with the observed scaling of the asymmetric behavior.

The most obvious implication for thruster system design is that the thruster should be operated for significantly longer periods than the asymmetric transient times in order to avoid the adverse effects of asymmetric operation. In addition, these results show that it is best to wait for several hundred microseconds before collecting data to ensure axisymmetric operation and that this time will be longer for lower values of $J^2/\dot{m}$. Since the transient times are on the order of a few hundred microseconds, steady state operation would be essentially unaffected by the initial transient phenomenon, although this does not rule out the possibility of other phenomena occurring on time scales much longer than 1 ms. Typical mission requirements will probably demand operation at levels of $J^2/\dot{m}$ over 40 kA^{2}s/g, in order to achieve a specific impulse of more than 1000 s. Under those conditions, the last vestige of asymmetric behavior disappears after 200-300 μs. Therefore, pulsed quasi-steady operation should not be significantly affected if the pulses are on the order of one or two milliseconds long.

If the constraints of the system do not permit operation at conditions that assure a short asymmetric transient, a segmented anode must be employed to ensure axisymmetric operation. By connecting each segment to a separate, but parallel pulse-forming network, equal currents can be made to flow through each segment. For example, the MPD thruster to be used in the upcoming Electric Propulsion Experiment on the Japanese Space Flyer Unit will be operated with 330 μs pulses at a specific impulse of less than 600 s,[15] equivalent to exhaust velocities that resulted in

asymmetric transient times of over 300 μs in the thruster used in this study. As mentioned in Chapter 1, asymmetric behavior is a significant problem in this Japanese thruster. The addition of a segmented anode ensured axisymmetry and increased efficiency as much as 15%. The largest improvement in efficiency occurs at the lowest specific impulse levels,[10] which is consistent with the results of this study that asymmetric behavior is more pronounced at lower values of $J^2/\dot{m}$.

As suggested future work, the effect of breakdown voltage on asymmetric behavior should be investigated over a wider range of voltages by appropriate redesign of the PFN. In addition, more data should be taken with the probe rig at different radii to characterize azimuthal variations in the steady magnetic field. Such data will permit the evaluation of the assumption of azimuthal symmetry in the construction of a magnetic field map. All other future work falls under three categories.

The first entails the direct determination of the effects of the cathode on asymmetric behavior. Most conclusions presented in this regard have been confined to indirect inferences. It should be determined directly whether abrasion or some other form of purposeful mistreatment of part of the cathode surface has an effect on the location of the transient lobe. In addition, application of a material, such as lithium, that changes the work function of the cathode surface or even just handling part of the cathode should be evaluated in a controlled fashion to determine the sensitivity of the asymmetric behavior to non-uniform surface contamination. To further elucidate the role of cathode spots in establishing symmetry, high speed photographic sequences should be taken, focusing on the cathode with an appropriate filter to block plasma line radiation and admit only continuum radiation from the spots. Such sequences would permit a more detailed study of the motion of spot clusters as the discharge develops. Finally, different cathode materials could be used to verify directly that spot motion, which depends strongly on the properties of the cathode material, does not limit the rate at which the asymmetric discharge spreads out.

The second category of future work involves the determination of whether the diffusion of high conductivity plasma is the principle mechanism for establishing a symmetric discharge. A set

of double Langmuir probes should be used to characterize azimuthal gradients in the electron temperature and number density for possible correlation with luminosity patterns. Such information would be useful in estimating the gradients in scalar conductivity. The probes could be configured in the same manner as the magnetic field probes to determine differences in the electron temperature across the thruster, or they could be clustered closer together to determine local gradients. Data on such local gradients would permit a more accurate calculation of expected diffusion velocities. In addition, magnetic field probes oriented to measure the radial component of the magnetic field would permit an estimate of the degree to which this diffusion is slowed by transverse magnetic fields. An added benefit from such extensive Langmuir probe data would be the determination of the variation in steady state temperature over a range of operating conditions.

The final category involves evaluating the influence of the back emf mechanism in establishing a symmetric discharge. First, the relative importance of the back emf term compared to the conduction term in Ohm's Law can be estimated directly from the appropriate probe data, both within the transient region of high luminosity and conductivity and on the opposite side of the thruster. Magnetic field probes have already been used in this thesis to determine the relative magnitudes of the magnetic field. In addition, the axial gradient in magnetic field gives an estimate of the radial current density. Langmuir probe data can be used to estimate the local conductivity, but most importantly Langmuir probes can be used to measure the local flow velocity as well as the difference in flow velocity on opposite sides of the thruster.[38] Second, more extensive studies of the effect of operating conditions could demonstrate whether back emf is a viable mechanism for promoting symmetry. More magnetic field data should be taken at conditions of very low magnetic Reynolds number to determine when and if asymmetric behavior becomes steady. Merely reducing $J^2/\dot{m}$ further in a full scale thruster, such as the one studied for this thesis, is not of primary interest since the lowest $J^2/\dot{m}$ reached yield specific impulse levels below those of practical interest. However, low magnetic Reynolds numbers may be achieved at useful exhaust velocities in a hybrid electrothermal/electromagnetic thruster because the higher chamber pressure can act to reduce the

conductivity. This research is especially pertinent because it is expected that as electrothermal acceleration becomes more prominent, asymmetric behavior may become a problem. In addition, more work should be done to characterize asymmetric behavior with other propellants. Thrust data would provide a measure of the characteristic exhaust velocity. Langmuir probe data would provide an estimate of the characteristic conductivity. Such data could then be used to verify the dependence of asymmetric behavior on magnetic Reynolds number for different propellants.

Appendix A

MASS FLOW RATE CALIBRATION

Mass flow rate calibration was accomplished by measuring the total mass injected and dividing that by the effective length of an injection pulse. The total mass injected was determined by closing the valve to the vacuum pumps, firing a pulse of cold propellant, and measuring the pressure in the vacuum tank. Typical pressures ranged from 50 to 200 μm Hg for one pulse, depending upon the mass flow rate. To account for the pressure increase due to leaks and outgassing, a test was also performed in which the pump valves were closed off and the pressure rise was measured over the time typically taken for the mass injection test. This pressure, which was generally less than 5 μm Hg, was subtracted from injection test measurements. The mass of the injected propellant can be calculated from the ideal gas law. The volume of the tank was calculated to be 1.12 m^3 from detailed measurements of the tank dimensions performed with the help of Alec Gallimore. The temperature of the gas was assumed to be room temperature, which was measured with a thermocouple gauge.

Deriving an effective time for which to calculate to the average mass flow rate is a slightly less straightforward matter. To record the pressure history of the pulse, a piezoelectric pressure transducer was installed between the mass injection valve and the sonic orifices as shown in Figure 2-1. The transducer was connected to a PCB model 482A amplifier, whose output was collected on a digital oscilloscope for later analysis. A typical trace is shown in Figure A-1. The decay in the output over the course of the pulse is primarily due to the drop in plenum pressure as it empties. There is also a slight electronic decay in the signal since the amplifier circuit is designed to measure only AC signals. The magnitude of the electronic decay can be evaluated from the dip below the baseline at the end of the pulse. From the trace in Figure A-1, it is apparent that this electronic decay is negligible, but could be corrected for with digital methods, if necessary.

Since the mass flow through a sonic orifice is proportional to the pressure upstream, the

113
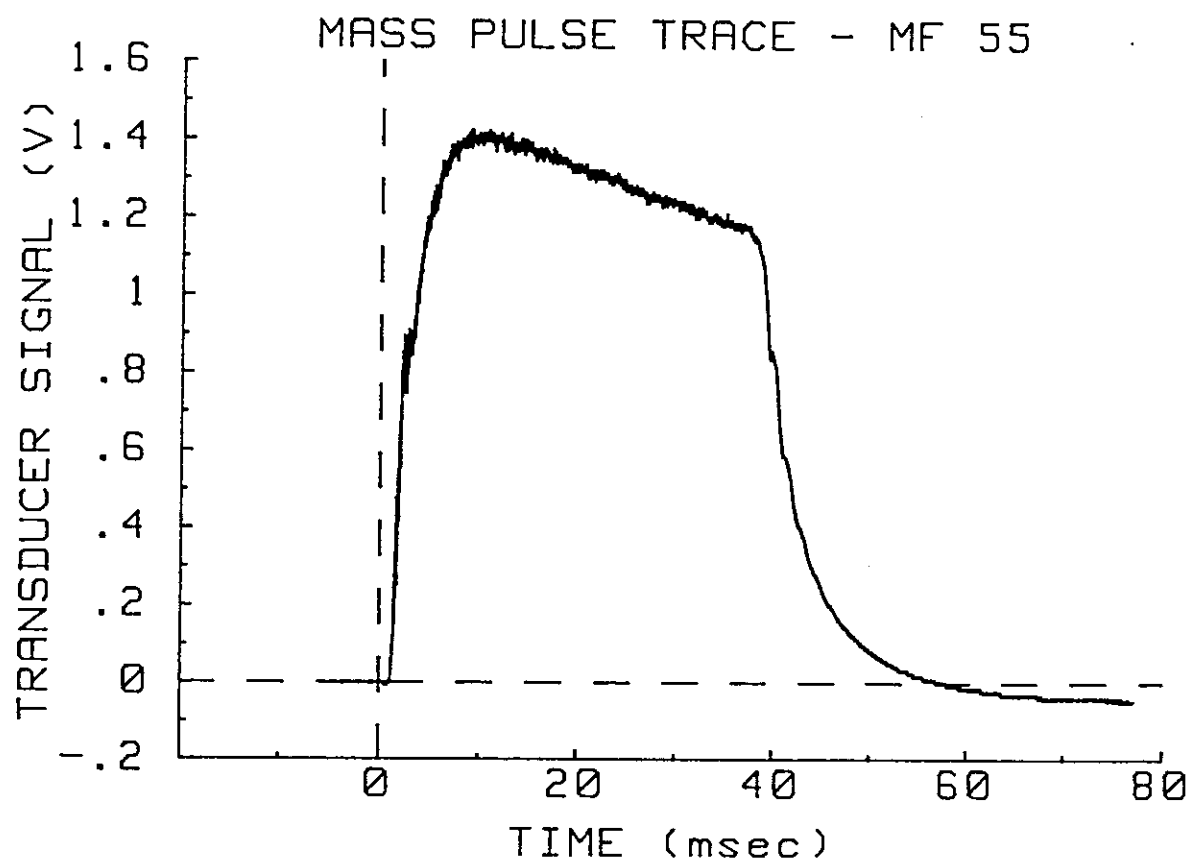
Typical Output from Pressure Transducer

for Mass Flow Rate Calibration

Figure A-1

instantaneous value of the transducer output is proportional to the instantaneous mass flow rate. Therefore, the average of the output for the millisecond during which the current would flow in the thruster is proportional to the average mass flow rate during a discharge. The integral under the transducer trace is proportional to the total mass injected, which is the product of an average mass flow rate and an effective injection pulse length. Thus, the ratio of the integral to the average value of the transducer output during the discharge is the effective injection pulse length. The total mass injected divided by this effective pulse length yields the mass flow rate during a discharge.

Since the pressure at the transducer changes with time, it is necessary to pinpoint the interval on the pulse during which the discharge occurs in order to accurately calculate the mass flow rate during the discharge. The delay between between the signal to the mass injection valve that starts the flow of the propellant and the point when the current starts to flow in the thruster has been calibrated and is shown in Figure A-2. About .5 millisecond should be subtracted from these times to account for the delay between the change in pressure at the transducer and the actual change in mass flow rate downstream in the thruster chamber, assuming such changes propagate at the speed of sound. Since a delay box setting of 6.0 was used throughout this study, the transducer output was averaged over a millisecond starting 20.7 ms after the signal to the injection valve.

The error induced by uncertainty in the delay is estimated to be 1%. The error in the integral under the transducer output is estimated at 2% due to noise and the electronic decay. The error in the temperature is negligible, but the error in the tank volume is estimated at 2%. Finally, the standard deviation in the amount of mass injected from shot to shot was 3%, so the uncertainty in the mass flow rate is estimated to be a total of 8%.

Delay time calibration

$y = 2.1411 + 3.1782x \quad R = 1.00$

□ Delay time 1
◆ Delay time 2

Delay time 1 = time from start of injection solenoid pulse to start of thruster current. Taken 9/18/87

Delay time 2 = time from start of injection solenoid pulse to start of switch solenoid pulse. Taken 10/23/87

Delay time (ms)

Delay Box Dial Setting

Figure A-2
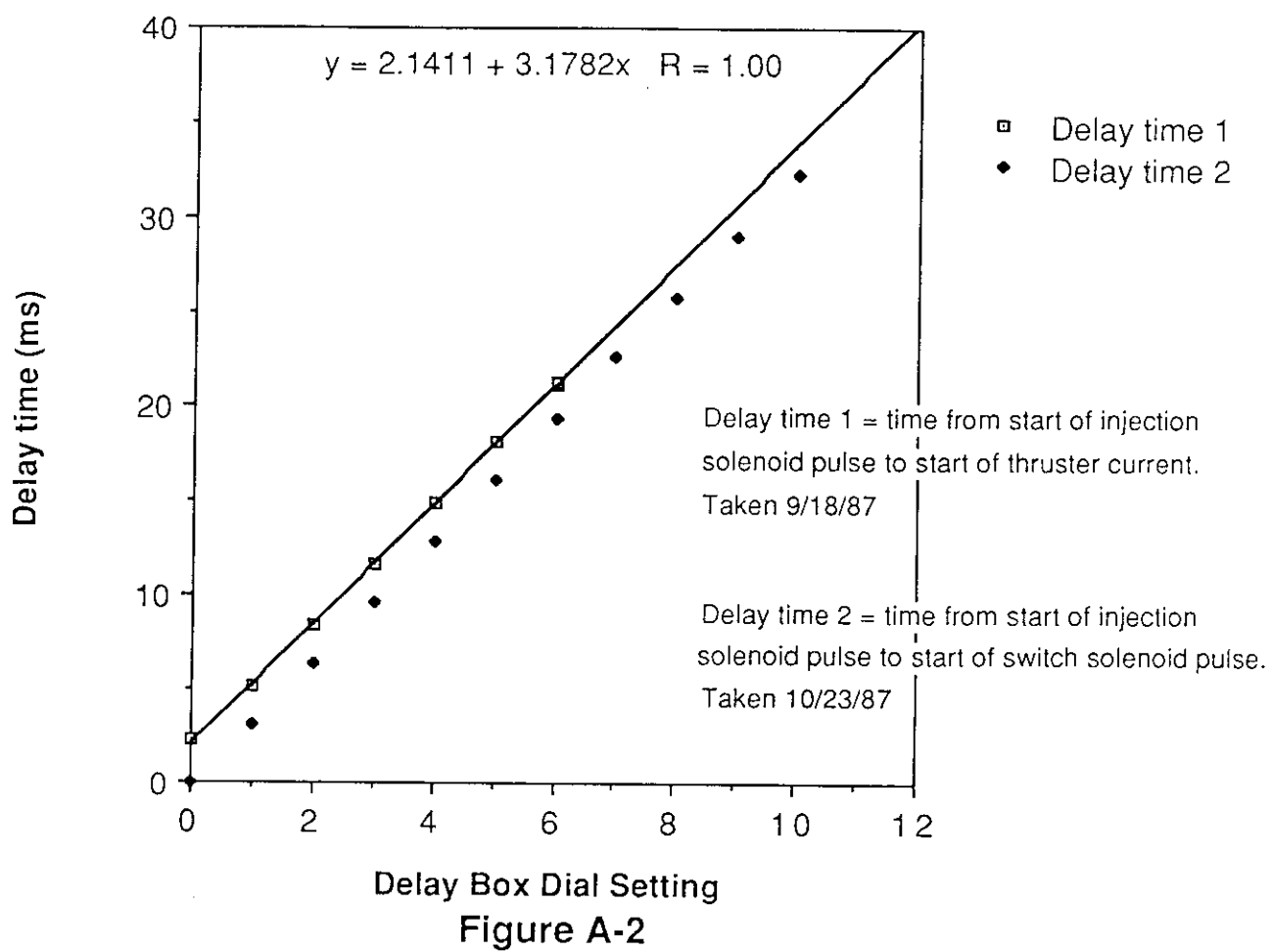
Appendix B

HIGH SPEED MOVIE CAMERA OPERATING PROCEDURES

At the high film speeds required for this study, the camera uses a 100 foot roll of film in roughly one second. For most of that time the camera accelerates the film, and only near the end of the roll does the camera reach top speed. A delay circuit was devised with the aid of George Miller to start the camera and let it run long enough to allow the film to reach a high speed, but not so long that the film runs out before automatically firing the thruster. The schematic diagram for this circuit is shown in Figure B-1. The circuit operates on 12 VDC supplied by a plug-in converter through the red and black banana plug inputs. The trigger input is connected by BNC cable to a signal generator that is set to produce a single, manually triggered, positive-running square wave with no attenuation. The circuit is connected to the remote switch connector on the camera by a long black cable. The delay circuit is connected to the firing circuit by a small gray cable that plugs into a jack on the fire button box.

The procedure for recording a discharge on high speed film is as follows. After the camera has been loaded in the darkened room, the lights are left out. The pulse-forming network is charged to the desired voltage and the power supply is switched off as usual. Instead of triggering the firing sequence directly by pressing the fire button, the signal generator is triggered manually, generating a single square wave that is output to the camera delay circuit. The upstroke of this square wave triggers the relay in the upper left of the diagram, which in turn triggers and latches the large relay in the center of the diagram. Triggering this large relay in turn closes the remote switch to the camera to start the film rolling. In addition, it turns on the "camera" light and turns off the "ready" light that is on when the circuit is in the reset mode. Upon the downstroke of the square wave, the "thruster" light goes on and a relay inside the fire button box initiates the firing sequence of the thruster. The delay, which is equal to the length of the positive square wave pulse output by the signal generator, can be set by adjusting the frequency control on the signal generator. Pressing the reset button on the camera delay box, turns off the "camera" and "thruster" lights and turns on the "ready" light, as

117

well as opening the remote switch to the camera so that the system is ready for the next discharge.

0 to +5V DC
Input from
Function Generator

Power Supply Input

+12V

GND

NC

12V 4PDT
Radio Shack
275-214

NC

NC

To Camera

Red "CAMERA" Light

NC

NC
Reset Button

Green "READY" Light

NC

Original Fire Switch

Blue "THRUSTER" Light

NC

X

NC

To Fire Control Circuit

Fire Button Box
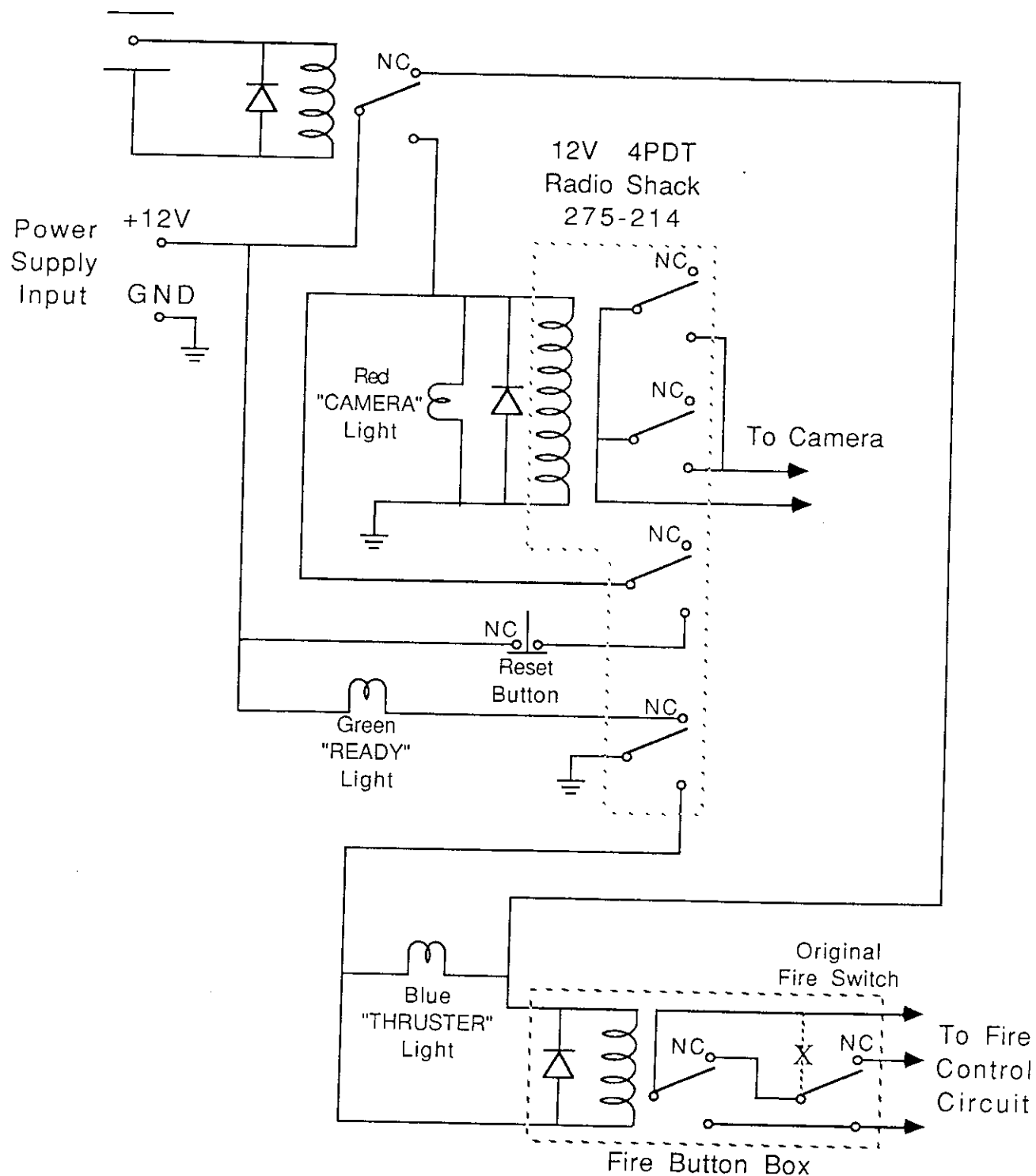
Camera Delay Circuit Diagram

Figure B-1

Appendix C

MAGNETIC FIELD PROBE CHARACTERISTICS AND CALIBRATION

Much work was done to develop probes and integrators for these experiments. The following represents a compendium of what was learned in the process.

The four parallel magnetic field probes used for this thesis were each encased in quartz and connected by a tri-axial cable to an active electronic integrator. The probe itself is a small coil of #44 formvar wire wrapped around a thin Lucite rod. The two leads of the coil are tightly twisted together and shielded by a stainless steel tube to avoid spurious electromagnetic pick-up. The coil leads are connected to the center conductor and inner shield of the tri-axial cable, with the outer shield being used to connect the stainless tube to the grounded instrument cage. Thus, the shielding acts as an extension of the instrument cage. The coil itself is not shielded from capacitive coupling with the plasma because the capacitance between the plasma and the coil through the .5 mm quartz walls is very small, and such shielding tends to attenuate the desired magnetic signal. The input impedance to the integrator is matched to the tri-axial cable impedance to avoid reflections and distortions of the probe signal due to the long cable. Finally, the output of the integrator is connected to a digital oscilloscope by a short coaxial cable with its own matched terminating resistor.

C.1 The Effect of the Probes on the Plasma

Since the probes physically perturb the plasma, it is important to determine that they do not significantly affect the magnetic field measurements by their presence. One effect of the probes is to alter the conduction pattern in the plasma by introducing regions of reduced conductivity. Not only do the probes themselves represent a volume of negligible conductivity, but they can cool the nearby plasma, thereby reducing its conductivity. Since ions and electrons that strike the relatively cool surface of the probe recombine and are re-emitted as cold neutral atoms, the probes act as heat

120

sinks.

However, since the thermal conductivity of the plasma has a dependence on temperature to the 5/2 power, cooling of the nearby plasma results in a strong "self-insulating" effect that tends to limit the extent of the temperature perturbation. It has been shown that for a spherical probe, significant reduction in temperature does not exist outside two probe radii even in the steady state.[39] Although it is not feasible to calculate the extent of the cool region around long, thin cylindrical probes, empirical evidence suggests that the perturbation in temperature is not extensive. For example, there is no extensive nearby reduction in argon ion radiation, which is extremely temperature sensitive. In addition, no change in the terminal voltage and current characteristics were noted with the insertion of probes, which might be expected if the probes caused widespread cooling of the plasma. In any case, both the size of the conductivity perturbation and the amount of heat absorbed by the probe scale with the radius of the probe, so every effort was made to keep the probes small.

Sealed quartz tubes were used as the outer sheath for the probes, both to withstand shattering and to avoid introducing impurities or significant additional mass flow in the form of evaporated probe material. Glass tubes were found to be prone to shattering in the discharge. Insulating the tip of the probe with epoxy, as has been done in the past instead of sealing the quartz tube, results in ablation of the epoxy. Although even quartz will boil if the discharge pulse is long enough, it can be shown that in the worst case the time until this happens is longer than the discharge used in this study. By employing the analysis used by Lovberg[39] in which the thermal diffusion equation is solved for a plane probe surface, the time until the surface of the probe boils is given by:

$$t_b = Q/q_o^2.$$

Q is a constant for the probe material, depending on the boiling temperature, thermal conductivity, density and specific heat, and is approximately 10^{13} W^2/cm^4s for quartz.

The heat flux incident upon the surface of the probe, q_o, can be calculated assuming that the ions and electrons incident upon the probe give up their thermal and ionization energy, recombine,

121

and leave the probes as cold, neutral atoms. Due to the higher mobility of the electrons, the probe surface will charge negatively and develop an electron-repelling sheath large enough to make the electron and ion fluxes equal at the probe surface. Since only the highest energy electrons can reach the probe surface, the average energy of the electrons reaching the probe is higher than the average thermal energy by a factor involving the sheath voltage. The total heat flux at the probe surface becomes:

$$q_o = (n_i v_i/4)[(eV_s + 2kT_e) + 2kT_i + \varphi_i].$$

where n_i is the ion number density and v_i, the mean ion thermal velocity, equals $\sqrt{8kT_i/\pi m_i}$. From the constraint of equal electron and ion fluxes, the sheath voltage, V_s, is given by:

$$V_s = (kT/2e) \ln(m_i/m_e).$$

φ_i is the ionization energy, which is 16 eV for argon. The electron and ion temperatures are both assumed to be about 2 eV. In the worst case, assuming that the mass flow is evenly distributed across the thruster chamber and fully ionized, n_i would be $8 \times 10^{21}/m^3$. Under these conditions, t_b would be 9 ms, which is several times the discharge pulse length. In actuality, t_b is likely to be longer since not all charged particles will be absorbed. Also, the magnetic fields will partially shield the probes by limiting diffusion across field lines. Moreover, because of the pumping force, n_i will be considerably lower than average near the anode where the probes were placed.

A final consideration of the effect of the probes involves the ability of the magnetic field to diffuse to the probe coil. The presence of a stationary probe in the moving plasma will stagnate the flow in front of the probe tip. If the conductivity in the plasma were infinite, the magnetic field would be frozen into the stagnated plasma, and the probe would not measure the magnetic field present in the unperturbed flow. The degree of freezing scales with the magnetic Reynolds number:

$$Re_m = \mu_o \sigma u L.$$

For very large Re_m, the field is frozen. For $Re_m < 1$, this effect is negligible and the probe essentially measures the unperturbed field. Since L, the length scale of interest, is the probe diameter, it is again advantageous to use as small a probe diameter as possible. For a conductivity,

σ, of 8×10^3 $\Omega^{-1}m^{-1}$, a probe diameter of .004 m, and a flow velocity, u, of 10^4 m/s, the magnetic Reynolds number is .4, which means that the field is not frozen. The placement of the probes 2 cm from the backplate and 4.5 cm from the thruster centerline has the advantage of putting them in a region of even lower magnetic Reynolds number. Since this is an unaccelerated region of the flow, the flow velocity is closer to the sonic speed, which is on the order of 10^3 m/s. In addition, the conductivity of that region is likely to be lower than near the electrodes where the conductivity was measured. In conclusion, the delay due to diffusion of flux to the probes has a negligible effect on the field measurements in this situation.

C.2 Probe Characteristics

At the heart of an induction probe such as the ones used in this study, lies a small coil of wire, across which changes in the component of the magnetic field parallel to the coil axis induce a voltage. The two chief parameters in the design of the probe coil are r_c, its radius, and N, the number of turns. To limit the perturbation of the plasma by the probe, it is desirable to make the external probe radius, and therefore the coil radius as small as possible. In addition, a small coil radius yields better spatial resolution. For a variety of reasons, the smallest feasible dimensions were found to be .75 mm for the coil radius and 4 mm for the outer probe diameter.

The number of turns in the coil was limited to 30, mainly because this was the most that would fit in a single layer that was short enough to fit inside the quartz sheath. Since the coil axis must be perpendicular to the sheath axis, the coil length is constrained to be roughly equal to the coil diameter. Only a single layer of turns was used because the turns in the subsequent layers tended to be irregular and irreproducible, making it difficult to produce four similar probes.

An added advantage to a small coil with few turns is a high frequency response due to the small coil inductance. To see the effect of the coil inductance on the frequency response, it is useful to analyze the probe circuit as a single current loop. A voltage, V_i, is induced across the probe coil, which has an associated resistance, R_p, and inductance, L_p. Since the integrator input impedance,

Z, is matched to the cable impedance, the loop can be considered to be completed by a simple resistance equal to Z, which is 75 Ω for these probes. Technically, the integrator does not measure V_i directly. Instead, it measures the voltage drop, V_Z, across the input impedance. By summing the voltages around the current loop according to Kirchoff's Law, it is possible to solve for V_Z:

$$V_Z = V_i [Z / (Z+R)] \{1 - (L_p/ZV_i) dV_Z/dt\}.$$

It can be shown that V_Z is proportional to V_i only if:

$$| (L_p/(Z+R_p)) dV_Z/dt | << V_Z.[40]$$

Thus, it is desirable to limit the coil inductance. The inductance of a coil of wire of a given length to radius ratio is proportional to $r_c N^2$, so reducing the coil size and number of turns makes this inequality easier to satisfy. For coils with a .75 mm radius, 1.5 mm length, and 30 turns, the inductance is approximately 10^{-6} H. Their resistance, R_p, was measured to be about 3 Ω, so $L_p/(Z+R_p) \approx 10^{-8}$ s. Therefore, the frequency response of the probes is 100 MHz, which is quite adequate since it is two orders of magnitude higher than the sampling rates used in this study.

The main disadvantage to using small coils with few turns lies in a reduced sensitivity. The voltage induced on a coil by the changing magnetic flux through it is given by:

$$V_i = - (N\pi r_c^2) \partial B/\partial t.$$

Assuming the effect of the coil inductance to be negligible, the voltage across the input impedance, V_Z, is simply $(Z / (Z+R_p))V_i$. However, since R_p is negligible compared to Z for these coils, V_Z is essentially equal to the induced voltage. The output of the integrators, which is the voltage actually recorded, is the integral of V_Z times a gain factor G:

$$V_o = \int GV_Z(t) \, dt = G\int (-N\pi r_c^2 \partial B/\partial t) \, dt = - GN\pi r_c^2 B.$$

From this relation it is obvious that the reduced sensitivity of a small probe can be offset somewhat by designing the integrators with a larger gain.

C.3 Integrator Characteristics

A complete schematic drawing of the integrators designed for this study is shown in Figure
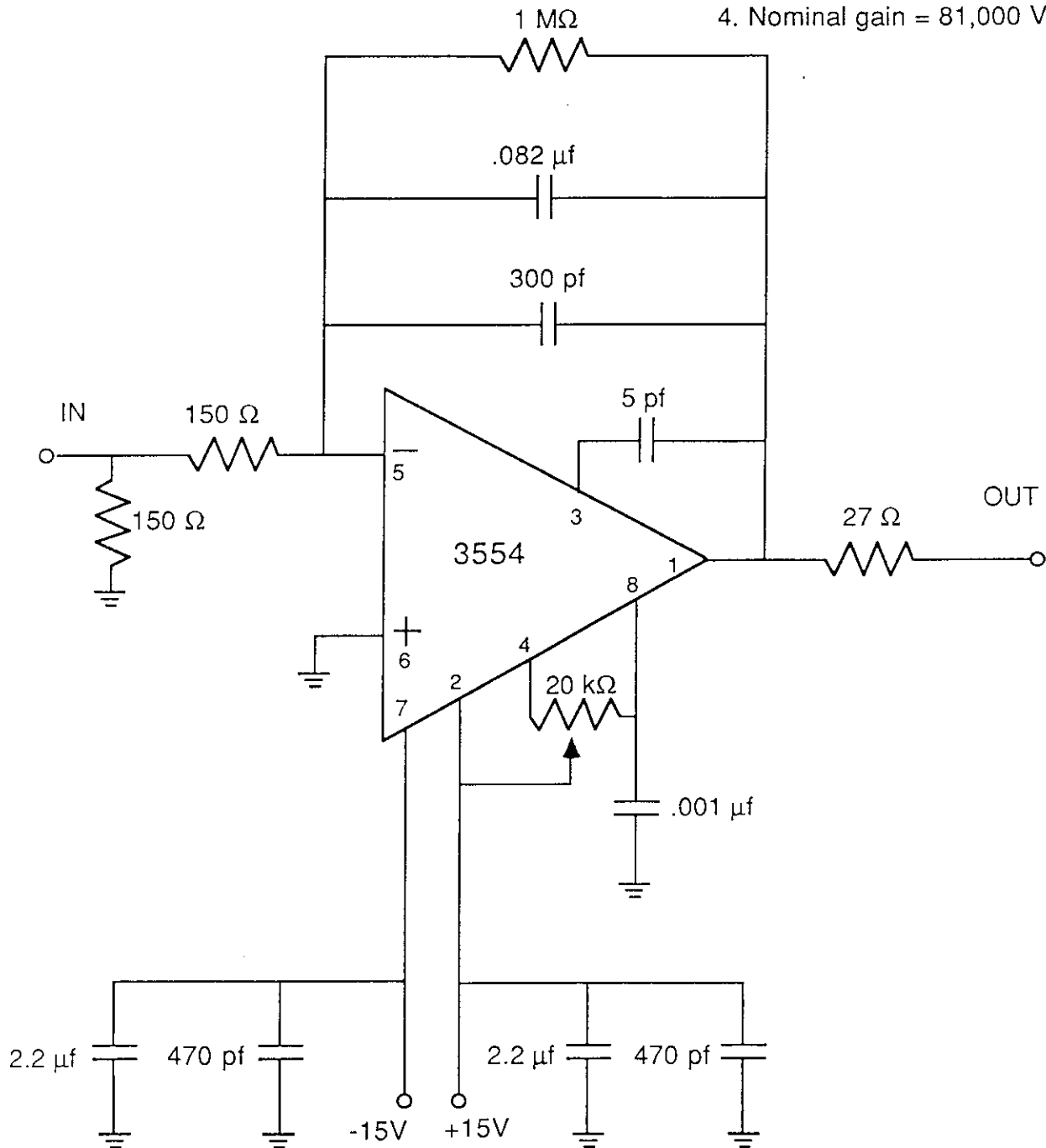
124

C-1. These integrators were designed to balance the competing requirements for high gain and high frequency response with little noise and baseline drift. The input and output leads not shown are commonly grounded. The central component of the integrator is the 3554 operational amplifier with its positive input connected to the grounded lead from the probe. The 150 Ω resistor in series between the other probe lead and the negative amplifier input, in conjunction with the feedback capacitance between the output and negative input of the amplifier, provides the integration capability. Because the negative input to the amplifier is effectively always at ground potential, the combination of the two 150 Ω resistors yields an effective input impedance of 75 Ω that matches the probe cable impedance. The 1 MΩ feedback resistor filters out very low frequency components of the input that can cause the baseline to drift off the oscilloscope screen between discharges. Other components depicted act to reduce noise and stabilize the output.

The 3554 operational amplifier was chosen for its very high frequency response of 1 GHz. Previous integrators using amplifiers with a more modest frequency response were often too slow to follow the rapidly varying signal at the beginning of the pulse. When the amplifier is too slow to follow a rapidly varying input, the resulting output does not return to the same base line after the pulse as existed before it. Often, this spurious shift in the output was over 50% of the true maximum output, leading to much difficulty in evaluating the data. The use of the faster amplifier eliminated this problem.

The integrator gain factor, G, is equal to 1/RC, where R is the resistance in series between the probe and the negative input to the amplifier, and C is the feedback capacitance. The gain can be made as large as necessary by using a small enough resistance and capacitance. However, because the negative amplifier input is effectively ground, using a resistance smaller than the terminating resistance on the input cable lowers the input impedance below that of the probe cable. The resulting impedance mismatch will cause reflections and the low impedance will lower the frequency response of the probe. In these integrators the 150 Ω integrating resistor allows a high gain, while still providing a matched input impedance of 75Ω in conjunction with the 150 Ω

Integrator Circuit

Figure C-1

NOTES:
1. Input impedance = 75Ω.
2. Use short RG 58 (50 Ω) output cable.
3. 82 ms nominal washout. (~70ms actual decay time constant)
4. Nominal gain = 81,000 V/V/s.

resistance between the probe leads. The use of .0823 µf in feedback capacitance yields a nominal gain of 8.1×10^4 V/V/s.

Although a high gain can compensate for the weak probe output, it does not, of course, improve the signal to noise ratio. A major problem with integrators of this type is the tendency of their output to drift out of the range of the oscilloscope as spurious input biases are integrated between discharges. Disconnecting the probe from the integrator and connecting the integrator inputs together has no effect on the output drift, demonstrating that the input biases are generated within the amplifier itself. A higher gain amplifies the effect these biases have on the output, making the output drift farther and more rapidly. The problem is compounded by the fact that the bias across the inputs of the 3554 amplifier is particularly sensitive to changes in temperature. Therefore, it is very important to assure as constant an amplifier temperature as possible, by isolating it from air currents and allowing it to achieve a steady operating temperature for at least an hour before taking data.

To prevent steady or very low frequency biases across the amplifier inputs from being integrated until the output is out of range, a large feedback resistance is mounted in parallel with the capacitor. The feedback resistance has the effect of bleeding off some of the charge on the capacitor, essentially acting as a low frequency filter. To combat the increased output drift due to a high gain and sensitive amplifier, a smaller feedback resistance can be used. However, too small a resistance will decrease the characteristic decay time of the output to such an extent that it impinges upon the desired measurement during a discharge pulse. The 1 MΩ resistance used in these integrators was just low enough to provide adequate baseline output stability, while yielding a 70 ms decay time. This decay is acceptable because it results in only a 1% drop in output over a 1 ms discharge, which is small compared with uncertainties in the probe position and calibration. In addition, in this study accurate absolute measurements of the magnetic field were not as important as relative ones, which are affected only by differences in the feedback resistors in different integrators.

127

C.4 Calibration Procedures

Each probe and integrator pair was integrated as a set in a calibration stand constructed for the purpose. The stand allows precise positioning of the probe coil in the center of a Helmholtz coil that is driven by a small bank of capacitors. A manually triggered square wave of an appropriate length, such as 40 ms, from a function generator controls a transistor that allows current to flow in the Helmholtz coil. The magnetic field produced by the Helmholtz coil is proportional to the voltage to which the capacitor bank is charged. The proportionality constant between the field and the voltage was calibrated with a Hall effect probe and Gaussmeter that measures the absolute magnetic field without integration.

Typical output from the Gaussmeter during a calibration pulse is shown in Figure C-2. The relatively long rise time is due to the impedance of the Helmholtz coil. After peaking, the magnetic field decays slowly with a characteristic time of 2.15 s as the driving capacitance discharge. Since the field plateaus between 30 and 35 ms after the start of the discharge, the calibration was determined from the average output between those times to be 6.838 T/V.

Because 30 ms are required to allow the calibration field to achieve its calibrated value, the probe calibrations must use pulses at least this long. For this pulse length, the decay in the integrator output due to the feedback resistance significantly affects the probe calibration (Figure C-3, top). Thus, an algorithm was developed to numerically correct the digitized traces. Since the time between data points is much less than the characteristic decay time, the undecayed data points can be approximated very accurately as:

$$V(p)_{corrected} = V(p-1)_{corrected} + V(p)_{raw} - V(p-1)_{raw} \, e^{-t/\tau}.$$

$V(p)_{corrected}$ is the pth data point corrected to its undecayed value, and p is 2, 3, 4, ...N, the number of data points. The first data point is assumed to be zero. t is the time between data points, and τ is the decay time constant. Raw and corrected calibration traces are shown in Figure C-3.

The decay time constant for each integrator were determined by trial and error as the number

128
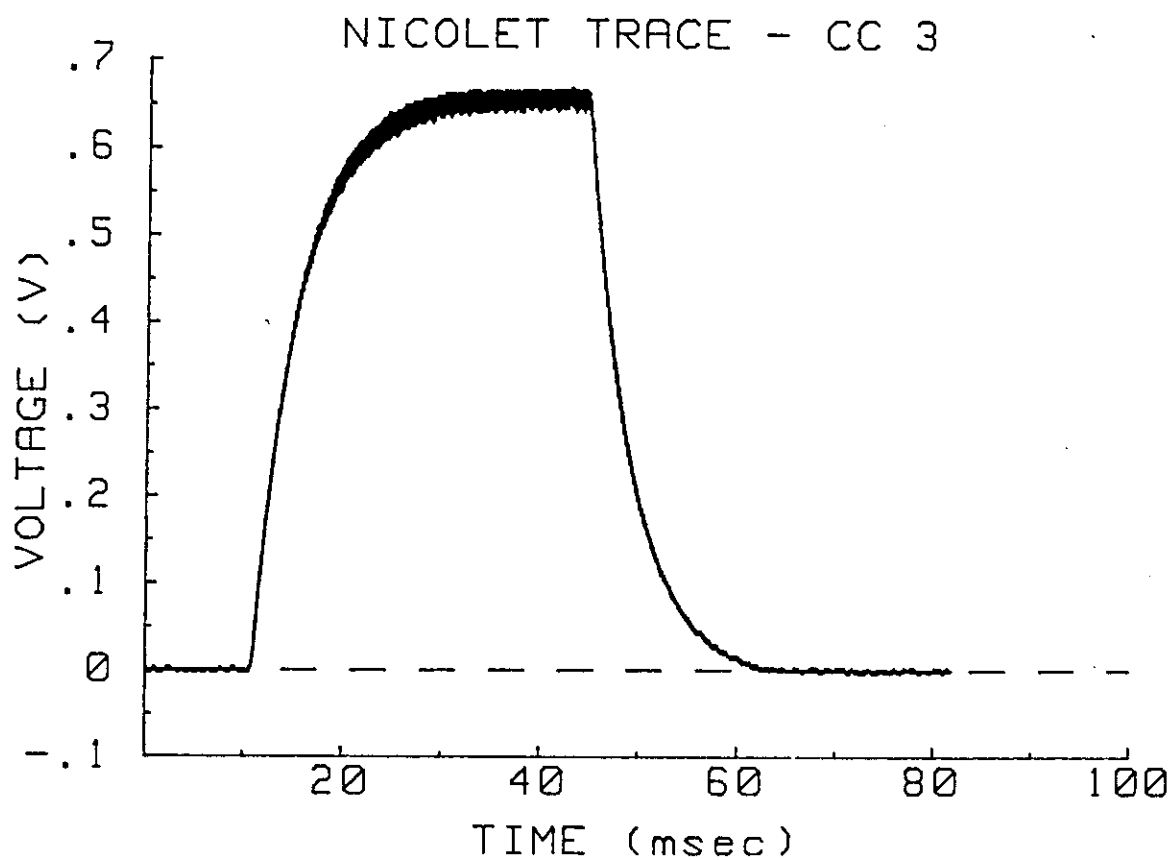
Typical Output from Gaussmeter
for Helmholtz Coil Calibration

Figure C-2
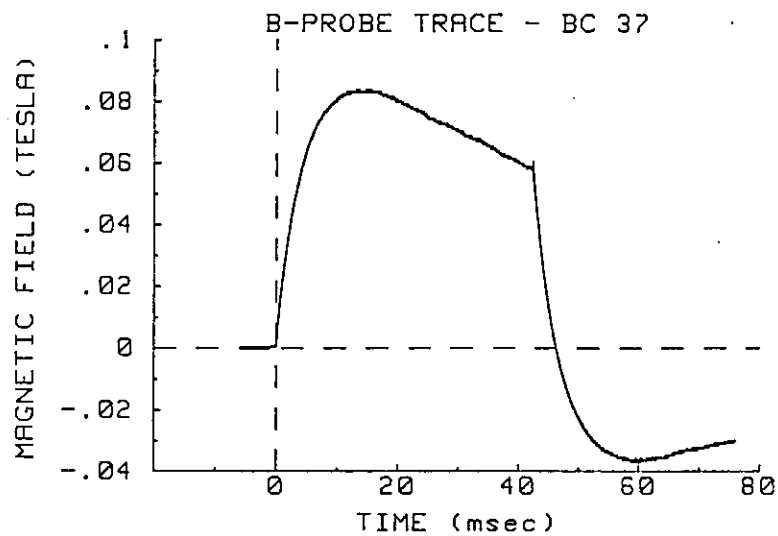
Raw Magnetic Field Probe Calibration Trace
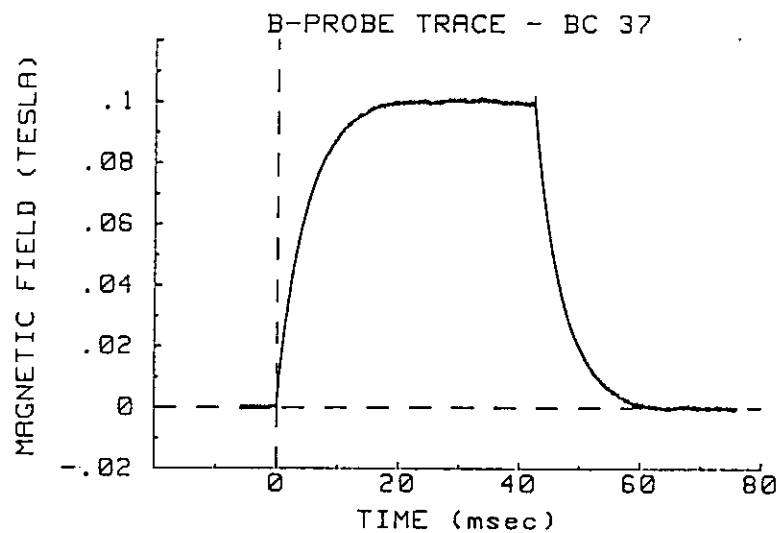
Corrected Magnetic Field Probe Calibration Trace

Figure C-3

that resulted in the same baseline before and after the pulse. Attempts to calculate the time constant from the nominal electronic component values or to measure it directly yielded unsatisfactory corrections. The estimated uncertainty in the decay constant contributes only 1 % to the 2 % uncertainty in the probe calibration. The other 1 % uncertainty results from the standard deviation of the calibration data.

REFERENCES

1 Jahn, Robert G. <u>Physics of Electric Propulsion</u>. New York: McGraw-Hill Book Company, 1986.

2 Berry, W., Bartoli, C. and Trippi, A. "The ESA Policy and Programme for the Development of Electric Propulsion." AIAA paper 88-001, 20th IEPC, Garmisch-Partenkirchen, W. Germany, 1988.

3 Jahn, Robert G. and Kelly, Arnold J. "Megawatt Level Electric Propulsion Perspectives." in <u>Space Nuclear Power Systems</u>. ed. M. S. El-Genk and M. D. Hoover. Malabar, FL: Orbit Book Co., 1988, pp. 499-505.

4 Clarke, Kenn E. "Quasi-Steady Plasma Acceleration." Diss. Princeton University, 1969.

5 Gilland, Jim. "MPD Large Plexiglas Tank Laboratory Notebook." Electric Propulsion Laboratory, Princeton University, 9/5/84-9/6/84, pp. 64-65.

6 Polk, Jay. "MPD Thruster Erosion." in "Electric Propulsion Laboratory Progress Report 1776.14." Princeton University, July/Aug., 1988, pp. 11-15.

7 Polk, Jay. "Fiberglass Tank Laboratory Notebook #11." Electric Propulsion Laboratory, Princeton University, 7/10/88 - 7/23/88, pp. 46-73.

8 Simpson, T.B. "Experimental Study of the Helium MPD Discharge." in "Pulsed Electromagnetic Gas Acceleration Report 634ac." Princeton University, 1978, pp. 70-78.

9 Heimerdinger, Daniel J. "Fluid Mechanics in a Magnetoplasmadynamic Thruster." Diss. M.I.T., 1988.

10 Nishida, E., Shimuzu, Y. and Kuriki, K. "Improved Thrust Generation Mechanism for Electrothermal/Electromagnetic Arcjet." AIAA paper 88-026, 20th IEPC, Garmisch-Partenkirchen, W. Germany, 1988.

11 Choueiri, Edgar Y. "Plasma Thruster Modeling" in "Electric Propulsion Laboratory Progress Report 1776.05." Princeton University, May, 1987, pp. 4-14.

12 Kaplan, David I. "Performance Characteristics of Geometrically-Scaled MPD Thrusters." Diss. Princeton University, 1982.

13 Polk, Jay. Personal communication.

14 Kurtz, H.L. et al. "Cylindrical Steady-State MPD Thruster." AIAA paper 88-025, 20th IEPC, Garmisch-Partenkirchen, W. Germany, 1988.

15 Shimuzu, Y., Toki, K., and Kuriki, K. "Development of an MPD Propulsion System." AIAA paper 88-015, 20th IEPC Garmisch-Partenkirchen, W. Germany, 1988.

16 Barnett, John W. "Operation of the MPD Thruster with Stepped Current Input." Diss. Princeton University, 1985.

17 Turchi, Peter John. "The Cathode Region of a Quasi-Steady Magnetoplasmadynamic Arcjet." Diss. Princeton University, 1970.

18 Polk, Jay. "Electric Propulsion Laboratory Progress Report." 1986.

19 Greim, H. P. Plasma Spectroscopy. New York: McGraw-Hill Book Co., 1964.

20 Campbell, Edward M. "The MPD Accelerator as a Plasmadynamic Laser Source." in "Pulsed Electromagnetic Gas Acceleration Report 634aa." Princeton University, 1976.

21 Rudolph, L.K. "The MPD Thruster Onset Current Performance Limitation." Diss. Princeton University, 1980.

22 Choueiri, E.Y., Kelly, A.J. and Jahn, R.G. "The Manifestation of Alvén's Hypothesis of Critical Ionization Velocity in the Performance of MPD Thrusters." AIAA paper 85-2037, 18th IEPC, Alexandria, VA, 1985.

23 Simpson, T.B. "Plasma Ionization State and Composition in the MPD Accelerator" in "Pulsed Electromagnetic Gas Acceleration Report 1467." Princeton University, 1979, pp. 50-61.

24 Mitchner, M. and Kruger, C. H. Partially Ionized Gases. New York: John Wiley & Sons, 1973.

25 Wiese, W. L., Smith, M. W. and Miles, B. M. Atomic Transition Probabilities: Sodium through Calcium, Volume II. Washington: National Bureau of Standards, 1969.

26 Schrade, H.O. "Arc Cathode Spots, Their Mechanism and Motion." XIII International Symposium on Discharges and Electrical Insulation in Vacuum, Paris, 1988, pp. 172-4.

27 Harris, L.P. "Arc Cathode Phenomena" in Vacuum Arcs: Theory and Application. ed. by J. M. Lafferty. New York: John Wiley & Sons, 1980.

28 Murphree, D. L. and Carter, R. P. "Visual Observations on the High Current Transition from the Constricted to the Diffuse MPD Arc Mode." 14th Symposium on Engineering Aspects of MHD, Vol. VIII, 1974, p. 41.

29 Merke, W. D. et al. "Nozzle Type MPD Thruster Experimental Investigations." AIAA paper 88-028, 20th IEPC, Garmisch-Partenkirchen, W. Germany, 1988.

30 Berisch, R. "Surface Erosion by Electrical Arcs." pp. 495-513.

31 Bond, C. E. "Slanting of Magnetically Stabilized Electric Arc in a Transverse Supersonic Flow." Physics of Fluids, Vol. 9 April, 1966. pp. 705-710.

32 Murphree, D.L. and Carter, R.P. "Low-pressure Arc Discharge Motion Between Concentric Cylindrical Electrodes in a Transverse Magnetic Field." AIAA Journal, Vol. 7, No. 8, 1969, pp. 1430-1437.

33 Gallagher, C.J. "The Retrograde Motion of the Arc Cathode Spot." J. Appl. Phys., Vol. 21, 1950, pp. 768-771.

34 Cory, John Slane. "Mass, Momentum and Energy Flow from an MPD Accelerator." Diss. Princeton University, 1971.

35 Cramer, W. H. J. Chem. Phys., Vol. 30, 1959, p. 641.

36 Choueiri, E. Y., Kelly, A. J. and Jahn, R. G. "Current Driven Instabilities of an Electromagnetically Accelerated Plasma." AIAA paper 88-042, 20th IEPC, Garmisch-Partenkirchen, W. Germany, 1988.

37 Gilland, J. "The Effect of Geometrical Scaling on MPD Thruster Behavior." Diss. Princeton University, 1988.

38 Choueiri, Edgar Y. "Plasma Thruster Modeling" in "Electric Propulsion Laboratory Progress

Report 1776.11." Section V, Princeton University, January/February, 1988, pp. 7-11.

39 Lovberg, R. H. "Magnetic Probes" in <u>Plasma Diagnostic Techniques.</u> ed. by Richard H. Huddlestone and Stanley L. Leonard. New York: Academic Press, 1965.

40 Bötticher, W. "Measurement of Magnetic Fields in Plasmas" in <u>Plasma Diagnostics.</u> ed. by W. Lochte-Holtgreven. Amsterdam: North-Holland Publishing Company, 1968.